Tampere University

UMAIR AHMED

Energy-Based Constitutive Modeling and Finite Element Analysis of Magnetostrictive Energy Harvesters

Tampere University Dissertations 979

Tampere University Dissertations 979

UMAIR AHMED

Energy-Based Constitutive Modeling and Finite Element Analysis of Magnetostrictive Energy Harvesters

ACADEMIC DISSERTATION
To be presented, with the permission of
the Faculty of Information Technology and Communication Sciences
of Tampere University,
for public discussion in the auditorium S2 (SA203),
of the Sähkötalo, Korkeakoulunkatu 3, Tampere,
on 22 March 2024, at 12 o'clock.

ACADEMIC DISSERTATION
Tampere University, Faculty of Information Technology and Communication Sciences
Finland

Responsible supervisor and Custos
Associate Professor
Paavo Rasilo
Tampere University
Finland

Pre-examiners
Professor
Daniele Davino
University of Sannio
Italy

Professor
Xavier Mininger
University of Paris-Saclay
France

Opponent
Professor
Saša Zelenika
University of Rijeka
Croatia

Cover design: Roihu Inc.

ISBN 978-952-03-3344-7 (print)
ISBN 978-952-03-3345-4 (pdf)
ISSN 2489-9860 (print)
ISSN 2490-0028 (pdf)
http://urn.fi/URN:ISBN:978-952-03-3345-4

Carbon dioxide emissions from printing Tampere University dissertations have been compensated.

PunaMusta Oy – Yliopistopaino
Joensuu 2024

ABSTRACT

This thesis validates the suitability of a thermodynamic magneto-mechanical constitutive model based on Helmholtz free energy density and an equivalent stress model to analyze galfenol-based magnetostrictive energy harvesters. The models are validated against measurement results obtained from prototype harvester devices. The choice of using galfenol as an active material was made after comparing the magnetic and mechanical properties of giant magnetostrictive materials. Rod-type and cantilever-beam-type energy harvester geometries have been utilized for the development of prototype energy harvesters. The choice of such geometries was based on a survey of state-of-the-art energy harvesters.

The aim of the thesis is to present a modeling approach that can be utilized to analyze different geometric configurations of the magnetostrictive energy harvesters. The magneto-mechanical constitutive models are implemented in 2D axisymmetric and 3D finite element (FE) models to investigate the coupled magneto-mechanical behavior of the galfenol material. The 2D axisymmetric model is implemented in MATLAB using in-house coding, whereas COMSOL Multiphysics is utilized for 3D finite element simulations. The measured and simulated results were compared, keeping in mind the sensitivity and repeatability of the measurements and limitations of the models. The leading principle of this thesis is the validation of the proposed modeling approaches to analyze both rod-type and cantilever-beam-type energy harvesters.

The research involved studying the influence of change in the operating conditions and the design parameters on the performance of magnetostrictive energy harvesters. The thermodynamic magneto-mechanical model is able to successfully predict the magneto-mechanical behavior of a rod-type energy harvester under different mechanical loadings and magnetic bias conditions. The model is also able to determine the influence of the mechanical preload, dynamic load, magnetic bias, and load resistance on the output power under forced dynamic mechanical excitations. The model also confirms that the optimal preload value changes as a function of the magnetic bias. For a cantilever beam-type energy harvester, the model is able to accurately predict the influence of

magnetostriction upon resonant frequency. In addition, the model can also successfully determine the resonant frequency and open circuit voltage under different amplitudes of mechanical vibrations.

The equivalent stress model can transform any arbitrary stress tensor into a uniaxial stress. The model is able to determine the correct permeability of the material for a combination of flux density vector and stress tensor. It allows a simplified approach to predict the permeability change from measurements to analyze the magnetostrictive energy harvesters and to determine the influence of mechanical loading over magnetic bias. The results validate that both models are able to reproduce the measurement results with reasonable accuracy and are therefore suitable to be utilized as a tool to analyze magnetostrictive energy harvesters.

PREFACE

The research work related to this thesis was primarily carried out at the research group of Electromechanics at Tampere University. Part of the research work was done during a research exchange period as an international collaboration with Istituto Nazionale di Ricerca Metrologica (INRiM), Italy. I would like to thank my supervisor Associate Prof. Paavo Rasilo for providing me the opportunity to work on this interesting topic of modeling and finite element analysis of magnetostrictive energy harvesters. I am grateful for his guidance, support, and supervision during my research career. I would also like to thank my colleagues from Italy, Dr. Mauro Zucca and Dr. Stefano Palumbo, for their help and support in the experimental setup at their laboratory. Also, I am thankful to my colleague from Aalto University Dr. Ugur Aydin for providing guidance with COMSOL Multiphysics software. I am thankful to Dr. Juha Jeronen for his help in postprocessing of measurements. I am grateful to Prof. Reijo Kouhia and Prof. Laurent Daniel for their support and guidance during the research work.

Moreover, I would like to thank Tampere University for the funding opportunity from the graduate school funds. I would like to thank Paavo Rasilo for providing me the funds to carry out the research work and finalize my thesis. I would also like to acknowledge the Walter Ahlström Foundation and industrial research funds at Tampere University for providing the research encouragement grants.

I am grateful to my colleagues Antero, David, Jay, Joonas, and Yoshito for their support and good times during my journey as a doctoral researcher. I learnt a lot from them and really enjoyed working alongside them as a researcher. I am also thankful to all my friends, especially Danish Khan, Muhammad Uzair Khalid, and Junaid Malik, for being there during tough times.

Last but not least, I would like to thank my lovely family. I express my gratitude to Atiq Iqbal for his mentoring and support. I am thankful to my brother and sister for their assistance, care, and support. I am grateful to my beautiful wife Hallah Noor for encouraging me, loving me, supporting me, and being in my life. I would like to thank Allah Almighty for His countless blessings. Lastly, I would

like to dedicate this thesis to my mother Farooqa Jan, as without her my life would not have been as beautiful as it is today.

Tampere, September 10th, 2023.

Umair Ahmed.

CONTENTS

LIST OF SYMBOLS AND ABBREVIATIONS

Symbols

$\boldsymbol{a}$	nodal values of vector potential in 2D model
A	cross-sectional area
$\boldsymbol{A}$	magnetic vector potential
$\boldsymbol{b}$	direction vector for magnetic flux density
B	magnetic flux density (scalar)
$\boldsymbol{B}$	magnetic flux density (vector)
B_{r}	remanence flux density
B_{ref}	reference value of magnetic flux density
$\boldsymbol{C}$	flux linkage matrix
$\boldsymbol{D}$	source current density matrix
$\boldsymbol{e}$	deviatoric part of strain
E	Young's modulus
$\boldsymbol{e}_{\mathrm{r}}$	unit vector in radial direction
$\boldsymbol{e}_{\mathrm{z}}$	unit vector in axial direction
$\boldsymbol{e}_{\theta}$	unit vector in circumferential direction
f	frequency
f_0	resonant frequency
H	magnetic field strength (scalar)
$\boldsymbol{H}$	magnetic field strength (vector)
H_{air}	region for computing the magnetic field in the air
H_{bar}	region for computing the magnetic field in the bar
H_{c}	coercive field

$\boldsymbol{I}$	second-order identity tensor
i_{coil}	pick-up coil current
I_i	invariant
$\boldsymbol{J}$	Jacobian matrix for Newton-Raphson iteration
$\boldsymbol{J}_{\text{s}}$	source current density
l	length of beam
M	tip mass
m_{eff}	effective mass of beam
N	number of coil turns
$\boldsymbol{N}_i$	vector of finite element nodal shape function
$\boldsymbol{r}$	residual vector in Newton-Raphson iterations
r	radial coordinate
R_{coil}	pick-up coil resistance
R_{load}	load resistance
$\boldsymbol{s}$	deviatoric part of stress
$\boldsymbol{S}$	mechanical stiffness tensor
S_{coil}	coil cross-sectional area
t	time
$\boldsymbol{u}$	displacement vector
V_{ind}	induced voltage
W_{σ}	magnetoelastic energy
x	cross-sectional coordinate
X_k	peak displacement amplitude
y	cross-sectional coordinate
z	axial coordinate
α_i	polynomial coefficient
α_{dM}	mass damping parameter
β_i	polynomial coefficient

β_{dK}	stiffness damping parameter
γ_i	polynomial coefficient
Γ	boundary lines inside the calculation domain
ΔB	flux density variation
Δt	time step length
$\Delta\sigma$	dynamic mechanical stress
ε	mechanical strain (scalar)
$\boldsymbol{\varepsilon}$	mechanical strain (tensor)
ζ	damping ratio
κ	electrical conductivity
λ	magnetostriction
μ_{r}	relative permeability
ρ	mass density
σ	mechanical stress (preload)
$\boldsymbol{\sigma}$	mechanical stress tensor
ν_0	constant reluctivity of free space
ψ	Helmholtz free energy density function
Ω	calculation domain
Ω_{coil}	coil domain

Abbreviations

2D	two-dimensional
3D	three-dimensional
DEA	discrete energy averaged
FE	finite element
FEM	finite element method

ORIGINAL PUBLICATIONS

Publication I Ahmed, U., Jeronen, J., Zucca, M., Palumbo, S. and Rasilo, P., 2019. Finite Element Analysis of Magnetostrictive Energy Harvesting Concept Device Utilizing Thermodynamic Magneto-Mechanical Model. *Journal of Magnetism and Magnetic Materials*, *486*, 165275.

Publication II Ahmed, U., Aydin, U., Zucca, M., Palumbo, S., Kouhia, R. and Rasilo, P., 2020. Modeling a Fe-Ga Energy Harvester Fitted with Magnetic Closure Using 3D Magneto-Mechanical Finite Element Model. *Journal of Magnetism and Magnetic Materials*, *500*, 166390.

Publication III Ahmed, U., Aydin, U., Daniel, L. and Rasilo, P., 2020. 3-D Magneto-Mechanical Finite Element Analysis of Galfenol-Based Energy Harvester Using an Equivalent Stress Model. *IEEE Transactions on Magnetics*, *57*(2), 7400405.

Publication IV Ahmed, U., Blažević, D., Mizukawa, Y., Aydin, U. and Rasilo, P., 2022. Validation of Thermodynamic Magneto-Mechanical Finite-Element Model on Cantilever-Beam type Magnetostrictive Energy Harvester. *Journal of Magnetism and Magnetic Materials*, *564*, 170098.

AUTHOR'S CONTRIBUTION

Publication I Umair Ahmed planned the study, carried out measurements, implemented the model, carried out computational work, and wrote the original manuscript. Juha Jeronen helped with postprocessing of the measurements and provided comments and suggestions. Mauro Zucca developed the prototype device, designed the experimental setup, and provided supervision, comments, and suggestions. Stefano Palumbo developed the prototype device and provided comments and suggestions. Paavo Rasilo applied for funding, participated in the planning of the study, programmed the finite element code, and provided supervision, comments, and suggestions.

Publication II Umair Ahmed planned the study, developed the methodology, performed computational work, investigated the results, implemented the model, and wrote the original manuscript. Ugur Aydin helped in COMSOL implementation and provided comments and suggestions. Mauro Zucca developed the prototype device and experimental setup and provided supervision, comments, and suggestions. Stefano Palumbo performed the measurements and provided comments and suggestions. Reijo Kouhia helped with the model and provided comments. Paavo Rasilo participated in the planning for the study and provided supervision, comments, and suggestions.

Publication III Umair Ahmed planned the study, carried out computational work, investigated the results, implemented the model and wrote the original manuscript. Ugur Aydin performed formal analysis and provided comments and suggestion. Laurent Daniel developed the model and provided comments and

	suggestions. Paavo Rasilo participated in the planning of the study and provided supervision, comments, and suggestions.
Publication IV	Umair Ahmed developed the prototype device and experimental setup, performed measurements, implemented the model, carried out computational work and wrote the original manuscript. David Blažević participated the planning of the study and provided comments and suggestion. Yoshito Mizukawa investigated the measurement results and provided comments and suggestions. Paavo Rasilo provided funding, participated in the planning of the study, and provided supervision, comments, and suggestions.

1 INTRODUCTION

This chapter provides an introduction to the thesis and discusses the motivation behind this research. The chapter also lists the specific research questions to be answered by this thesis. The scientific contributions of the thesis are listed from the viewpoint of Publications I–IV in a chronological order, and an outline of the thesis is presented at the end.

1.1 Introduction and motivation

Attention towards the concept of magnetostrictive energy harvesting has increased significantly in the past decade, enabling maintenance and battery-free operation of low-power microelectronic devices and sensors. The magnetostrictive energy harvester utilizes ambient vibrations that are considered wasted otherwise and converts them into electrical energy. Magnetostrictive materials utilized by such energy harvesters show microscopic change in their shape when they are subjected to an external magnetic field. Furthermore, the magnetic behavior of the magnetostrictive materials changes under the application of mechanical loading. Therefore, the magneto-mechanical properties of the magnetostrictive materials need to be studied for analyzing and designing the magnetostrictive energy harvesters. Modeling tools are needed to investigate the coupled magneto-mechanical phenomenon in the magnetostrictive materials in order to analyze, design, and optimize the energy harvesters.

Deriving phenomenological nonlinear constitutive laws of magnetostrictive materials generally requires deriving an energy function. The energy-based models utilizing a thermodynamic approach are mainly categorized into two types. The first type of models utilizes Gibbs free energy that measures useful work (given by mechanical and magnetic contributions) from a closed thermodynamic system at constant temperature and pressure. The second type of models utilizes Helmholtz free energy which measures useful work from a closed thermodynamic system at constant temperature and volume. Various state-of-the-

art energy-based phenomenological models have been developed by previous researchers utilizing Gibbs free energy to describe the coupled magneto-mechanical behavior of magnetostrictive materials. These models utilize stress and magnetic field as the state variables whereas strain and magnetic flux density are state functions. This thesis presents two different constitutive modeling approaches to analyze magneto-mechanical behavior of giant magnetostrictive material galfenol[1] used as an active material in energy harvesters. The first approach uses Helmholtz free energy to analyze the galfenol-based magnetostrictive energy harvester. The second approach uses an equivalent stress model that offers a simplified modeling approach to predict the operation characteristics of magnetostrictive energy harvester. The Helmholtz free energy-based model has been validated previously to successfully predict the magnetoelastic behavior of electrical steel sheets used in electrical machines. In this work, the model is utilized for the first time to analyze giant magnetostrictive material-based energy harvesters. Moreover, contrary to some earlier approaches, the model utilizes magnetic flux density and strain as state variables. This simplifies the implementation of FE models based on magnetic vector potential and mechanical displacement since time-consuming inversion of the constitutive law is not required.

The aim of the thesis is to provide a modeling approach that can be utilized to analyze various geometric configurations of energy harvesters. Since most existing models have been validated on a single specific geometry of the harvester, it is unclear whether they are applicable for analyzing energy harvesters with different geometries (such as rod-type and cantilever-beam-type). This provides the motivation to find a modeling approach that is capable of analyzing both rod-type and cantilever-beam-type prototype energy harvesters. To achieve this, the energy-based magneto-mechanical model is validated on different prototype geometries including a rod-type energy harvester, a rod-type energy harvester fitted with a magnetic core, and a cantilever-beam-type energy harvester. This thesis also highlights the influence of the sensitivity and repeatability of the measurements when comparing the discrepancies among simulated and measured results for model validation.

[1] The first letter of galfenol is not capitalized considering it's an alloy of two common metals, iron and gallium.

1.2 Research questions

The specific research questions to be answered in this thesis are:

1) How accurately can the thermodynamic magneto-mechanical model reproduce the stress-dependent magnetization curves for galfenol?
2) Can a finite element implementation of the thermodynamic model successfully predict the operation characteristics for different geometric configurations of the magnetostrictive energy harvesters?
3) How accurate is the finite element implementation of the equivalent stress model compared to the thermodynamic model?
4) What is the significance of the sensitivity and repeatability of the measurements in validating the models? What can be done to improve the repeatability of the measurements?

1.3 Scientific contributions

The main scientific contributions of the thesis are listed below. The scientific contributions are presented in a chronological order as the research progressed.

- A thermodynamic magneto-mechanical model based on Helmholtz free energy density function is utilized for the first time to analyze magnetostrictive energy harvesters.
- The thermodynamic model is first implemented in a 2D axisymmetric finite element model to demonstrate the model's capability to reproduce the experimental results. The model is validated against measurement results obtained from a rod-type galfenol-based prototype energy harvester. It is shown that the model is able to reasonably predict the output power of the energy harvester under varying amplitudes of mechanical loading. Furthermore, the model is also able to predict the optimal value of the load resistance yielding maximum output power.
- Complete understanding of the magneto-mechanical phenomenon in magnetostrictive materials require 3D fully coupled magneto-mechanical finite element model. To achieve this, the magneto-mechanical constitutive equations derived utilizing the thermodynamic model are implemented in COMSOL Multiphysics for 3D finite element analysis of the magnetostrictive energy harvesters. The capability of the commercial software COMSOL is

tested in order to implement the custom constitutive model. It is demonstrated that the model can analyze the modified geometric configuration of the energy harvester. This is done by adding a magnetic core to the rod-type protype energy harvester and changing the position of the permanent magnets. It is shown that the model is able to successfully predict the influence of mechanical and magnetic bias over the output power and can be used to analyze the magneto-mechanical behavior of the energy harvester.

- An equivalent stress model is utilized for the first time to analyze a magnetostrictive energy harvesting device. The equivalent stress model is implemented in COMSOL for 3D finite element analysis of a rod-type galfenol-based prototype energy harvester fitted with a magnetic core. The model provides a simplified approach to predict the permeability of the galfenol material based on uniaxial measurements. It is shown that the model is able to reasonably predict the output power under different magnetic field biases and mechanical loading conditions. A direct comparison between the thermodynamic model and equivalent stress model is also presented.
- The thermodynamic model is tested on a cantilever-beam-type galfenol-based prototype energy harvester. It is demonstrated that the model is able to accurately predict the resonant frequency of the cantilever beam under different amplitudes of the mechanical vibrations. Furthermore, it is shown that the resonant frequency of the cantilever beam changes due to magnetostriction. The model successfully captures the effect of magnetostriction on the resonant frequency.

1.4 Thesis outline

Chapter 2 provides a detailed overview of the energy harvesting concept and techniques. State-of-the-art magneto-mechanical models analyzing the coupled magneto-mechanical phenomenon in ferromagnetic and magnetostrictive materials are discussed. The application of state-of-the-art models to analyze magnetostrictive energy harvesters is presented. In Chapter 3, the experimental setups of the prototype energy harvesters are presented. The chapter also discusses the constitutive and finite element models utilized for analyzing the prototype energy harvesters. Chapter 4 summarizes the results from Publications I–IV and provides arguments and discussions. Chapter 5 presents concluding remarks and discussion related to future work.

2 LITERATURE REVIEW

This chapter provides an overview of the previous research in the area of modeling and design of magnetostrictive energy harvester devices. The chapter starts by presenting the phenomenon of magnetostriction and the concept of magnetostrictive energy harvesting. The properties of various giant magnetostrictive materials are discussed to justify the choice of the active material used in this research. The emphasis and need of magneto-mechanical models in designing and analyzing the energy harvesters are presented. The chapter ends with a detailed overview of the state-of-the-art in modeling the coupled magneto-mechanical phenomenon of magnetostrictive energy harvesters.

2.1 Magnetostriction

The concept of magnetostriction was first discovered in 1842 by James Joule when he observed that ferromagnetic materials undergo microscopic change in their shapes under the application of an external magnetic field. The ferromagnetic material consists of magnetic domains in which magnetic dipoles are present. The magnetic domains are randomly aligned under the absence of magnetic field. When an external magnetic field is applied, the magnetic moments rotate and align themselves in the direction of the applied magnetic field pushing the walls between the domains. The alignment of magnetic domains produces microscopic change in the length and width of the material shown in Figure 2.1, whereas the overall volume remains constant [1]. The change in length is shown

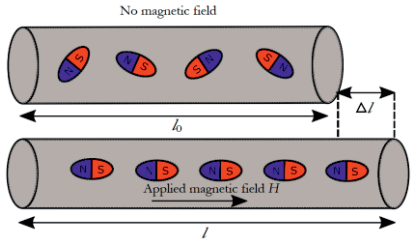

Figure 2.1 The process of magnetostriction in ferromagnetic materials.

as Δl, which causes strain due to magnetostriction. The amount of magnetostrictive strain in magnetostrictive materials including nickel, cobalt and iron is below 30 ppm at room temperature [2], [3]. A class of rare earth metals was discovered in the early 1970s at the US Naval Ordinance Laboratory, showing large magnetostriction in the order of 5000 ppm. These are referred to as giant magnetostrictive materials. This discovery led to the development of new alloys combining the properties of rare earth metals with transition metals such as cobalt, nickel and iron. The giant magnetostrictive materials are utilized in sonar applications, as micro-actuators, as vibration suppression devices, and for energy harvesting purposes [3], [4].

2.2 Giant magnetostrictive materials

Some of the most popular giant magnetostrictive materials are discussed here in order to provide a comparison among the material characteristics, including their magnetic and mechanical properties. It is important to select a suitable material for energy harvesting applications; this selection was made after reviewing the literature from previous researchers and going through the material properties at the beginning of the research.

2.2.1 Terfenol-D

Terfenol-D is an alloy of iron (Fe) and rare earth metals dysprosium (Dy) and terbium (Tb). Dysprosium and terbium show large magnetostriction (~5,000 ppm) but only at cryogenic temperatures which reduces significantly at room temperature [4]. However, when they are combined with iron, they form a compound alloy Terfenol-D that can provide large magnetostriction under temperatures ranging from -200 $^{\circ}$C to 200 $^{\circ}$C in the presence of an external magnetic field. At room temperature, Terfenol-D of stoichiometry $Tb_{0.3}Dy_{0.7}Fe_{1.92}$ shows saturation magnetostriction of 1640 ppm with saturation magnetic field of 160 kA/m. Terfenol-D has a Curie temperature of 380 ^{0}C and a Young's modulus of 90 GPa. However, the material is brittle in nature, with tensile strength ranging from 22 to 40 MPa and compressive strength ranging from 300 to 880 MPa [2], [3], [5].

2.2.2 Galfenol

Galfenol is an iron and gallium (Ga) alloy that was discovered in 1990 in a research collaboration with the Naval Surface Warfare Centre and the United States Department of Energy's (DOE) Ames Laboratory. The motivation behind the discovery was to obtain a giant magnetostrictive material that has steel-like mechanical properties and shows large magnetostriction [5]. At room temperature, galfenol of stoichiometry $Fe_{81.6}Ga_{18.4}$ shows saturation magnetostriction of ~350 ppm at saturation magnetization of just ~10 kA/m. galfenol has a high Curie temperature of 670 ^{0}C and a Young's modulus of 75 GPa. The material is ductile in nature and has a tensile strength of 350 MPa. Since galfenol has steel like structural properties, it can be easily machined and welded into different shapes [6], [7].

2.2.3 Metglas 2605SC

Metglas are amorphous iron-based soft magnetic alloys that were discovered in 1970s [7]. The material is mostly used in high-frequency applications because of its low iron losses and high permeability. In most applications, Metglas is used in the form of metal sheets or foils due to its softness and ease of machinability. The material shows magnetostriction of 60 ppm at room temperature and has a high tensile strength of ~1-2 GPa. The Curie temperature is 370 ^{0}C with a Young's modulus of 100 – 110 GPa [2].

The material properties of the giant magnetostrictive materials discussed above provide the justification to use galfenol as an active material for this research. The reason for choosing galfenol is that it has comparatively high compressive and tensile strength compared to Terfenol-D and it shows large magnetostriction compared to Metglas. The coupling coefficient of Terfenol-D is higher than that of galfenol [8], but Terfenol-D is brittle in nature. On the other hand, galfenol is pliable and demonstrates large magnetostriction over a wide temperature range. Most importantly, it can be welded and machined easily, making it suitable for energy harvesting applications. Although, Terfenol-D has the largest magnetostriction of all the materials discussed, but it cannot survive under strong ambient vibrations of stochastic nature due to its brittleness. Furthermore, Terfenol-D cannot be machined easily, making it difficult to incorporate into various geometries of the energy harvester [9].

2.3 Energy harvesting concept, techniques and applications

The development in technology, such as wireless communication networks, microcontrollers, and sensors, has placed pressure on the energy demand for powering up such devices [10]–[12]. The predominant source of energy for such devices is electrolytic batteries or rechargeable cells, which require frequent maintenance and replacement. Another issue is the scarcity of natural resources to manufacture batteries and the environmental issues related to their disposal. This demands a solution that could replace the batteries and make such systems autonomous. One possible solution is to utilize energy harvesters for power supply [13], [14]. The energy harvester utilizes ambient vibration sources that are otherwise considered wasted and converts them into electricity. The vibration sources could originate from, for example, long cables from steel bridges, speed breakers, human motion, rotating or moving parts of machines, airplane wings, rail tracks, or blades of a wind turbine, etc. However, the ambient vibrations are stochastic in nature with the narrowband and broadband frequency range. Therefore, the energy harvesters require an energy management system where the electrical energy from mechanical vibrations is first accumulated into a supercapacitor or some storage device before it is supplied to the sensors or micro-electronic devices [10]–[15]. The steps involved in energy harvesting are presented in Figure 2.2, showing the whole process from source to supply. Energy harvesters are meant to power up small-scale loads having the power requirement of hundreds of milliwatts. They provide the advantage of an autonomous and battery-free system [16], [17]. Long cabling is not needed, since the power is supplied locally and the information is transferred wirelessly through wireless sensors nodes [18]–[20]. This reduces wire losses, and the fault detection also becomes easier.

Some of the typical applications of energy harvesting devices discussed in previous literature involve structural health condition monitoring for bridges [21]

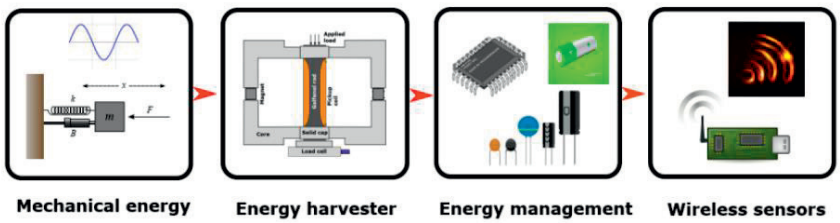

Figure 2.2 Steps involved in energy harvesting process from mechanical vibrations.

in the aviation industry [22], [23], for railway tracks [24], [25], and floor vibrations from machines in industries [26]. Some of the interesting application of energy harvesters are supplying power to wireless sensor networks for Internet of Things applications [27], [28], powering up sensors and wireless tags for domestic animals [29], [30], agricultural and biomedical applications [31]. Moreover, the energy harvesters can also be used as vibration suppression devices, as discussed in [32]. Various energy harvesting techniques converting mechanical vibrations into electrical energy are discussed here briefly. Popular techniques include electrostatic, piezoelectric, electromagnetic, and magnetostrictive energy harvesting [18]–[21], [26], [31].

2.3.1 Electrostatic energy harvesting

In electrostatic energy harvesting, electric charge is stored between two parallel capacitive plates, creating a potential difference. The harvesting process involves fixing one plate while moving the other using mechanical vibrations. This can also be achieved using a variable capacitor, where plates are configured as two parallel sets of moving combs, as discussed in [19]. A detailed review of various configurations of electrostatic energy harvesters is presented in [18] and [20]. Electrostatic energy harvesters can be built using low-cost materials and have a longer lifespan as compared to piezoelectric energy harvesters [19], [31]. However, they produce high output voltage, which needs to be stepped down before supplying to the load. There are also mechanical limitations in controlling the distance between the capacitors and need an external voltage source [18]–[20].

2.3.2 Piezoelectric energy harvesting

In piezoelectric energy harvesting, electric charge is created by direct actuation of the piezoelectric material. Piezoelectric energy harvesters commonly use a cantilever-beam-type device structure that consists of layers of piezoelectric materials attached to a substrate in unimorph or bimorph configurations. When the beam is subjected to dynamic mechanical vibrations, the mechanical energy is converted into electrical energy. The advantage of piezoelectric energy harvesting is the design simplicity, smaller size, and higher energy density compared to electrostatic energy harvesters [20]. Moreover, unlike the

electrostatic energy harvester, it does not require any external voltage source. However, this technique suffers from the fatigue caused by mechanical stress and therefore has a shorter lifespan and also has low coupling coefficient [31], [33]. The piezoelectric effect was discovered in 1880 and, ever since, many piezoelectric materials, including gallium arsenide, lead zirconate titanate (PZT), aluminum nitride, nanogenerators zinc nanowires (ZnO), and polymer polyvinylidene fluoride (PVFD), have been discovered as discussed in detail in [34], [35].

2.3.3 Electromagnetic energy harvesting

In electromagnetic energy harvesting, mechanical energy is converted into electrical energy by the motion of a magnet close to a pickup coil. The electromagnetic energy harvesting technique works on the principle of Faraday's law of electromagnetic induction [34]. A simple geometry of an electromagnetic energy harvester is presented in [27], [36], where a magnet levitates between magnetic springs placed inside a tube. The vibration causes the central magnet to oscillate inducing voltage due to change in the magnetic flux seen by the pickup coil. These kind of energy harvesters are most suited for low-frequency vibrations and do not require an external voltage source. However, their size can limit their application in small-scale power electronic devices. Moreover, the downscaling of the harvester would result in additional damping due to friction, parasitic electromagnetic interference and low output voltage levels [18], [27].

2.3.4 Magnetostrictive energy harvesting

As discussed in Section 2.1, when a magnetostrictive material is subjected to an external magnetic field, the material undergoes microscopic change in the shape caused be magnetostrictive strain. The displacement caused by magnetostriction is in the order of micrometers and varies from 60–1500 ppm for different magnetostrictive materials, presented in detail in Section 2.2 [2]–[7]. Magnetostrictive energy harvesters utilize giant magnetostrictive materials as an active material. The energy harvesting technique utilizes an inverse magnetostrictive phenomenon, also known as the Villari effect, which was discovered by Emilio Villari. The Villari effect is defined as a change in the magnetic susceptibility of a ferromagnetic material when it is subjected to an

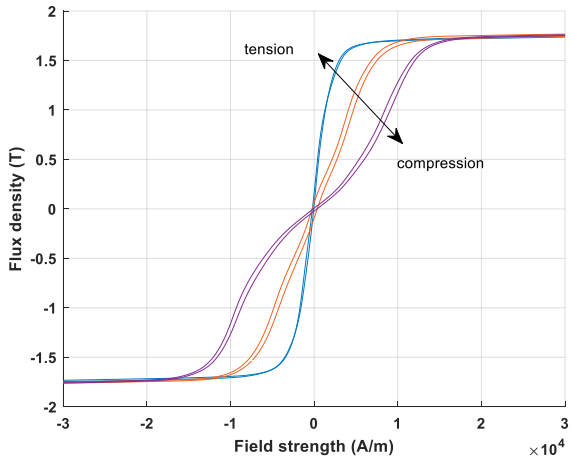

Figure 2.3 Measured *B* – *H* curves under tensile and compressive stress.

external mechanical loading [6], [7]. The change in the magnetization of the material under compression and tension can be seen in Figure 2.3, which shows that the permeability of the material decreases under compressive stress and increases under tensile stress.

In the magnetostrictive energy harvesting technique, the active material is first magnetized using permanent magnets and then subjected to dynamic mechanical excitations; this produces time-varying magnetic flux inside the material. A voltage is induced in the pickup coil wound around the material due to Faraday's law of electromagnetic induction [6], [7], [37]. It has been observed experimentally that stress annealing of the magnetostrictive materials enhances their performance and generates higher output power [38].

Piezoelectric and electromagnetic energy harvesting techniques have received most attention in the literature due to their simpler device design and ability to harvest power at lower frequencies (less than 10 Hz). There are merits and demerits of each energy harvesting technique, as discussed in the literature above. However, due to shorter lifespan of piezoelectric materials, size constraints, low coupling coefficient, fatigue constraints, and technical difficulties due to manufacturing tolerances in electromagnetic, electrostatic and piezoelectric energy harvesting techniques, the focus of this research is inclined towards magnetostrictive energy harvesting. Magnetostrictive materials offer strong magneto-mechanical coupling, high energy conversion efficiency, more durability due to their high mechanical strength (galfenol, alfenol and Metglas etc.) and lack of depolarization. However, magnetostrictive energy harvesters are not suitable for low-frequency vibrations and require bulky magnets and pickup

coils to produce sufficient voltage levels. An optimal compressive pre-stress is required to ensure that maximum magnetostriction is obtained. This generally is not an issue since it can be achieved by material stress annealing. Magnetostrictive energy harvesters are inherently nonlinear due to their nonlinear material properties. Furthermore, due to high material costs, they can be more expensive as compared to piezoelectric and electromagnetic energy harvesters.

The upcoming section provides a detailed overview of magnetostrictive energy harvester prototypes and their geometric configurations developed in the previous literature.

2.4 Magnetostrictive energy harvester prototypes

After the discovery of giant magnetostrictive materials, the research on magnetostrictive energy harvesting has predominantly increased and various prototype devices have been developed as proofs of concept. Mainly, rod-type and cantilever-beam-type energy harvester prototype configurations are adopted in the previous literature, and therefore this research also studies and adopts similar kind of harvester geometries. The prototype energy harvesting devices developed and tested by previous researchers are discussed here briefly.

2.4.1 Cylindrical rod-type harvester configuration

Clamente in [38] and Adly in [39] have presented a cylindrical rod-type prototype energy harvesting devices utilizing galfenol and Terfenol-D as the active materials. The device design and working principle of the rod-type magnetostrictive energy harvester developed by Clamente in [38] are presented in Figure 2.4. A stress annealed galfenol rod of 5 mm diameter and 30 mm length was magnetized using permanent magnets with the help of the iron cores as shown in Figure 2.4. The rod was subjected to sinusoidal mechanical vibrations, which results in an induced voltage into the pickup coil as a result of Faraday's law discussed in Section 2.3.4. The proposed harvester in [38] can generate up to 3 µW of peak power using a 20 Ω load resistance under 0.5 Hz mechanical frequency, whereas an average power of approximately 450 µW was obtained under 50 Hz mechanical frequency when Terfenol-D rod is compressively stressed at 8 MPa [39]. Terfenol-D and galfenol-based rod-type energy harvesters

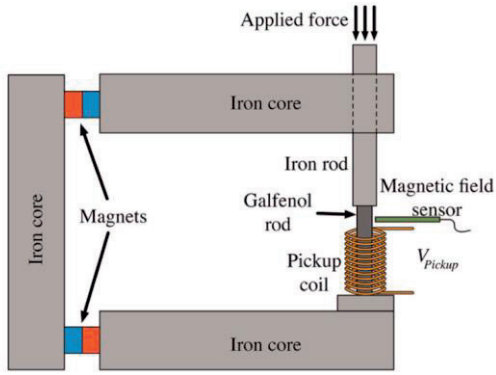

Figure 2.4 The device design and working principle of a cylindrical-rod-type galfenol-based magnetostrictive prototype energy harvester [38].

are presented in [40]–[44]. The harvester proposed in [40] can harvest power from passing vehicles on the road. It has been demonstrated experimentally that the harvester can generate a peak open circuit voltage of 96 mV using a pick-up coil of 1000 turns under an impulse of 0.1 s generated by an axial load of 100 kg. The harvester has a power density of 0.01 W/m^2. Furthermore, it is demonstrated that the output power changes as a function of static preload, dynamic load, magnetic field bias, and load resistance. In [41], [42], Zucca demonstrated the effect of preload, dynamic load, load resistance, frequency of mechanical vibrations and magnetic field bias on rod-type energy harvesters utilizing Terfenol-D and galfenol as active materials.

Extensive sets of experiments have been carried out to determine the influence of the magnetic bias and mechanical excitation. The Terfenol-D based rod-type harvester in [41] can produce 8 mW of power at 300 Hz frequency when a preload of 3.8 MPa and dynamic load of 1.05 MPa are applied. This output power can be increased to 82.8 mW by tuning the static preload, load resistance, and pickup coil parameters (wire thickness and coil turns). In [42], Palumbo analyzed the performance of a rod-type galfenol-based energy harvester under varying mechanical excitations, magnetic field bias and load resistance. Their study suggests that these parameters need to be optimized individually when designing the energy harvester for a specific application. The proposed harvester could produce 45 mW of average output power under 55 MPa preload and 8 MPa dynamic loading at an optimal load resistance of 160 Ω. During the experiment, the magnetic field bias was applied using permanent magnets, whereas the mechanical excitation frequency of 100 Hz was utilized. Fang in [43] integrated a Terfenol-D based rod-type energy harvester with a nonlinear energy damper to

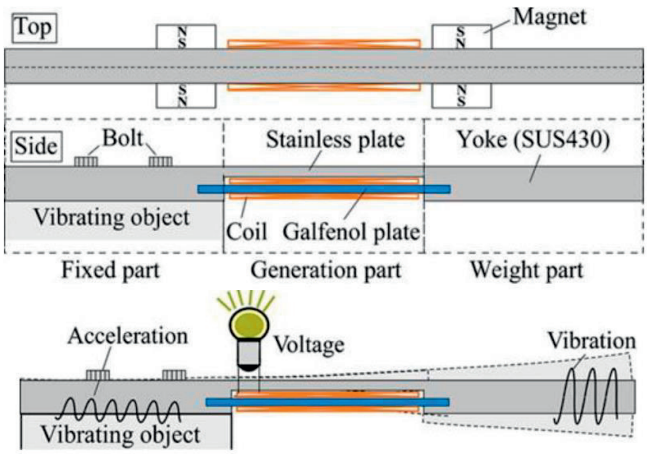

Figure 2.5. The device design and working principle of a cantilever-beam-type galfenol-based magnetostrictive energy harvester [45].

realize an energy harvester with vibration damping capabilities. Berbyuk in [44] presented a galfenol-based rod-type energy harvester, and the operating conditions were optimized to obtain 450 mW of power using 50 Hz excitation frequency.

2.4.2 Cantilever-beam-type harvester configuration

Cantilever-beam-type energy harvesters utilizing galfenol or Terfenol-D as the active material are presented in [45]–[51]. Cantilever-beam-type energy harvesters are typically configured as unimorphs or bimorphs. In unimorph configuration, the cantilever beam consists of a single layer of an active material that is attached to a non-magnetic substrate for mechanical support, known as a passive layer, as discussed in [45]–[50]. Bimorph configuration consists of two layers of active material attached to a substrate discussed in [51], [52]. In [45], Kati demonstrated the effect of output power upon changing the beam dimensions. The device design and working principle of a cantilever-beam-type prototype energy harvester developed by Kati in [45] is presented in Figure 2.5. The harvester consists of a parallel beam of galfenol and stainless plates. A pickup coil of 1605 turns is wound around the galfenol beam, and the galfenol beam is then joined to the yoke firmly by adhesive. The fixing part is used to fix the generator on a vibrating object by bolts. The harvester is then attached to a shaker to provide sinusoidal mechanical vibrations. A maximum power of 5.4 mW was

obtained using a load resistance of 80 Ω under free vibration frequency test when the beam width is 7 mm with a length of 100 mm and height of 3 mm. The effect of vibration amplitude and frequency over the output power is demonstrated in [45], [49], and [50]. Those studies concluded that the output power increases with the increase in acceleration amplitude from 1g to 4g where g = 9.81 m/s^2 is the gravitational acceleration. Moreover, the resonant frequency of the beam can be tuned for performance optimization by changing the tip mass or modifying the beam dimensions. An output power of 0.25 mW is obtained in [48] at resonant frequency of 238 Hz, whereas an output power of 16 mW is obtained in [49] at resonant frequency of 222 Hz when the gravitational acceleration is 4g in both cases. In [52], Uneo analyzed the performance of a bimorph cantilever beam utilizing galfenol material and obtained a peak output power of 2 mW of from free vibrations at resonant frequency of 392 Hz.

2.5 Modeling of magnetostrictive materials and devices

The literature presented above provides an understanding regarding the concept of energy harvesting and discusses some well-known magnetostrictive materials that have been utilized to harvest energy from mechanical vibrations. The energy harvesting techniques have been discussed in detail along with the proofs of concept prototype devices developed in the previous literature. It has been argued that the energy harvesters utilize ambient vibration sources that exist naturally in the environment for which the amplitude and frequency cannot be controlled. Furthermore, the energy harvesters should be able to supply the required output power, which depends on the type of load (sensors, microelectronics, etc.). Therefore, mathematical models and simulation tools are needed in order to analyze, design, and optimize an energy harvester device to obtain the maximum output power.

The design process of an energy harvester involves understanding the properties of the active material (stress-dependent magnetization curves and material strain due to magnetization) and knowledge related to the nature, amplitude and frequency of mechanical vibrations. The development of an energy harvester includes determining the suitable operating conditions (static mechanical preload, dynamic mechanical load and magnetic field bias) and design parameters (device geometry, load resistance and pick-up coil parameters). Based on the ambient source of vibrations, the operating conditions and the design

parameters are modified in order to design an energy harvester device that is suitable for a specific application. The magnetic bias is applied using permanent magnets, whereas the preload (static stress) can be applied through tightening a bolt or directly induced into the material by stress annealing. In stress annealing process, the material is first prestressed under heat and then cooled down to room temperature leaving permanent stress into the material [53], [54]. In [54], Michael showed that large magnetostriction can be achieved at zero preload condition by stress annealing the galfenol material to induce 55 MPa compressive stress.

There are two typical approaches to design and develop a prototype energy harvester device. The first approach is to develop the prototype using a trial-and-error method, whereas the second approach is to utilize modeling and simulation tools to first analyze the prototype harvester device before developing the actual prototype. Because the former approach requires significant time and resources, the latter approach is considered more suitable for designing energy harvester devices. Various models have been developed in the literature to analyze and design the prototype energy harvester concept devices. Most models utilize the finite element (FE) method to solve for the magneto-mechanical interaction inside the material and analyze the behavior of the active material under changing operating conditions and design parameters. The developed magneto-mechanical models are introduced briefly here to provide motivation for the need for modeling and simulation tools.

2.5.1 Magneto-mechanical models

The Preisach and Jiles-Atherton models are some of the popular constitutive models that have been developed to determine the electromagnetic behavior of the ferromagnetic materials incorporating material hysteresis introduced in 1935 and 1986 [55], [56]. These models were later modified to include the coupled magneto-mechanical behavior of the materials, as discussed in [57]–[61]. Bottauscio in [60] tested a modified Preisach-based model to incorporate the magnetoelastic behavior of Terfenol-D utilizing FE simulations. The implemented model can exploit the dynamic characteristic of Terfenol-D as an actuator. The research concerning 2D and 3D magneto-mechanical modeling of magnetostrictive materials is discussed in [57]–[67] and [79]–[81]. In [62], Zhou developed a 2D magneto-mechanical FE model to simulate a vibration suppression device comprising a giant magnetostrictive material. In [63],

Chakrabarti presented a 2D axisymmetric FE model of a hydraulically amplified magnetostrictive actuator for active power train mounts implemented in COMSOL Multiphysics. The actuator consists of a piston operated by Terfenol-D rod in a fluid chamber. The magnetic bias is applied by permanent magnets. The model utilizes Maxwell and Navier Stokes equations representing the electromagnetic and mechanical system coupled through a nonlinear magneto-mechanical constitutive law.

Energy-based phenomenological models describing the magneto-elastic properties of the magnetostrictive materials are presented in [64]–[71]. Evans and Dapino in [64] presented a linearized discrete energy-averaged (DEA) model that calculates the magnetization directions of mesoscopic magnetic domains by minimizing the locally defined Gibbs free energy to the easy axes. The magneto-mechanical model provides a hysteretic relationship between magnetic field and stress versus magnetization and strain. The model is further modified by Dapino and Chakrabarti in [65], where the dynamic magnetic response of a unimorph galfenol actuator is described by implementing an anhysteretic 3D DEA model. The model takes the 1D material characterization as the input parameters and calculates the 3D constitutive model parameters. Chakrabarti [66] utilized the DEA model to analyze the anisotropic behavior of the Terfenol-D material incorporating the nonlinearity and hysteresis of the material. The model is validated for sensing and actuation measurements and the model parameters are obtained from the anhysteretic magnetization curve. The modeling approach in [65] is further improved by calculating the exact analytical expression of the magnetostriction tensor and providing a simplified version of Gibbs free energy [67]. The modified DEA model can calculate the 3D hysteretic magnetization and magnetostriction of galfenol material. The reduced order model is also presented for 2D plane stress and 1D axial loading applications. Belahcen and Fonteyn proposed a directly coupled magneto-mechanical model utilizing a thermodynamic approach in [68] and [69]. The model is based on deriving a suitable form of the Helmholtz free energy density presented in [68]. The energy-based model is implemented using the 2D finite element model (FEM) to simulate the effect of magnetostriction causing stress in an electrical machine. Slightly modified versions of the Helmholtz free-energy-based magneto-mechanical models were later presented in [70], [71], [72]. The proposed models are utilized to analyze the behavior of iron sheets under biaxial loading [70] and to determine losses in ferromagnetic laminations under uniaxial mechanical stress [71].

The applications involving multiaxial loadings caused by rotation or torsion require models to account for multiaxial stress or strain. In most cases, the developed magneto-mechanical models are validated against the measurements obtained under uniaxial loading. In [73], Daniel proposed an equivalent stress model to analyze the effect of multiaxial stress on magnetic behavior of the ferromagnetic material. The equivalent stress model is based on describing the equivalence in terms of magnetoelastic energy. The model can transform complex multiaxial loadings into a uniaxial one in the direction parallel to the applied magnetic field. The model is validated on iron-cobalt laminations under biaxial loadings [73], [74] and later utilized for modeling the magnetic hysteresis losses under biaxial loading for electrical machine steel sheets in [75]. Fully multiaxial magneto-mechanical models are discussed in [76], [77]. The multiaxial model in [76] describes the magneto-elastic coupling at the magnetic domain scale utilizing an equivalent stress approach based on [73] and [74]. A simplified approach for modeling the magneto-mechanical behavior of magnetic materials was proposed in [77] based on the multiscale model presented in [76]. The simplified model offers low computation time and can be implemented in FE models for designing the electromagnetic devices. The model is able to describe the magnetostriction and magnetization curves under various magneto-mechanical loading configurations. An equivalent strain model was later presented in [78] based on the equivalent stress model in [73]. It was concluded in [76] and [78] that the models can reasonably determine the effect of stress on magnetic behavior, but cannot replace the physical-based constitutive models capable of accurately describing the magneto-elastic behavior of the material.

In [79], Mudivarthi presented a bidirectionally coupled magneto-mechanical model implemented coupled with a 3D nonlinear FE model to predict the strain caused by magnetic flux density in a galfenol beam attached to aluminum substrate. This model was extended to incorporate the induced electric currents and additionally evaluate the change in Young's modulus in the galfenol rod [80]. An analytical magneto-mechanical model validated under a constant weak magnetic field utilizing a thermodynamic framework and anhysteretic magnetization is presented in [81]. The models discussed in [57]–[67] and [79]–[81] provide an understanding of magneto-mechanical interaction inside the magnetostrictive materials. They are validated for devices utilized as active transducers, vibration suppressors, and sensing applications. However, they have not been utilized for analyzing the magnetostrictive energy harvesting devices.

2.5.2 Model applications for energy harvesters

For energy harvesting applications, modeling tools are required to investigate the coupled magneto-mechanical phenomenon in the magnetostrictive material in order to determine the optimal operating conditions and design parameters. Various models developed in previous literature to analyze and design the energy harvesters utilizing magnetostrictive materials have been presented in [37], [38], [49]–[51], and [82]–[89]. Models utilizing a linearized approach are discussed in [49] and [82]. In [49], Yoo utilized 1D linearized piezomagnetic constitutive equations describing the magneto-mechanical behavior of a cantilever-beam-type prototype energy harvester. In [82], Zhao presented a linearized magneto-mechanical model that also includes the effect of eddy currents on the output power. The linearized models can be utilized to analyze materials with low hysteresis losses such as galfenol. Palumbo and Rezaeealam, in [42] and [83] have experimentally shown that galfenol exhibits negligible hysteresis. A fully coupled nonlinear phenomenological model describing the magneto-mechanical interaction in material incorporating hysteresis losses is presented in [37]. The model utilizes a Preisach-based phenomenological modeling approach to analyze a Terfenol-D based rod-type prototype harvester with a larger hysteresis than galfenol. Models developed to analyze rod-type galfenol-based energy harvesters are discussed in [38], [83], [84], [88], and [89]. The model in [83] is based on Armstrong's energy-based modeling approach utilizing an anhysteretic modeling technique to analyze a rod-type galfenol-based energy harvester. A Gibbs free-energy-based nonlinear magneto-mechanical model presented in [38] proposes an equivalent magnetic and mechanical circuit for analyzing the magneto-mechanical effects in galfenol rod. The model in [38] was later utilized to develop a three-port equivalent circuit model to couple the mechanical, magnetic and electric quantities together [88]. The model is tested under sinusoidal vibrations on single-rod and three-rod energy harvester geometries utilizing galfenol as the active material. At a later stage, the fully coupled nonlinear magneto-mechanical model is implemented in COMSOL Multiphysics for 3D FE simulations in [89]. The model involves Solid Mechanics, Magnetic Field and Electric Circuit -physics, and the constitutive laws are implemented through the Ordinary Differential Equations and Differential Algebraic Equations -interface. The model is validated against measurements from a three-rod galfenol-based prototype energy harvester device under impact vibrations. Analytical models developed to analyze a cantilever-beam-type galfenol-based energy harvesters are

discussed in [49]–[51], [62], [85]–[87]. For the cantilever-beam-type harvester geometry, the performance of the harvesters relies on the beam resonant frequency, coil parameters, load resistance, stress annealing of the material, and material magnetization. The proposed models are tested under specific mechanical loading and magnetic bias conditions. The resonant frequency, magnetic bias, and coil parameters are varied to study their influence. The simulated open circuit voltage and output power are then compared with measured results for model validation.

2.6 Summary

The literature review provided a systematic overview of the research topic, starting with introducing the concept of magnetostriction, classifying magnetostrictive materials, and discussing in detail the energy harvesting techniques and developed prototype energy harvester devices. Finally, state-of-the-art magneto-mechanical models developed by previous researchers and their application for analyzing the prototype energy harvester devices have been presented. It is important to note that most models have been validated on a single specific type of harvester geometry and have not been shown to be applicable for analyzing the influence of rod-type and cantilever-beam-type energy harvester geometries. Moreover, not all models were tested to analyze the effect of varying operating conditions (mechanical preload, dynamic load, magnetic bias and resonant frequency) and design parameters (harvester's geometry, load resistance and coil parameters) upon energy harvester performance. This thesis presents an energy-based magneto-mechanical constitutive model [69], [72], utilizing a thermodynamic approach to analyze the galfenol-based magnetostrictive prototype energy harvesters. Furthermore, an equivalent stress model presented in [73], [74] has been utilized for the first time to analyze a magnetostrictive energy harvester. The models have been validated against measurements obtained from a rod-type and cantilever-beam-type prototype energy harvesters. The models have been demonstrated to successfully analyze the influence of varying operating conditions and design parameters upon the harvester's output power.

3 METHODS

The methodology of the research work is divided into two parts. The first part deals with the experimental setups and measurements of the prototype energy harvesters developed in Publications I–IV. The second part discusses the magneto-mechanical constitutive models and FE models to analyze the developed prototype energy harvesters under various operation conditions and design parameters.

3.1 Experimental setups

The experimental setups are further categorized into two parts. The first part deals with the material characterization. The second part deals with the energy harvesting setups, utilizing different geometric configurations of the prototype energy harvester devices. In this research, the geometric configurations adopted for the development of prototype energy harvesters are rod-type and cantilever-beam-type geometries. The choice of the harvester geometries is motivated by the existing literature. The detailed overview of the rod-type and cantilever-beam-type energy harvesting devices developed in the previous literature is presented in Section 2.4. This research utilizes galfenol as an active material for the development of the prototype energy harvesters. The section discusses the experimental setups presented in Publications I–IV in chronological order.

3.1.1 Material characterization

Publication I present the experimental setup for the material characterization developed by Zucca at Istituto Nazionale di Ricerca Metrologica (INRiM) in [90]. The material characterization was performed during a research exchange period in collaboration with INRiM. The material characterization is needed to determine the influence of stress over the magnetization of the magnetostrictive material. The schematic diagram of the experimental setup developed for the

material characterization is shown in Figure 3.1. The setup consists of a galfenol rod, pick-up coil, magnetizing coils, a magnetic core, a Hall probe, and a fatigue testing machine. A galfenol rod of stoichiometry $Fe_{81.6}Ga_{18.4}$ produced by Etrema Products is utilized as the sample material to be characterized. The galfenol rod is based on a polycrystalline material grown as the <001> axis aligned along the length of the rod. The galfenol rod has a length of 60 mm and a diameter of 12 mm. The magnetization is provided by a set of coils and a U-shaped magnetic core. The magnetic core is connected to the galfenol rod with the help of two solid caps made from pure iron placed at both ends of the rod, as shown in Figure 3.1. The overall dimensions of the magnetic core are 120 mm x 68 mm x 15 mm. The core is prepared from non-oriented silicon-iron sheets of 0.2 mm thickness. The magnetizing coils are connected in series and consist of 600 turns. The power amplifier (E-480 HVPZT Amplifier) can deliver a maximum current of 6 A through magnetizing coils. A pick-up coil of 40 turns made from 0.2 mm thick enameled copper wire is wound around the active material.

A high-performance fatigue testing machine (Instron ElectroPlus E10000) is utilized to provide mechanical loadings. The test machine can deliver a linear static force of ± 7 kN and a dynamic force of ± 10 kN by using high pressure pneumatic mechanical grips. The testing machine has the capability to provide mechanical loadings with a maximum frequency of 100 Hz. For material characterization, the galfenol rod is first subjected to a static compressive stress σ (preload) applied from the top in the axial direction indicated by arrows in

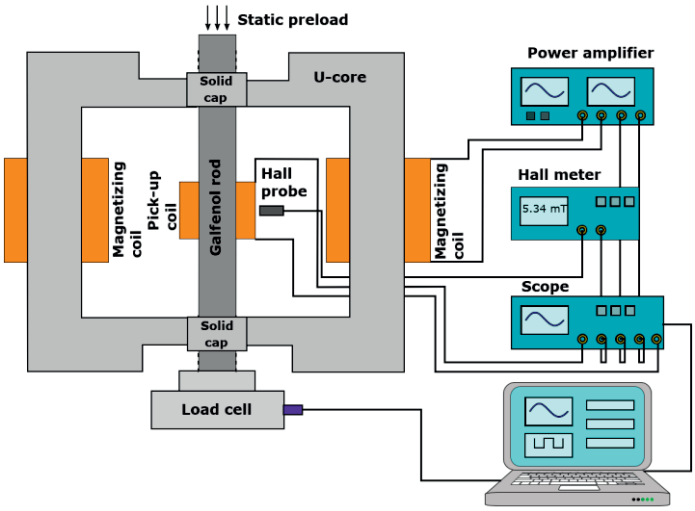

Figure 3.1 Schematic diagram for the characterization setup [Publication I].

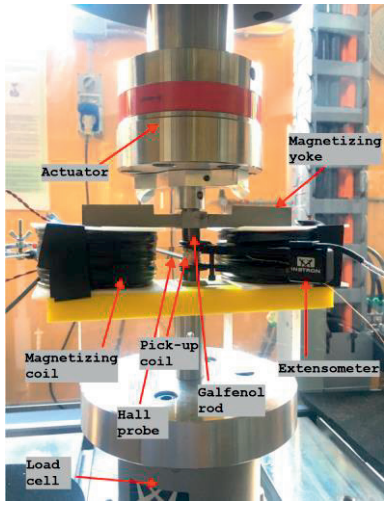

Figure 3.2 The actual setup for the material characterization [Publication I].

Figure 3.1. The rod is then magnetized by applying a sinusoidal AC voltage of 200 mHz through a power amplifier and a signal generator. This causes an induced voltage into the pick-up coil wound around the galfenol rod as a result of Faraday's law. The magnetic field strength $H(t)$ is measured using a Hall probe (LakeShore transverse probe 400 series) placed perpendicularly in contact with the external surface of the rod, located at the center of the rod in the longitudinal direction as shown in Figure 3.2. The magnetic flux density $B(t)$ is obtained by integrating the induced voltage from the pick-up coil as

$$B(t) = -\frac{1}{NA}\int_0^t V_{\text{ind}}(t)dt \tag{3.1}$$

where N denotes the number of turns in the pick-up coil, A is the cross-section area of the galfenol rod and $V_{\text{ind}}(t)$ is the induced voltage. The actual setup for the material characterization is presented in Figure 3.2.

The strain $\varepsilon(t)$ is measured using an extensometer clamped at the middle of the sample. The hysteresis loop of the measured magnetization curve (B–H) obtained at zero preload condition is presented in Figure 3.3, which shows that galfenol has negligible hysteresis loss. Therefore, single-valued curves can be effectively utilized by taking the average of the hysteresis loop. Moreover, the material tends to saturate around 20 kA/m, which is quite small compared to Terfenol-D saturating around the magnetic field of 160 kA/m reported in [2]–[5], [91], [92]. A set of single-valued measured magnetization and magnetostriction (ε–H)

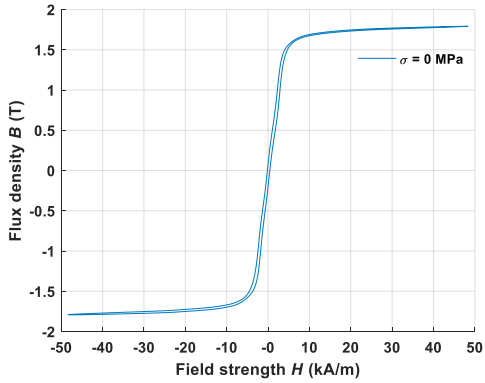

Figure 3.3 Measured magnetization curve plotted as hysteresis loop at zero preload condition.

curves obtained at different compressive preload values ranging from 0 to 80 MPa with a step of 10 MPa are presented in Figure 3.4 and Figure 3.5, respectively.

The results from Figure 3.4 show that the permeability of the material decreases with the increase in the preload value from 0 to 80 MPa, indicated by an arrow. In addition, the magnetostriction of the material also varies with change in the preload values, as can be seen from Figure 3.5. The magnetostriction curves show nonlinear behavior with respect to the applied magnetic field and require a stronger magnetic field to reorient the magnetic moments at larger preload values. Thus, a higher magnetic field is required to obtain the same elongation in the material at larger preload values. The measured saturation magnetostriction under zero preload condition is 250 ppm; this increases to 276 ppm at 10 MPa and reaches a maximum value of 289.8 ppm at 20 MPa. This shows that there is indeed an optimal preload value that needs to be tuned in order to maximize the performance of the energy harvester device.

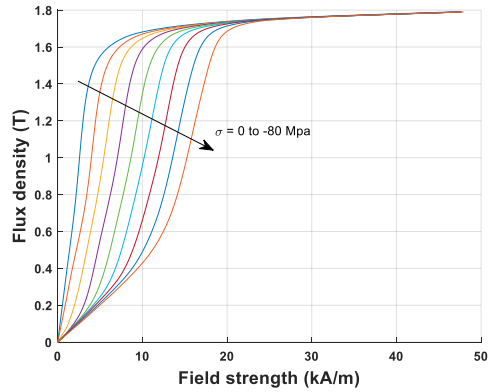

Figure 3.4 Single-valued measured magnetization curves (*B–H*) obtained at static compressive preload values from 0 to 80 MPa.

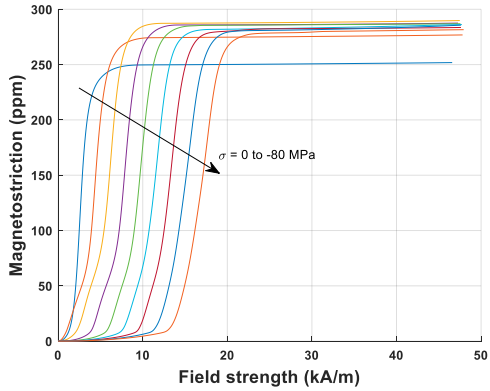

Figure 3.5 Single-valued measured magnetostriction curves (*ε*–*H*) obtained at static compressive preload values from 0 to 80 MPa.

3.1.2 Rod-type energy harvester

Publication I utilize a galfenol-based rod-type energy harvester device that was developed by Zucca and Palumbo in [42] and constructed at Istituto Nazionale di Ricerca Metrologica. The experimental work and measurements were performed during a research exchange period in collaboration with INRiM. The schematic diagram and working principle of the energy harvesting setup is shown in Figure 3.6. The energy harvester consists of a galfenol rod, two permanent magnets, and a pick-up coil. The galfenol rod, with a length of 60 mm and a diameter of 12 mm is first machined from the middle part to accommodate the pick-up coil. The rod diameter is reduced from 12 mm to 6 mm after machining the sample for the

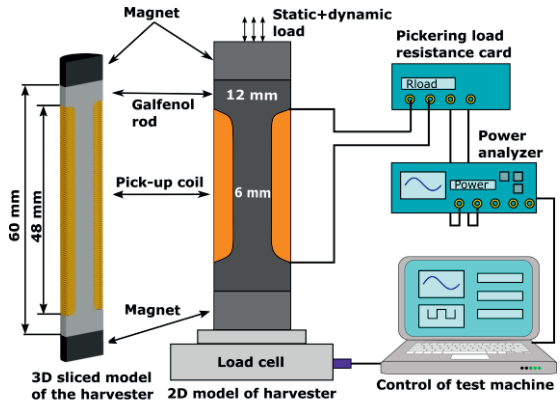

Figure 3.6 Schematic diagram and working principle of the rod-type galfenol-based prototype energy harvester setup [Publication I].

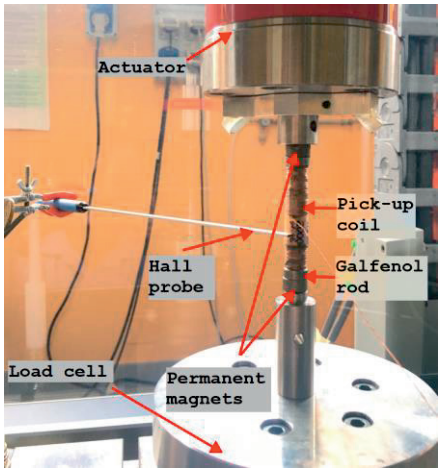

Figure 3.7 The actual setup of the rod-type galfenol-based prototype energy harvester [Publication I].

length of 48 mm, as indicated in Figure 3.6. This allowed us to utilize the same stress applied by the test machine to analyze the behavior of the material over a wide range of mechanical bias amplitudes.

A constant magnetic bias is provided using neodymium-iron-boron (NdFeB) permanent magnets placed at both ends of the galfenol rod. The magnets have a measured remanence flux density of B_r = 1.2 T and a corresponding coercive field of H_c = 955 kA/m with physical dimensions of 6 mm in thickness and 12 mm in diameter. A pick-up coil of 2000 turns made from 0.2 mm thick enameled copper wire is wound around the machined sample length of 48 mm, as shown in Figure 3.6. The pick-up coil has a measured wire resistance of 32.6 Ω. The total sinusoidal mechanical stress, $\sigma_{tot}(t) = \sigma + \Delta\sigma \sin(2\pi ft)$, consisting of static mechanical preload σ and dynamic load $\Delta\sigma$ are applied in the axial direction using the actuator of the fatigue testing machine through permanent magnets. The NdFeB magnet has a multilayer coating of phosphate and polytetrafluoroethylene (PTFE) which provides prolonged protection against oxidation corrosion and abrasion resistance [93]–[95]. The actual setup of the rod-type galfenol-based energy harvester is shown in Figure 3.7.

For the energy harvesting setup presented in Figure 3.7, the magnetized galfenol rod is first subjected to a static compressive preload, followed by a sinusoidal dynamic load of 100 Hz frequency. The excitation frequency is kept constant throughout the experiments. A voltage is induced into the pick-up coil as a result of Faraday's law and the Villari effect. The mechanical load is measured and controlled by a load cell used in a feedback loop. Moreover, the

applied load is increased gradually to avoid excessive loading during the transient period. The load cell can measure the force with an expanded uncertainty of ≤ 0.5 percent. The induced voltage is measured using a precision power analyzer (Yokogawa WT3000). The pick-up coil is connected to a Pickering programmable precision resistor card (PXI 40-297-002), which serves as a variable load resistance (R_{load}). The load resistance is varied to determine the optimal value yielding maximum output power. The prototype energy harvester device is tested under various amplitudes of σ values ranging from 40 MPa to 80 MPa, $\Delta\sigma$ values ranging from 6 MPa to 8 MPa, and R_{load} values ranging from 5 to 250 Ω to determine the influence of mechanical bias and load resistance upon harvested output power.

3.1.3 Rod-type harvester with magnetic core

A modified rod-type harvester device developed in [42] is utilized in Publication II, which consists of a magnetic core and additional permanent magnet. The schematic diagram of the experimental setup is shown in Figure 3.8. The magnetic core provides a closed path for the magnetic flux to enter into the galfenol rod. The motivation of Publication II was to include the effect of change in magnetic bias upon the performance of the energy harvester. The magnetic core is made from non-oriented silicon-iron sheets with a thickness of 0.2 mm. The leg of the U-shaped magnetic core is cut from the middle to accommodate the permanent magnets such that the overall length of the magnetic circuit remains unchanged. The resulting L-shaped magnetic cores are connected to the galfenol

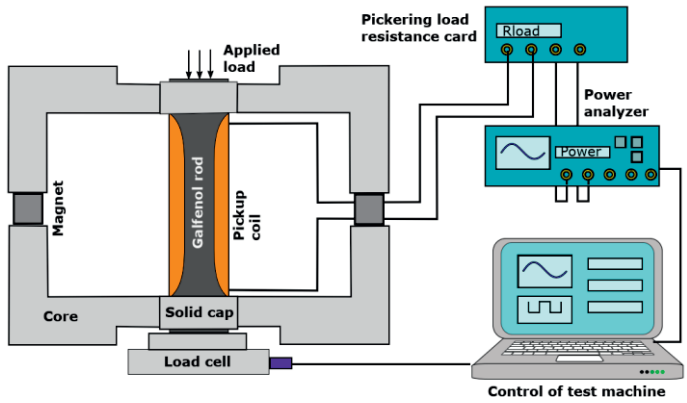

Figure 3.8 Schematic diagram of the rod-type prototype energy harvester fitted with magnetic core [Publication II].

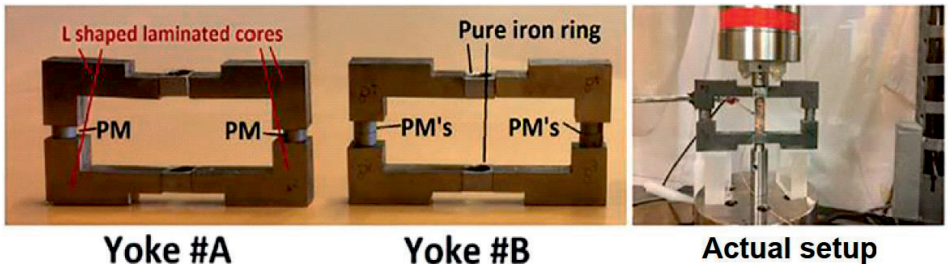

Figure 3.9 The actual setup of the rod-type prototype harvester with magnetic core (right) having two magnets (Yoke#A) and four magnets (Yoke#B) on both sides [42].

rod with the help of solid caps made from pure iron placed at both ends of the galfenol rod.

Unlike the harvester setup shown in Figure 3.6, the mechanical load is directly applied to the galfenol rod shown in Figure 3.8. This allows direct actuation of the galfenol rod and protects the magnets from wearing under continuous and intense mechanical stresses. The right side of Figure 3.9 shows the actual setup of the rod-type energy harvester fitted with the magnetic closure circuit. Two different cases labelled as Yoke#A and Yoke#B are studied to analyze the influence of change in magnetic bias upon the energy harvester performance shown in Figure 3.9 (left). The magnetic bias in Yoke#A case is provided by two permanent magnets placed between the columns of the L-shaped magnetic cores, whereas the Yoke#B case utilizes four permanent magnets placed as a pair at each column. The modified harvester geometry is tested under varying amplitudes of the preload ranging from 20 MPa to 80 MPa at a fixed dynamic load of 8 MPa for both Yoke#A and Yoke#B. The load resistance is kept constant at 160 Ω. The experimental results are analyzed to determine the influence of mechanical load and magnetic bias over the measured output power.

3.1.4 Cantilever-beam-type energy harvester

A cantilever-beam-type prototype energy harvester device is developed and tested in Publication IV. The motivation behind Publication IV was to validate the thermodynamic magneto-mechanical modeling approach to analyze different geometries of the prototype energy harvesters. To do this, a cantilever beam-type prototype energy harvester is constructed at the laboratory of Tampere University. The schematic diagram showing the working principle of the cantilever-beam-type energy harvester device is shown in Figure 3.10. The device design of the

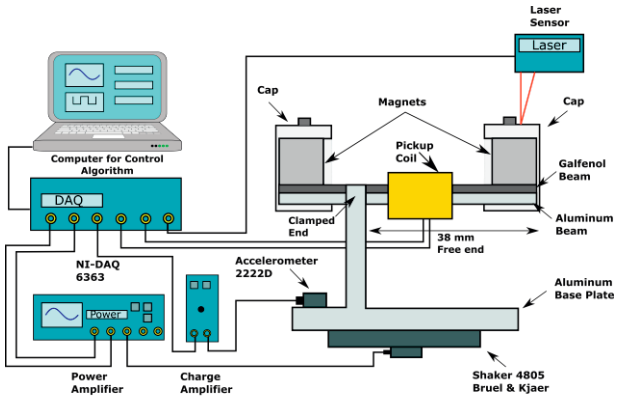

Figure 3.10 Schematic diagram and working principle of a cantilever-beam-type prototype energy harvester [Publication IV].

cantilever harvester is obtained from the literature presented in [49] and [86]. The cantilever beam consists of a unimorph structure and utilizes a galfenol beam of length 50 mm and width 6 mm, with a thickness of 0.78 mm as an active layer. The galfenol beam is attached to an aluminum beam with a length of 50 mm, width of 6 mm, and thickness of 1.28 mm. The aluminum beam is the passive layer and provides mechanical support to the galfenol beam. Both beams are glued by evenly applying a thin layer of Loctite superglue. The cantilever beam was kept in a bench vice for 8 hours to cure the glue properly. Care is taken to avoid any misalignment that could affect the bending modes of the cantilever beam. The cantilever beam is magnetized using two NdFeB magnets with dimensions of $10 \times 10 \times 10$ mm^3 attached at both ends of the beam. The magnet has a remanence flux density of B_r = 1.18 T measured using a Hall probe with Gaussmeter (DX-103). The magnets are fixed in place with the help of screws and caps made from PETG material shown in Figure 3.10. The mechanical vibrations are provided utilizing a Brüel & Kjær shaker device that uses a permanent magnet motor (base model type 4805 with tabletop type 4813). The maximum displacement amplitude of the shaker base plate is 13 mm peak-to-peak with the excitation frequency up to 3 kHz. The input signal to the shaker is supplied a linear power amplifier from Venable Instruments.

A customized aluminum base plate is made to clamp the cantilever beam with the shaker base to provide mechanical excitations. The beam is clamped such that the active free length of the beam is measured to be 38 mm from the fixed end indicated in Figure 3.10. The height of the clamping structure is chosen to avoid any interference from the magnetic field of the permanent magnet motor of the

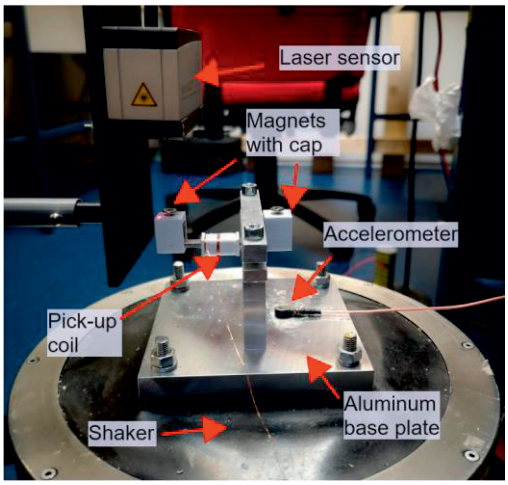

Figure 3.11 The actual setup of the cantilever-beam-type prototype energy harvester [Publication IV].

shaker. The overall mass of the cantilever beam is 2.14 grams, measured a using precision scale with resolution of 0.01 grams. The total mass of magnet, cap and screw at the free end is 7.57 grams, which also acts as a tip mass for the cantilever beam. A pick-up coil of 1000 turns made from 0.1 mm thick enameled copper wire is placed at the free end of the beam. The amplitude and frequency of the mechanical vibrations are measured using a piezoelectric accelerometer (Endevco model 2222D) mounted on the aluminum base plate. The tip displacement of the free end is measured using an optical laser displacement sensor from Micro Epsilon (model optoNTDC ILD1900-25). The sensor can record the data with a sampling rate of 10 kHz and has the measuring range of 25 mm with a linearity range within ± 5 µm. The actual experimental setup of the prototype cantilever-beam-type energy harvester is shown in Figure 3.11.

For the energy harvesting setup, the cantilever beam is first subject to the sinusoidal mechanical vibrations. The application of mechanical vibrations produces time-varying strain/stress in the cantilever beam, which causes an induced voltage into the pick-up coil as a result of Faraday's law. The amplitude of the mechanical vibration acceleration is varied from 1g to 2g with a step of 0.5g, where g = 9.81 m/s^2 is the gravitational acceleration. For each value of the acceleration amplitude, the resonant frequency of the cantilever beam is deduced by sweeping the vibration frequency and measuring the tip displacement yielding maximum displacement value. The amplitude of vibrations is controlled by measuring the output signal from the accelerometer in a feedback loop. The control algorithm is implemented using a MATLAB-controlled National

Instruments data acquisition card NI-6363, from which a sinusoidal input voltage signal is generated and supplied to the shaker via the power amplifier. The amplitude of the voltage signal is varied in an iterative way until it reaches the desired acceleration value, where it is kept constant for six seconds to obtain the measurements. The experimental setup is repeated for each acceleration amplitude to measure the open circuit voltage of the pick-up coil and the resonant frequency of the beam. The measured results are then analyzed to determine the effect of magnetic and mechanical bias over resonant frequency of the harvester.

The literature presented in [38]–[42] suggests that the deviation among measurement results and their repeatability is crucial for determining the measurement error. This information is needed to determine the contribution of measurement error while analyzing the deviations among measured and simulated results. When comparing measured and simulated results, the variations and repeatability of the experiments should be kept in mind. Therefore, the experiments from the energy harvesting setup for each configuration of the prototype energy harvester device discussed in Section 3.1 are repeated at least three times to determine the deviation. It was observed that the deviations among measurement results may occur partly due to the measuring instruments (measurement resolution and linearity range), slight changes in the experimental setup (misalignments, small air gap changes in magnetic circuit, displacement of magnets due to vibration or reduction in adhesive strength due to fatigue), or human error. Therefore, special care was taken while repeating the experiments to minimize the effects of changes in the experimental setup. The measurements were performed after the warm-up time of all measuring devices had elapsed to minimize the measurement errors.

3.2 Constitutive models

The literature review suggests that coupled magneto-mechanical modeling tools are needed in order to design and optimize the magnetostrictive energy harvesting devices. This thesis presents two different modeling approaches for analyzing the galfenol-based magnetostrictive energy harvesters. The first approach utilizes a thermodynamic magneto-mechanical model [68], [69] based on an analytical expression of the Helmholtz free energy density function, whereas the second approach utilizes an equivalent stress model [73], [74] to analyze the energy harvester device. Furthermore, 2D and 3D FE models are presented to investigate

the coupled magneto-mechanical effects in the magnetostrictive material. The developed models are validated against the measured results obtained from the rod-type and cantilever-beam-type galfenol-based energy harvester prototype devices described in the previous section.

3.2.1 Thermodynamic magneto-mechanical model

An energy-based magneto-mechanical constitutive model is utilized in Publications I, II, and IV to analyze the galfenol-based magnetostrictive energy harvesters. Initially, a rod-type prototype harvester device is modeled utilizing a thermodynamic approach presented in [68], [69] based on deriving a free energy density expression. The experimental setup and working principle of the rod-type energy harvester is discussed in Section 3.1.2. Models presented in [70]–[72] utilize a similar energy-based modeling approach, with a slightly modified energy density function for coupled magneto-mechanical analysis of the core laminations of the iron sheets used in electrical machines. The magneto-mechanical constitutive equations are derived based on Helmholtz free energy density $\psi(\boldsymbol{B}, \boldsymbol{\varepsilon})$ as a function of the magnetic flux density vector $\boldsymbol{B}$ and strain tensor $\boldsymbol{\varepsilon}$ chosen as the independent state variables. This choice of state variables is convenient, as it simplifies the implementation of FE models based on magnetic vector potential and mechanical displacement, since time-consuming inversion of the constitutive law is not required. The constitutive model describes the magneto-elastic interactions in the galfenol material. The total strain consists of both the strain caused by magnetostriction $\boldsymbol{\lambda}$ and mechanical strain $\boldsymbol{S}^{-1}\boldsymbol{\sigma}$, written as

$$\boldsymbol{\varepsilon} = \boldsymbol{S}^{-1}\boldsymbol{\sigma} + \boldsymbol{\lambda} \tag{3.2}$$

where $\boldsymbol{S}$ is the mechanical stiffness tensor and $\boldsymbol{\sigma}$ is the stress. Assuming galfenol is an isotopic material, free energy density function $\psi(\boldsymbol{B}, \boldsymbol{\varepsilon})$ can be written in terms of six scalar invariants

$$\begin{gathered} I_1 = \operatorname{tr} \boldsymbol{\varepsilon}\,,\ I_2 = \operatorname{tr} \boldsymbol{\varepsilon}^2,\ I_3 = \operatorname{tr} \boldsymbol{\varepsilon}^3, \\ I_4 = \frac{\boldsymbol{B}\cdot\boldsymbol{B}}{B_{\mathrm{ref}}^2},\ I_5 = \frac{\boldsymbol{B}\cdot\boldsymbol{\varepsilon}\boldsymbol{B}}{B_{\mathrm{ref}}^2},\ I_6 = \frac{\boldsymbol{B}\cdot\boldsymbol{\varepsilon}^2\boldsymbol{B}}{B_{\mathrm{ref}}^2} \end{gathered} \tag{3.3}$$

where tr represents the trace of a tensor. Invariants I_1, I_2 and I_3 describe pure mechanical behavior, I_4 describes pure magnetic behavior whereas I_5 and I_6 describe magneto-elastic behavior of the material. Invariant I_3 is not used considering linear elastic behavior of the material. Since the hydrostatic part does not have an effect on the magnetization properties [70], the deviatoric part of strain $\boldsymbol{e}$ is used in invariant I_5 and I_6 obtained as

$$\boldsymbol{e} = \boldsymbol{\varepsilon} - \frac{1}{3}(\text{tr}\ \boldsymbol{\varepsilon})\boldsymbol{I} \tag{3.4}$$

where $\boldsymbol{I}$ represents the second-order identity tensor. B_{ref} = 1 T in (3.3) is used for the purpose of scaling and to make the invariants dimensionless. The analytical expression for the Helmholtz free energy density function describing the magneto-mechanical interactions in the galfenol material is then written as

$$\psi = \frac{1}{2}\lambda I_1^2 + \mu I_2 + \sum_{i=1}^{n_\alpha} \alpha_i I_4^i + \sum_{i=1}^{n_\beta} \beta_i I_5^i + \sum_{i=1}^{n_\gamma} \gamma_i I_6^i \,. \tag{3.5}$$

The chosen energy density function resembles the one in [69], [72], with slight modifications. The polynomial coefficients α_i β_i and γ_i are the model parameters and λ and μ are the Lamé parameters obtained from Young's modulus E and Poisson's ratio v as

$$\lambda = \frac{Ev}{(1+v)(1-2v)} \tag{3.6}$$

$$\mu = \frac{E}{2(1+v)} \,. \tag{3.7}$$

The constitutive equations for the magnetic field strength $\boldsymbol{H}$ and Cauchy stress tensor $\boldsymbol{\sigma}$ are then obtained by partial differentiation of ψ with respect to the state variables $\boldsymbol{B}$ and $\boldsymbol{\varepsilon}$ as

$$\boldsymbol{H}(\boldsymbol{B}, \boldsymbol{\varepsilon}) = \left(\frac{\partial \psi}{\partial \boldsymbol{B}} \right)^{\text{T}} \tag{3.8}$$

$$\boldsymbol{\sigma}(\boldsymbol{B}, \boldsymbol{\varepsilon}) = \frac{\partial \psi}{\partial \boldsymbol{\varepsilon}} \tag{3.9}$$

where T denotes the transpose. The polynomial coefficients α_i β_i and γ_i are determined by fitting the function $\boldsymbol{H}(\boldsymbol{B}, \boldsymbol{\varepsilon})$ obtained from (3.5), (3.8), and (3.9) against the single-valued measured magnetization curves $H(B, \sigma)$ shown in Figure 3.4 obtained from material characterization presented in Section 3.1.1. During the fitting, the strain tensor $\boldsymbol{\varepsilon}$ is iterated with the Newton Raphson method until the desired uniaxial stress is obtained as

$$\boldsymbol{\varepsilon} = \begin{bmatrix} \varepsilon_{xx} \\ \varepsilon_{yy} \\ \varepsilon_{xy} \\ \varepsilon_{zz} \end{bmatrix}, \boldsymbol{B} = \begin{bmatrix} B_x \\ 0 \\ 0 \end{bmatrix}, \boldsymbol{\sigma}(\boldsymbol{B}, \boldsymbol{\varepsilon}) = \begin{bmatrix} \sigma_{xx} \\ \sigma_{yy} \\ \sigma_{xy} \\ \sigma_{zz} \end{bmatrix}$$

$$\boldsymbol{r}(\boldsymbol{\varepsilon}^i) = \boldsymbol{\sigma}(\boldsymbol{B}, \boldsymbol{\varepsilon}) - \begin{bmatrix} \sigma_{xx} \\ 0 \\ 0 \\ 0 \end{bmatrix} = 0 \tag{3.10}$$

$$\boldsymbol{J}(\boldsymbol{\varepsilon}^i) = \left. \frac{d\boldsymbol{r}}{d\boldsymbol{\varepsilon}} \right|_{\boldsymbol{\varepsilon}=\boldsymbol{\varepsilon}^i}$$

$$\boldsymbol{\varepsilon}^{i+1} = \boldsymbol{\varepsilon}^i - \boldsymbol{J}(\boldsymbol{\varepsilon}^i)^{-1} \boldsymbol{r}(\boldsymbol{\varepsilon}^i)$$

where B_x and σ_{xx} are the measured uniaxial flux density and stress given initially as an input, $\boldsymbol{r}$ is the residual vector that needs to be minimized, and $\boldsymbol{J}$ represents the Jacobian matrix.

3.2.2 Equivalent stress model

In Publication III, the equivalent stress model presented in [73], [74] is utilized for the first time to analyze a magnetostrictive energy harvesting device. The model has previously been utilized to study the magnetic hysteresis losses in thin iron-silicon sheets used in the rotors of variable frequency generators [75]. The model was able to successfully describe the effect of stress on the magnetic behavior of the material caused by metal-forming process. In energy harvesting applications, different combinations and orientations of magnetic fields and mechanical stresses can occur making the problem to be multiaxial in nature. Therefore, the concept of equivalent stress can be utilized to study the magneto-mechanical behavior of magnetostrictive material under different magnetic and mechanical

bias cases. In this study, the model is used to analyze the rod-type galfenol-based prototype energy harvester device shown in Figure 3.8. Unlike multiaxial magneto-mechanical models, the equivalent stress model provides a simplified approach to predict the permeability of the material based on uniaxial measurements. The equivalent stress model can transform any arbitrary stress tensor $\boldsymbol{\sigma}$ into an equivalent uniaxial stress σ_{eq} oriented parallel to the applied flux density. The resulting uniaxial stress would change the magnetic behavior of the material in a similar way as the multiaxial stress. This approach has an advantage over models that are restricted to describing the effect of stress on the magnetic behavior of the materials under uniaxial mechanical loadings. The complete derivation of the equivalent stress model is presented in [73]. Briefly, the equivalent stress model is based on defining an equivalence in the magnetoelastic energy W_{σ} over a volume V by

$$W_{\sigma} = \frac{1}{V}\int_{V} -\boldsymbol{\sigma} : \boldsymbol{\varepsilon} dV \tag{3.11}$$

where $\boldsymbol{\sigma}$ and $\boldsymbol{\varepsilon}$ are the stress and magnetostriction strain tensors, respectively. Three assumptions are made. First the stress is considered uniform over the volume of the material; second, the material is considered to be isotropic; third, the magnetostriction is assumed to be isovolumetric. The components of macroscopic stress tensor $\boldsymbol{\sigma}$ and strain tensor $\boldsymbol{\varepsilon}$ are written as

$$\boldsymbol{\sigma} = \begin{bmatrix} \sigma_{11} & \sigma_{12} & \sigma_{13} \\ \sigma_{21} & \sigma_{22} & \sigma_{23} \\ \sigma_{31} & \sigma_{32} & \sigma_{33} \end{bmatrix} \text{ and } \boldsymbol{\varepsilon} = \lambda \begin{bmatrix} 1 & 0 & 0 \\ 0 & -\frac{1}{2} & 0 \\ 0 & 0 & -\frac{1}{2} \end{bmatrix} \tag{3.12}$$

where λ is the magnetostriction strain measured in 11 direction aligned with the flux density. The magnetoelastic energy becomes

$$W_{\sigma} = -\lambda \left[\frac{3}{2}\sigma_{11} - \frac{1}{2}\text{tr}(\boldsymbol{\sigma}) \right]. \tag{3.13}$$

In order to obtain the magnetoelastic energy independent of the chosen coordinate system, the stress component in the direction of the magnetic flux density vector

$\boldsymbol{B} = B\boldsymbol{b}$ is written as $\sigma_{11} = \boldsymbol{b}^{\mathrm{T}}\boldsymbol{\sigma}\boldsymbol{b}$, where B is the magnitude of the flux density and $\boldsymbol{b}$ is the direction vector. The magnetoelastic energy can be rewritten as

$$W_{\sigma} = -\lambda\left(\frac{3}{2}\boldsymbol{b}^{\mathrm{T}}\boldsymbol{\sigma}\boldsymbol{b} - \frac{1}{2}\mathrm{tr}(\boldsymbol{\sigma})\right). \tag{3.14}$$

Considering the case of a uniaxial stress acting parallel to the magnetic flux density applied in 11 direction the magnetoelastic energy becomes $W_{\sigma} = -\lambda\sigma_{11}$. Assuming the same magnetoelastic energy leads to same magnetic behavior and λ does not depends on $\boldsymbol{\sigma}$. The equivalent stress σ_{eq} can be obtained as

$$\sigma_{\mathrm{eq}} = \frac{3}{2}\boldsymbol{b}^{\mathrm{T}}\boldsymbol{s}\boldsymbol{b} \tag{3.15}$$

where $\boldsymbol{s} = \boldsymbol{\sigma} - (1/3)\mathrm{tr}(\boldsymbol{\sigma})\boldsymbol{I}$ is the deviatoric part of stress tensor $\boldsymbol{\sigma}$. The permeability data $\mu(B, \sigma)$ is first obtained from the uniaxial measurements during the characterization of the galfenol material discussed in Section 3.1.1. The equivalent stress model then utilizes the permeability data to predict the correct permeability for a combination of an arbitrary stress tensor $\boldsymbol{\sigma}$ and flux density vector $\boldsymbol{B}$ using interpolation. The equivalent stress model is implemented in COMSOL for 3D FE analysis, which will be discussed in Section 3.3. Publication III also provides a comparison among the thermodynamic model and equivalent stress model by comparing the simulated results for the rod-type prototype energy harvester fitted with a magnetic core.

3.3 Finite element models

The constitutive equations presented in Section 3.2.1 are implemented in 2D and 3D FE models to analyze the magneto-mechanical behavior of the actuator material. The proposed models are validated against the measured results obtained from the rod-type and cantilever-beam-type prototype energy harvester devices under changing operating conditions and design parameters.

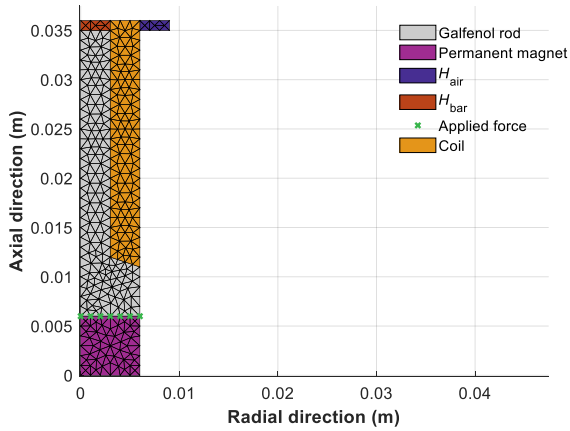

Figure 3.12 The geometry and FE mesh utilized in the rod-type galfenol-based prototype harvester device [Publication I].

3.3.1 2D axisymmetric FE model

The thermodynamic magneto-mechanical modeling approach is first validated on the rod-type prototype energy harvester device discussed in Section 3.1.2. The analytical expressions of the constitutive equations developed in Section 3.2.1 are implemented in a 2D axisymmetric FE model. The geometry and FE mesh, utilized in an 2D axisymmetric FE model, is presented in Figure 3.12. The air domain is not shown in Figure 3.12. However, a sufficiently large air domain was chosen to maintain a balance between the solution accuracy and computation efficiency. The dimensions of the air domain are 120 mm and 216 mm in radial and axial directions, respectively. The magnetic field computed in the air and inside the galfenol sample is marked by the regions H_{air} and H_{bar}. The green markers shown in Figure 3.12 represent the boundary of the galfenol rod where the axial mechanical load is applied. In the galfenol region, the 2D axisymmetric magneto-mechanical FE model is based on solving the mechanical balance equations, together with the combination of Ampere's and Faraday's law

$$\nabla \cdot \boldsymbol{\sigma}\left(\boldsymbol{B}, \boldsymbol{\varepsilon}\right) = 0 \tag{3.16}$$

$$\nabla \times \boldsymbol{H}\left(\boldsymbol{B}, \boldsymbol{\varepsilon}\right) + \kappa \frac{\partial \boldsymbol{A}}{\partial t} = 0 \tag{3.17}$$

where κ is the electrical conductivity. The magnetic flux density vector $\boldsymbol{B}$ and strain tensor $\boldsymbol{\varepsilon}$ are expressed as

$$\boldsymbol{B} = \nabla \times \boldsymbol{A} \tag{3.18}$$

$$\boldsymbol{\varepsilon} = \frac{1}{2}\left(\nabla \boldsymbol{u} + (\nabla \boldsymbol{u})^{\mathrm{T}}\right) \tag{3.19}$$

where $\boldsymbol{A} = A\boldsymbol{e}_\theta$ is the circumferential magnetic vector potential and $\boldsymbol{u} = u_\mathrm{r}\boldsymbol{e}_\mathrm{r} + u_\mathrm{z}\boldsymbol{e}_\mathrm{z}$ is the displacement vector, which are used as field variables in the symmetry plane. Equations (3.16) and (3.17) are coupled through the constitutive law (3.5), (3.8), and (3.9). In other regions, only the electromagnetic problem is solved by

$$\nabla \times \left(\nu_0 \nabla \times \boldsymbol{A}\right) + \kappa \frac{\partial \boldsymbol{A}}{\partial t} = \boldsymbol{J}_\mathrm{s} + \nabla \times \boldsymbol{H}_\mathrm{c} \tag{3.20}$$

where ν_0 is constant reluctivity of free space and $\boldsymbol{J}_\mathrm{s} = (Ni_\mathrm{coil}/S_\mathrm{coil})\boldsymbol{e}_\theta$ is the circumferential source current density, which is nonzero only in the pick-up coil. N, S_coil and i_coil denotes the number of turns in the coil, coil cross-section area and coil current, respectively. $\boldsymbol{H}_\mathrm{c} = H_\mathrm{c}\boldsymbol{e}_\mathrm{z}$ is the axially oriented coercive field of the permanent magnet, given as a parameter that is nonzero only in the magnet.

The field problem and variables A, u_r and u_z are discretized using a standard Galerkin FE discretization with nodal shape function $\boldsymbol{N} = [N_1, N_2, \ldots]$. The coil current i_coil of the pick-up coil is set as an additional variable that is solved from the voltage equation. The complete system of equations is

$$\begin{aligned}
&\int_\Omega r\left(-\left(\frac{\partial \boldsymbol{N}^{\mathrm{T}}}{\partial r} + \frac{\boldsymbol{N}^{\mathrm{T}}}{r}\right)H_\mathrm{z} + \frac{\partial \boldsymbol{N}^{\mathrm{T}}}{\partial z}H_\mathrm{r}\right)d\Omega + \left(\int_\Omega r\kappa \boldsymbol{N}^{\mathrm{T}}\boldsymbol{N}d\Omega\right)\frac{d\boldsymbol{a}}{dt} - \boldsymbol{D}i_\mathrm{coil} = 0 \\
&\int_\Omega r\left(\frac{\partial \boldsymbol{N}^{\mathrm{T}}}{\partial r}\sigma_\mathrm{rr} + \frac{\partial \boldsymbol{N}^{\mathrm{T}}}{\partial z}\sigma_\mathrm{zz}\right)d\Omega + \int_\Gamma r\boldsymbol{N}^{\mathrm{T}}\left[\sigma_\mathrm{rr}\ \ \sigma_\mathrm{zz}\right]\boldsymbol{n}d\Gamma = 0 \\
&\int_\Omega r\left(\frac{\partial \boldsymbol{N}^{\mathrm{T}}}{\partial r}\sigma_\mathrm{rr} + \frac{\boldsymbol{N}^{\mathrm{T}}}{r}\sigma_{\theta\theta} + \frac{\partial \boldsymbol{N}^{\mathrm{T}}}{\partial z}\sigma_\mathrm{rz}\right)d\Omega + \int_\Gamma r\boldsymbol{N}^{\mathrm{T}}\left[\sigma_\mathrm{rr}\ \ \sigma_\mathrm{rz}\right]\boldsymbol{n}d\Gamma = 0 \\
&\boldsymbol{C}\frac{d\boldsymbol{a}}{dt} + (R_\mathrm{coil} + R_\mathrm{load})i_\mathrm{coil} = 0
\end{aligned} \tag{3.21}$$

where vector $\boldsymbol{a}$ contains the nodal values of the vector potential $A = \boldsymbol{N}\boldsymbol{a}$, and r denotes the radial coordinate. R_coil is the resistance of the pick-up coil and R_load is

the load resistance. In addition, the components of stress and magnetic field strength in the radial (r), axial (z) and circumferential (θ) directions are σ_{rr}, σ_{zz}, $\sigma_{\theta\theta}$, H_r, and H_z, respectively. The calculation domain in the axisymmetric plane is denoted by Ω, Γ represents the boundary lines inside Ω where the mechanical load is applied, and $\boldsymbol{n}$ is outer normal vector of Γ. As boundary conditions, the radial displacement u_r is set to zero at the longitudinal middle axis of the galfenol rod, whereas the axial displacement u_z is fixed to zero in the middle cross-section area of the rod. The top boundary has a Neumann boundary condition, and the circumferential magnetic vector potential $\boldsymbol{A}$ is fixed to zero at the outer boundaries and the symmetry axis. The flux linkage and source current density matrices $\boldsymbol{C}$ and $\boldsymbol{D}$ of the winding are given by

$$\boldsymbol{C} = \frac{2\pi N}{S_{\text{coil}}} \int_{\Omega_{\text{coil}}} r\boldsymbol{N} d\Omega \tag{3.22}$$

$$\boldsymbol{D} = \frac{N}{S_{\text{coil}}} \int_{\Omega_{\text{coil}}} r\boldsymbol{N}^{\mathrm{T}} d\Omega \,. \tag{3.23}$$

The discretization of the time derivatives is done using Backward-Euler method as

$$\frac{d\boldsymbol{a}}{dt} = \frac{\boldsymbol{a} - \boldsymbol{a}_{\text{previous}}}{\Delta t}. \tag{3.24}$$

To provide a reasonable accuracy of the solution, the time step Δt is chosen to be 100 µs. The resulting discretized system in (3.21) is solved using the Newton-Raphson method.

3.3.2 3D FE model for the rod-type harvester

In Publication II, the thermodynamic magneto-mechanical model presented in Section 3.2.1 is implemented in COMSOL Multiphysics for 3D FE analysis of the rod-type energy harvester discussed in Section 3.1.2. The idea is to test the capability of commercial software COMSOL to implement the custom constitutive model. This provides the advantage of performing parametric sweep operations and modifying the geometry conveniently for performance

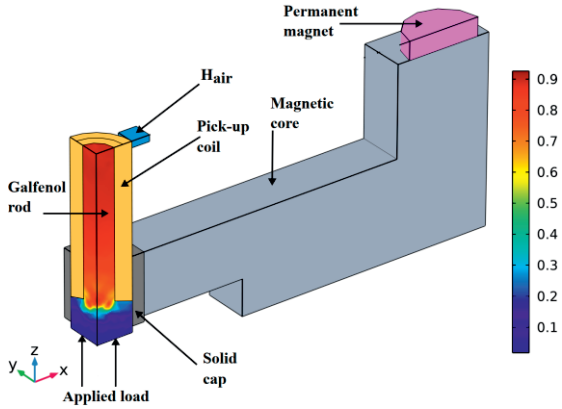

Figure 3.13 The geometry of the rod-type prototype energy harvester implemented in COMSOL for 3D FE simulations. Color bar represents the magnetic flux density norm (T) inside the galfenol rod [Publication II].

optimization of the energy harvester. A slightly modified configuration of the rod-type prototype energy harvester device is utilized for model validation incorporating a magnetic core, which is discussed in Publication II. The experimental setup of the prototype harvester device fitted with a magnetic core is discussed in Section 3.1.3. In COMSOL, the energy harvester is modeled utilizing Magnetic Field, Solid Mechanics and Electric Circuit interfaces. The Magnetic Field interface computes the electromagnetic fields by solving the Maxwell's equations, Solid Mechanics interface solves for the equation of motion whereas the Electric Circuit interface models the voltages and currents in the harvester's electric circuit. The analytical expression of the constitutive equations in (3.5), (3.8) and (3.9) are implemented in COMSOL by overriding the built-in electromagnetic and mechanical constitutive models. In the galfenol rod, the magneto-mechanical model is based on solving the combination of Ampere's and Faraday's laws in (3.17) along with the equation of motion

$$\rho\left(\frac{d^2\boldsymbol{u}}{dt^2}\right)-\nabla\cdot\boldsymbol{\sigma}(\boldsymbol{B},\boldsymbol{\varepsilon})=0. \tag{3.25}$$

where $\boldsymbol{u}$ represents the displacement vector and ρ is the mass density. In other regions, a purely electromagnetic problem is solved using (3.20) where a nonzero electrical conductivity κ is set for the solid cap and magnets and the coercive field $\boldsymbol{H}_c$ is given as a parameter for the permanent magnet. The flux density $\boldsymbol{B}$ and strain $\boldsymbol{\varepsilon}$ are expressed as in (3.18) and (3.19). For symmetry reasons, the 3D FE

analysis is carried out utilizing only $1/8^{th}$ of the harvester geometry shown in Figure 3.13. The air domain is not shown in the geometry for the sake of better visualization.

As boundary conditions, the normal component of the displacement u_z is set to zero at the top sliced boundary of the galfenol rod, whereas u_x and u_y are set to zero at the longitudinal sliced boundaries of the galfenol rod. The tangential components of the vector potential $\boldsymbol{A}$ are set to zero at the outer boundaries. The mechanical load is applied directly to the galfenol rod defined as boundary load in the axial direction indicated by arrows in Figure 3.13. The Electric Circuit interface computes the induced voltage in the pick-up coil and current across the load resistance R_{load}. The resistance of the pick-up coil $R_{\text{coil}} = 32.6\ \Omega$ and R_{load} are given as the parameters. The Electric Circuit interface is added to simulate the power flow from the pick-up coil to the load resistance, where the induced voltage in the pickup coil is computed by averaging the time derivative of the circumferential component of $\boldsymbol{A}$ over all possible paths of the coil volume Ω_{coil} as

$$\frac{N}{S_{\text{coil}}} \int_{\Omega_{\text{coil}}} \frac{\partial A_\theta}{\partial t} dV + \left(R_{\text{coil}} + R_{\text{load}}\right) i_{\text{coil}} = 0 \,. \tag{3.26}$$

The time integration of the Ampere's law is done utilizing Backward-Euler method, and the resulting discretized nonlinear algebraic equations system is solved with Newton-Raphson method.

3.3.3 3D FE analysis with an equivalent stress model

The analytical expression of the equivalent stress σ_{eq} in (3.15) is implemented in COMSOL for 3D FE analysis of the rod-type prototype harvester device presented in Section 3.1.3. The idea was to apply the equivalent stress model to analyze the magnetostrictive energy harvester and compare the simulated results with the thermodynamic magneto-mechanical model. For the sake of comparison, both models are validated against the measured results obtained from the experimental setup under similar preload and magnetic bias conditions, as discussed in Section 3.1.3. The modeled harvester geometry resembles Figure 3.13. This allows us to directly compare the simulated results obtained from two different modeling approaches. In COMSOL, purely mechanical simulation with linear elasticity is carried out in the first step. The Solid Mechanics interface

solves for the equation of motion in (3.25) to compute the stress distribution in the galfenol rod. The stress tensor only includes pure mechanical stress written as $\boldsymbol{\sigma} = \boldsymbol{S} : \boldsymbol{\varepsilon}$, where $\boldsymbol{\varepsilon}$ is the pure elastic strain tensor and $\boldsymbol{S}$ is the mechanical stiffness tensor. The next step involves electromagnetic simulation, which utilizes the equivalent stress model to predict the permeability of the galfenol material as the constitutive laws as

$$\boldsymbol{H}\left(\boldsymbol{B},\, \boldsymbol{\sigma}\right) = \frac{\boldsymbol{B}}{\mu\left(\left\|\boldsymbol{B}\right\|,\, \sigma_{\mathrm{eq}}\left(\boldsymbol{B}\right)\right)} \tag{3.27}$$

where $\mu(\|\boldsymbol{B}\|,\, \sigma_{\mathrm{eq}}(\boldsymbol{B}))$ is the local permeability utilized by COMSOL which is obtained through interpolation from the uniaxial permeability measurement data obtained from the characterization of the material. In the actuator material, the FE model is based on solving the combination of Ampere's and Faraday's laws in (3.17) and (3.18). In other regions, a purely electromagnetic problem is solved according to (3.20). Similar boundary conditions are applied for Solid Mechanics and Magnetic Field interfaces, as discussed in Section 3.3.2. The Electric Circuit interface computes the coil current and the induced voltage into the pick-up coil according to (3.26).

3.3.4 3D FE model for cantilever-beam-type harvester

From the literature review it is argued that magneto-mechanical constitutive models developed by previous researchers are mostly tested on a specific geometry or configuration of a prototype energy harvester. Thus, it is unclear whether the models are applicable to analyze energy harvesters with different geometries (such as rod-type and cantilever-beam-type geometries) and account for the influence of the varying design parameters and operating conditions. This provided a motivation to test the thermodynamic model on a completely different harvester geometry. In Publications I and II, the thermodynamic modeling approach was tested on a rod-type prototype harvester device and later validated on a modified geometry of the rod-type harvester, including an additional magnetic core and four permanent magnets. Publication IV discusses the validation of the thermodynamic magneto-mechanical model on a cantilever-beam-type prototype energy harvester device. The experimental setup and working principle of the beam type energy harvester are discussed in Section

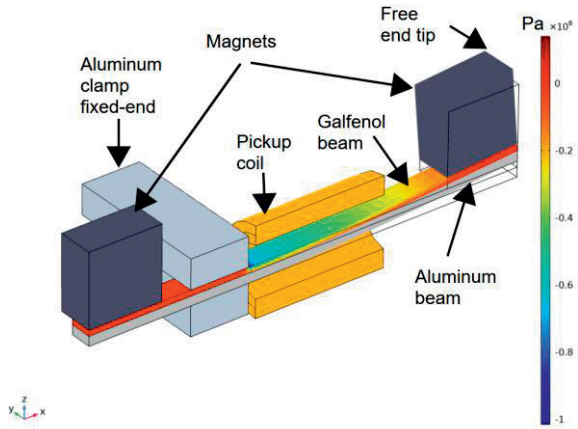

Figure 3.14 The geometry of the prototype cantilever-beam-type energy harvester implemented in 3D FE model. The color bar shows the xx-component of stress in the galfenol beam (Pa) [Publication IV].

3.1.4. The 3D FE analysis is carried out using COMSOL. For symmetry reasons, only one half of the harvester geometry is modeled for 3D FE simulations. The modeled geometry is shown in Figure 3.14. The implementation of the thermodynamic magneto-mechanical constitutive model in COMSOL Multiphysics is discussed in detail in Section 3.3.2. The experimental setup of the cantilever-beam-type harvester does not include a load resistance; therefore, the Electric Circuit interface is not utilized in the FE analysis and only the no-load voltage is studied.

Additional damping parameters are included in the equation of motion (3.25). The damping must be modeled carefully to perform structural analysis of the cantilever-beam-type harvester. The mechanical damping can be obtained from the decaying amplitude of free vibrations, whereas the rate of decay depends on how strong the damping is. The damping is important especially when the beam is vibrating close to the resonant frequency, which is the case in our study. In the Solid Mechanics interface, the structural damping is modeled using Rayleigh damping parameters by modifying the equation of motion (3.25) written as

$$\rho\left(\frac{d^2\boldsymbol{u}}{dt^2}+\alpha_{\mathrm{dM}}\frac{d\boldsymbol{u}}{dt}\right)-\nabla\cdot\left(\boldsymbol{\sigma}(\boldsymbol{B},\boldsymbol{\varepsilon})+\beta_{\mathrm{dK}}\frac{\partial\boldsymbol{\sigma}(\boldsymbol{B},\boldsymbol{\varepsilon})}{\partial t}\right)=0 \tag{3.28}$$

where α_{dM} and β_{dK} are the mass and stiffness damping parameters, respectively. The Rayleigh damping in terms of damping ratio ζ is obtained from

$$\zeta = \frac{1}{2}\left(\frac{\alpha_{\mathrm{dM}}}{2\pi f_0} + \beta_{\mathrm{dK}} 2\pi f_0 \right) \tag{3.29}$$

where f_0 is the resonant frequency. It is common in mechanical engineering to utilize a viscous damping model by using bulk viscosity and shear viscosity obtained as material parameters. The Rayleigh damping is equivalent to viscous damping by setting $\alpha_{\mathrm{dM}} = 0$, where the damping is only provided by the stiffness term β_{dK}. The coil current is zero due to the no-load condition and only the induced voltage V_{ind} is computed from

$$V_{\mathrm{ind}} = \frac{N}{S_{\mathrm{coil}}} \int_{\Omega_{\mathrm{coil}}} \frac{\partial A_0}{\partial t} d\Omega \,. \tag{3.30}$$

The time integration is carried out using Generalized Alpha method instead of the Backward-Euler method, since the latter causes numerical damping [96]. The Generalized Alpha method is a second-order backward differential formulation with a parameter to control the damping at higher frequencies. The resulting nonlinear system is solved with Newton Raphson iterations.

4 RESULTS AND DISCUSSION

This chapter summarizes the results obtained from the experimental setups and magneto-mechanical constitutive models presented in Chapter 3. The results are summarized in the order of the Publications I–VI.

4.1 Material characterization

In Publication I, the material characterization setup presented in Section 3.1.1 was utilized to obtain the stress dependent magnetization *B*–*H* curves. As discussed earlier, single-valued *B*–*H* curves can be utilized for galfenol due to negligible hysteresis losses. The single-valued *B*–*H* curves were obtained by magnetizing the galfenol sample and then applying the static mechanical preload σ ranging from 0 to 80 MPa. The measured single-valued *B*–*H* curves are shown in Figure 4.1. The negative σ values shown in Figure 4.1 indicate that the applied stress is compressive. The model parameters α_i, β_i, and γ_i were obtained by fitting the analytical expression of the energy density function (3.5) to the single-valued *B*–*H* curves. The fitting was performed for the σ values ranging from 40 to 70 MPa. The values of Young's modulus and Poisson's ratio utilized in the model were 75 GPa and 0.4, respectively. The results from the fitting are shown in Figure 4.2. The fitting range of 40–70 MPa was chosen as it falls within the range at which output power was measured. The degrees of the polynomials for the energy

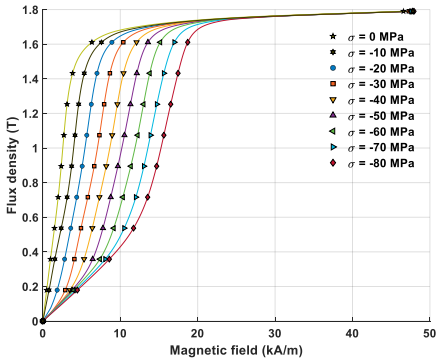

Figure 4.1 The stress-dependent measured *B*–*H* curves at different compressive preload σ values.

Table 4.1 Model parameters for σ values ranging from 40 to 70 MPa [Publication I].

Parameter	Value (J/m^3)	Parameter	Value (J/m^3)
α_1	9.217×10^3	α_8	-1.071×10^4
α_2	-1.028×10^4	α_9	2.754×10^3
α_3	1.854×10^4	α_{10}	-399.5
α_4	-3.159×10^4	α_{11}	24.99
α_5	4.286×10^4	β_1	4.647×10^6
α_6	-4.082×10^4	γ_1	1.128×10^{10}
α_7	2.595×10^4	γ_2	-6.977×10^5

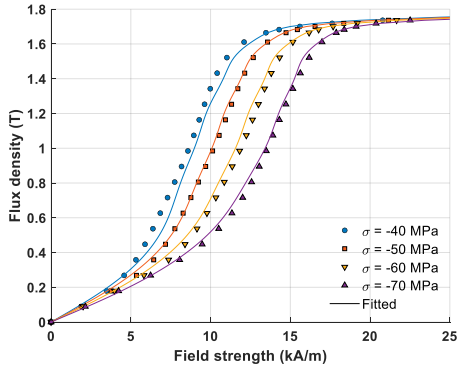

Figure 4.2 Measured and fitted *B*–*H* curves under compressive stress σ values from 40 to 70 MPa.

expression was chosen such that it fits well with the measured magnetization curves with small discrepancies. The results from Figure 4.1 and Figure 4.2 indicate that the permeability of the galfenol material decreases with an increase in the preload. The relative differences between measured and simulated magnetic field strengths are 7.92% for 40 MPa, 5.03% for 50 MPa, 5.19% for 60 MPa, 2.98% for 70 MPa preload values. It is worth noting that the deviation between measured and fitted curves changes and depends on the choice of the σ values used in the fitting. Furthermore, the wider the stress range, the lower the accuracy. The values of the model parameters α_i, β_i and γ_i for $n_\alpha = 11$, $n_\beta = 1$ and $n_\gamma = 2$ are presented in Table 4.1.

4.2 2D axisymmetric FE model

In Publication I, the performance of a rod-type galfenol-based prototype energy harvester was analyzed to determine the influence of preload σ, dynamic load $\Delta\sigma$ and load resistance R_{load} over the harvested output power. The energy harvester

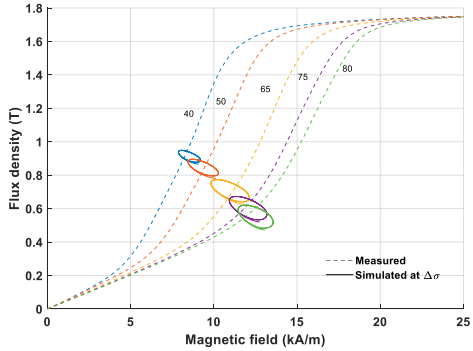

Figure 4.3 Measured *B–H* curves at different σ values and simulated dynamic hysteresis loops ΔB under constant cyclic mechanical loading $\Delta\sigma$ of 8 MPa [Publication I].

setup presented in Section 3.1.2 was excited using different σ and $\Delta\sigma$ values ranging from 20–80 MPa and 4–8 MPa, respectively. The excitation frequency of mechanical vibrations was kept constant at 100 Hz throughout the experiments. The 2D axisymmetric FE model presented in Section 3.3.1 was validated against the measurement results obtained under varying σ, $\Delta\sigma$ and R_{load} values. The change in the magnetic flux density ΔB inside the galfenol sample was studied under sinusoidal mechanical stress to determine the influence of σ over ΔB. The simulated results were obtained by applying σ ranging from 20 to 80 MPa while keeping a constant $\Delta\sigma$ of 8 MPa throughout the FE simulations. The simulated ΔB and the corresponding magnetic fields H were averaged over the H_{bar} region shown in Figure 3.12. ΔB under sinusoidal mechanical vibrations is plotted as dynamic hysteresis loops over the measured *B–H* curves obtained from material characterization. The measured *B–H* curves under σ values ranging from 40 to 80 MPa and the corresponding simulated hysteresis loops of ΔB are shown in Figure 4.3. The change in B is represented by ΔB loops, which can be utilized to determine the optimal σ value. The reason for plotting the σ range of 40–80 MPa is to avoid any overlap of the simulated ΔB loops over the measured *B–H* curves, even though the simulations were carried out for the complete σ range from 20–80 MPa. The results clearly demonstrate the influence of σ over ΔB, where the area of hysteresis loop represents the average power for the corresponding σ value. The results from ΔB loops show that the largest peak-to-peak variations of B occur at σ = 75 MPa indicating an optimal value that will generate the highest output power.

To validate the optimal σ of 75 MPa shown in Figure 4.3, a comparison was carried out between the measured output powers obtained by varying σ from 40 to 80 MPa using a constant $\Delta\sigma$ of 8 MPa. Furthermore, for each σ value the

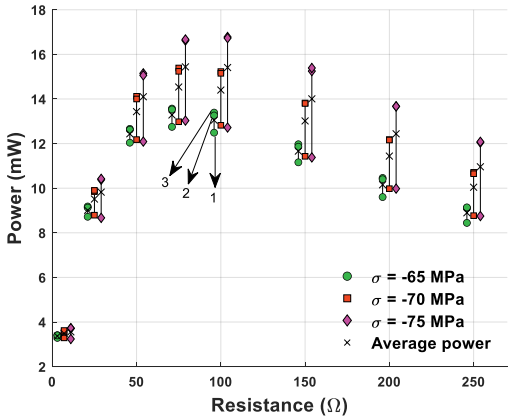

Figure 4.4 Measured output powers obtained from three consecutive measurement sessions (1, 2 and 3) using σ = 65–75 MPa at constant $\Delta\sigma$ = 8 MPa. The markers represent the measured values during each session and the cross represents the average power. The resistance values are the same for each preload case and the horizontal shift in the markers is done for readability [Publication I].

influence of R_{load} over the measured output power was studied by varying the R_{load} from 5 Ω to 250 Ω to determine the optimal value yielding maximum output power. The experiments were conducted three times to determine the repeatability of the measurements and to provide an accurate comparison between the measured and simulated results. The repeatability of the measurements for three consecutive sessions is shown in Figure 4.4. The measured output powers were obtained using a constant $\Delta\sigma$ of 8 MPa and varying σ and R_{load} values of 65 to 75 MPa and 5 to 250 Ω, respectively. The markers represent the measured power for each session, whereas the crosses represent their average value. Moreover, the R_{load} values are the same for each σ case and the horizontal shift in the markers for 65 MPa and 75 MPa is done for readability. The range of σ values in Figure 4.4 is chosen mainly because the maximum output power falls within that range. The results depict the sensitivity of the measurements to the external conditions that include misalignments between the galfenol sample, magnets and the vertical loading system, warm-up time of the measurement devices and measurement tolerances.

The comparison between the measured and simulated average output powers is shown in Figure 4.5. The measured (a) and simulated (b) results were obtained under constant $\Delta\sigma$ of 8 MPa to demonstrate the influence of change in σ and R_{load}. The measured output power is plotted as the average of three measurement sessions to provide a reasonable comparison with the simulated output power. The results from Figure 4.5 show that the output power changes as a function of

preload and load resistance. The output power increases with the increase in σ and R_{load} and a maximum simulated power of 15.4 mW was computed at σ = 75 MPa and R_{load} = 75 Ω. The same pattern can be seen from Figure 4.3, where ΔB changes as a function of σ and reaches maximum at σ = 75 MPa. The value of ΔB at constant $\Delta\sigma$ of 8 MPa was computed to be 153 mT and 147 mT at 75 MPa and 80 MPa. The simulated results in Figure 4.5 (b) accurately predict the optimal σ and R_{load} values, validating the modeling approach.

For FE simulations, a time step Δt length of 100 µs (100 steps per one fundamental period) was utilized to compute the output power under dynamic mechanical loading of 100 Hz. A magnetostatic solution was utilized as an initial state and three fundamental periods were simulated to ensure steady state. The simulation time for one time step was computed to be approximately 130 ms independent of the used Δt. The total simulation time was computed as the time required to complete 56 simulations to compute the simulated output powers

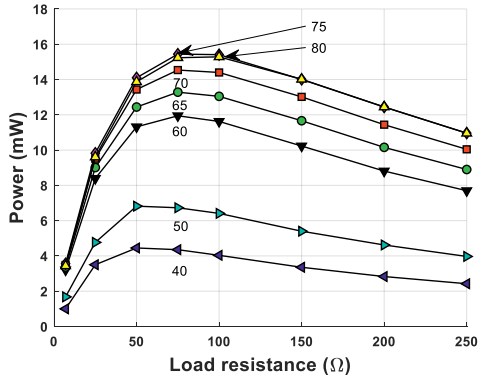

(a)

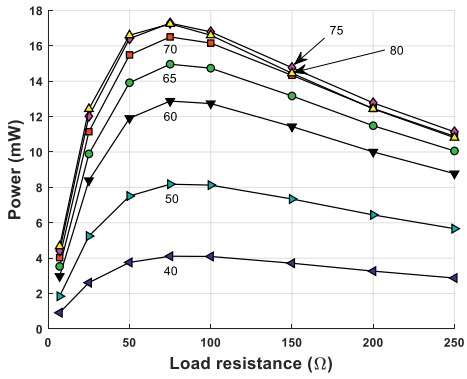

(b)

Figure 4.5 Measured (a) and simulated (b) average output powers obtained under varying σ = 40–80 MPa at a constant $\Delta\sigma$ = 8 MPa [Publication I].

Table 4.2 Simulation times and output power computed at different time step (Δt) lengths. The total simulation time was computed for 56 simulations shown in Figure 4.5 (b) [Publication I].

Time step Δt (µs)	Total simulation time (mins)	Power difference w.r.t Δt = 100 (µs)
200	20	-2.7 %
100	36	0 %
50	72	1.5 %
33	86	1.9 %
25	133	2.2 %
20	165	2.4 %
12.5	188	2.5 %

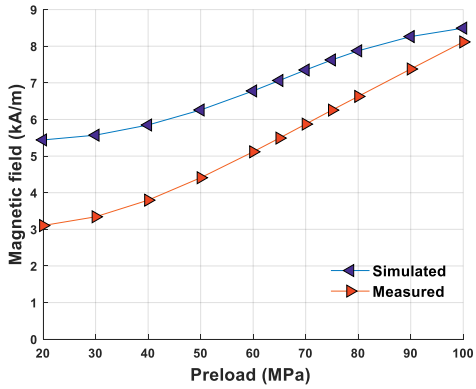

Figure 4.6 Measured and simulated magnetic field strength H near the middle part of the galfenol sample at σ ranging from 20–100 MPa under constant $\Delta\sigma$ of 8 MPa. The results are plotted as the average values of H [Publication I].

shown in Figure 4.5 (b). The choice of Δt = 100 µs was made after analyzing and comparing the percentage differences in the simulated output powers obtained using different Δt values with respect to the 100 µs case. The results of the comparison are presented in Table 4.2. The results depict that, for Δt = 12.5 µs, the output power increases by 2.5 percent, with an additional computational cost of 152 minutes. However, using Δt = 200 µs decreases the output power to 2.7 percent, saving 16 minutes. Therefore, the choice of Δt = 100 µs was considered a good compromise between the solution accuracy and computation time.

To investigate the deviations between measured and simulated output powers presented in Figure 4.5, a comparison between measured and simulated H in the air near the middle part of the galfenol sample (H_{air} region in Figure 3.12) was conducted, as shown in Figure 4.6. The results show that H in the air increases as σ increases. In addition, the model overestimates the magnetic field compared to measured results and the difference is higher for the lower σ values. This is because the model underestimates the material permeability like seen in the 40

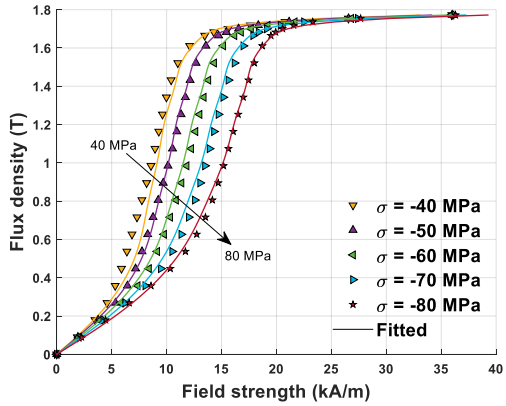

Figure 4.7 Measured and simulated *B*–*H* curves for compressive stress σ values from 40 to 80 MPa.

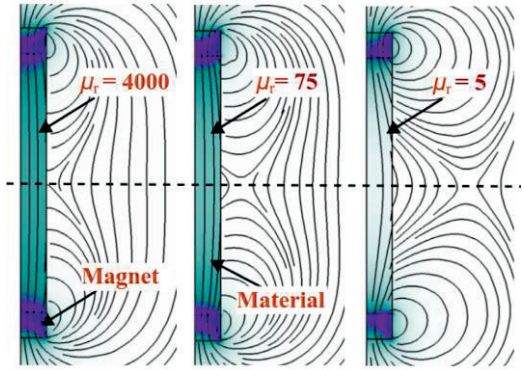

Figure 4.8 The field lines of magnetic flux density *B* simulated by varying the relative permeability (μ_r). The rectangular sample is magnetized by two permanent magnets attached at both ends whereas the dashed line denotes middle part of the sample [Publication I].

MPa case, which is also evident by comparing measured and simulated *B*–*H* curves shown in Figure 4.2 and Figure 4.7. The reason why *H* in the air increases with an increase in the preload can be illustrated with Figure 4.8. A rectangular sample with relative permeability μ_r was simulated to analyze the effect of change in μ_r upon magnetic flux density *B* inside the sample shown in Figure 4.8.

It can be seen that a larger share of total flux is pushed into the air as μ_r decreases from 4000 to 5. This is evident from the bending flux lines near the middle part of the sample marked by the dashed line shown in Figure 4.8. The same happens when the galfenol rod is subjected to a compressive preload causing a decrease in the permeability of the material and reducing the total flux inside the rod. To further validate this, FE simulations were carried out by

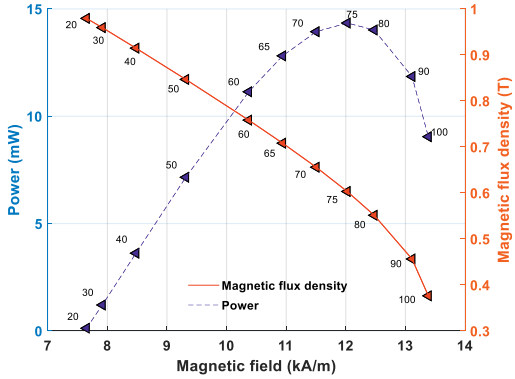

Figure 4.9 Simulated B (mean values) inside the galfenol sample versus simulated output power obtained by varying the preload from 20–100 MPa while keeping $\Delta\sigma$ = 8 MPa and R_{load} = 75 Ω throughout the simulations [Publication I].

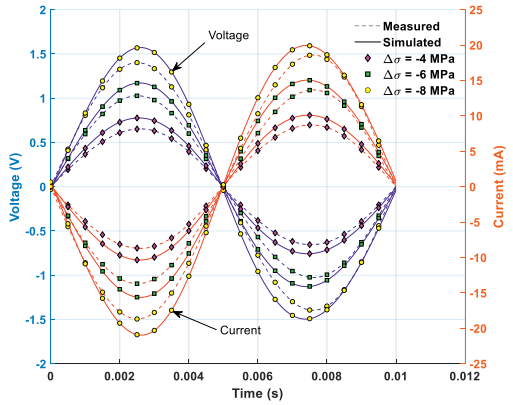

Figure 4.10 Comparison between measured and simulated output voltage and current waveforms obtained under varying $\Delta\sigma$ from 4–8 MPa using σ = 65 MPa and R_{load} = 75 Ω [Publication I].

changing the σ values from 20 to 100 MPa while keeping $\Delta\sigma$ = 8 MPa and R_{load} = 75 Ω throughout the simulations.

Figure 4.9 shows the simulated average output power and mean value of B computed at the middle part of the galfenol sample (H_{bar} region shown in Figure 3.12). The results evidence a decrease in the magnetic flux density inside the sample as the preload increases. Furthermore, the maximum output power is obtained at σ = 75 MPa which further validates the existence of an optimal preload value. Finally, the influence of a change in the amplitude of $\Delta\sigma$ on the performance of the energy harvester was tested by varying $\Delta\sigma$ from 4 to 8 MPa while keeping σ and R_{load} at 65 MPa and 75 Ω, respectively. The comparison of measured and simulated output currents and voltages is presented in Figure 4.10. As expected, the results show that the output voltage and current increases by

increasing $\Delta\sigma$ from 4 to 8 MPa. In addition, the simulated results closely follow the measured results with small discrepancies, which can be explained by model limitations in underestimating the material permeability and sensitivity of the measurements to the external conditions.

4.3 3D FE model for the rod-type harvester

Publication II presents a 3D FE analysis of the rod-type prototype energy harvester device fitted with a magnetic core presented in Section 3.1.3. The measurements were obtained from the prototype energy harvester device developed in [42] to validate the modeling approach. The 3D model provides a complete understanding of coupled magneto-mechanical phenomenon in the magnetostrictive material. The implementation of the thermodynamic magneto-

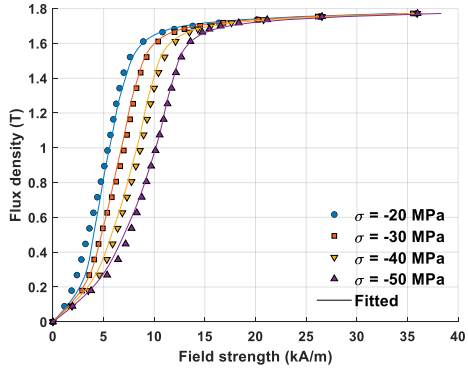

Figure 4.11 Measured (markers) and fitted (solid lines) *B–H* curves obtained under different σ values from 20–50 MPa [Publication II].

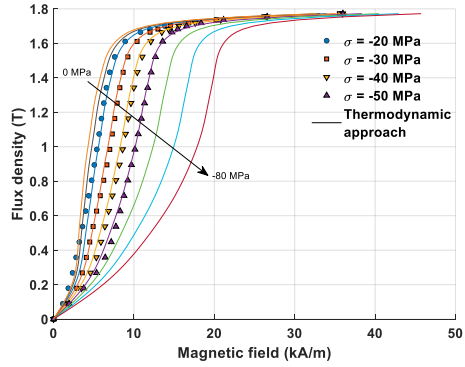

Figure 4.12 Simulated *B–H* curves (solid lines) obtained by utilizing the thermodynamic model under σ values from 0 to 80 MPa. The markers represent the measured *B–H* curves used for fitting the model [Publication II].

Table 4.3 Model parameters for σ values ranging from 20 to 50 MPa [Publication II].

Parameter	Value (J/m^3)	Parameter	Value (J/m^3)
α_1	6.892×10^3	α_8	-1.631×10^4
α_2	-1.727×10^4	α_9	3.805×10^3
α_3	4.510×10^4	α_{10}	-509.5
α_4	-8.087×10^4	α_{11}	29.89
α_5	9.798×10^4	β_1	-1.761×10^6
α_6	-8.032×10^4	γ_1	8.132×10^9
α_7	4.444×10^4	γ_2	-1.766×10^5

mechanical model in COMSOL for 3D FE analysis is presented in Section 3.3.2. In Publications II and III, the fitting was performed for the σ values ranging from 20 to 50 MPa to obtain the model parameters α_i, β_i and γ_i. The results of the measured and fitted *B*–*H* curves at σ ranging from 20 to 50 MPa are shown in Figure 4.11. The chosen range of σ provides a relatively good fitting against the measured *B*–*H* curves. To validate this, the simulated results of the *B*–*H* curves produced by the thermodynamic model in the range of 0–80 MPa are shown in Figure 4.12. The results show that the narrow fitting range of 20–50 MPa corresponds well to the measured magnetization curves. The relative differences between measured and simulated magnetic field strengths are 4.96% for 20 MPa, 2.12% for 30 MPa, 2.34% for 40 MPa, 7.33% for 50 MPa preload values. However, outside the fitting data range (below 20 and above 50 MPa), the simulated *B*–*H* curves deviate from the measured ones shown in Figure 4.1. The values of the fitting parameters α_i, β_i and γ_i for n_α = 11, n_β = 1 and n_γ = 2 are presented in Table 4.3.

Palumbo and Zucca in [42] carried out an extensive set of experiments to determine the influence of operating conditions including mechanical preload, dynamic load, magnetic bias, excitation frequency, load resistance, and coil parameters over the measured output power. It has been shown that a change in the operating conditions changes the measured output power. Therefore, the operating conditions need to be tuned individually to maximize the performance of the harvester. Furthermore, finding the optimal values of the mechanical bias and load resistance was not so trivial, because they depend heavily on the value of magnetic field bias. The measured output power obtained from the energy harvester setup utilizing permanent magnets presented in [42] was utilized to validate the model. The measured output power was obtained under sinusoidal mechanical vibrations of 100 Hz using constant $\Delta\sigma$ of 8 MPa and R_{load} of 160 Ω. The change in the magnetic bias was realized by utilizing two different

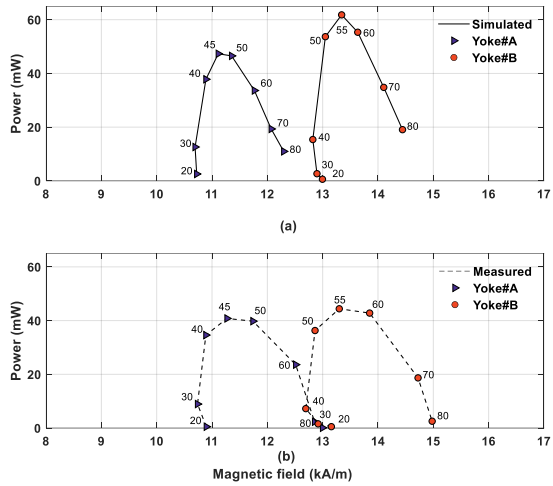

Figure 4.13 The comparison between simulated (a) and measured (b) output powers obtained by varying σ from 20 to 80 MPa while using constant $\Delta\sigma$ of 8 MPa and R_{load} of 160 Ω for both Yoke#A and Yoke#B cases [Publication II].

configurations of the rod-type energy harvester (Yoke#A and Yoke#B) presented in Figure 3.9. The magnetic bias in Yoke#A configuration was provided by two permanent magnets, whereas Yoke#B configuration had four magnets in total. For both cases (Yoke#A and Yoke#B), the preload varied from 20 to 80 MPa to determine the influence of changing preload and magnetic bias upon the measured average output power.

The 3D FE simulations were carried out by utilizing similar operating conditions as the measured results for both Yoke#A and Yoke#B cases for validation. The capability of the thermodynamic magneto-mechanical model was tested to analyze the rod-type magnetostrictive energy harvester under varying σ and magnetic bias. The simulated (a) and measured (b) average output powers obtained by varying σ from 20 to 80 MPa for the case of Yoke#A and Yoke#B are presented in Figure 4.13. It was difficult to predict the magnetic bias accurately with the FE simulations because the information related to the remanence flux density (B_r) of the magnets and the airgaps between the solid caps, magnetic core and galfenol rod was not available. Therefore, B_r was tuned once such that the simulated H near the middle part of the sample closely matches the measured H using the Hall probe for the preload values of 45 and 55 MPa at which maximum output power was obtained as shown in Figure 4.13. However, no tuning was performed to match the simulated and measured output powers for other preload values. The remanence flux density was kept constant throughout

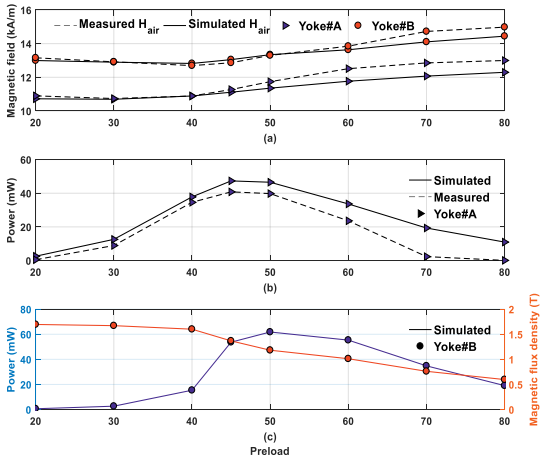

Figure 4.14 Comparison between measured and simulated magnetic fields for Yoke#A and Yoke#B cases (a). Simulated and measured average output powers for Yoke#A case (b). Simulated B (mean value) inside the galfenol sample (region B_{bar} in Figure 3.12) and average output power for Yoke#B case (c). The results were obtained by varying σ from 20 to 80 MPa and using constant $\Delta\sigma$ and R_{load} values of 8 MPa and 160 Ω, respectively [Publication II].

the simulations. The results clearly show that the output power changes as a function of magnetic bias and mechanical preload. The model was able to reasonably reproduce the measurement results, but with slightly larger amplitudes of the output power.

To understand the reason behind the deviations between simulated and measured output powers, a comparison was conducted between the mean values of measured and simulated H values computed near the middle part of the sample (region H_{air} in Figure 3.12). The results from the simulated and measured H for both Yoke#A and Yoke#B are shown in Figure 4.14 (a). Furthermore, the measured and simulated average output powers for Yoke#A, and the simulated results of the B inside the sample along with the average output power for the Yoke#B are shown in Figure 4.14 (b) and (c), respectively. The results from Figure 4.14 (a) show that the model slightly underestimates the magnetic field compared to the measured one for σ range of 60–80 MPa. However, the simulated results are in good agreement for the σ range of 20–50 MPa used in the fitting. The simulated results in Figure 4.14 (c) illustrate that material permeability decreases with an increase in the preload. The difference between measured and simulated results arises partly because the simulations do not account for the small air gaps due to manufacturing tolerances between the core, solid caps, and galfenol rod. This decreases the total reluctance of the magnetic circuit and causes an increase in the simulated power. Moreover, the fact that the magnetization

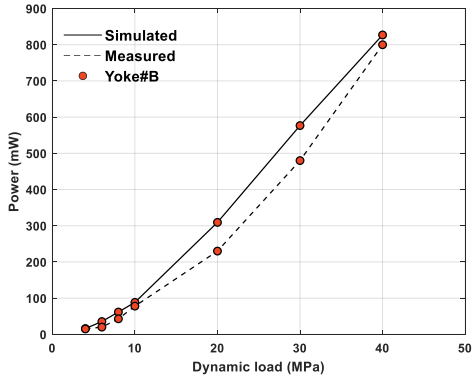

Figure 4.15 The comparison among measured and simulated average output power obtained using different $\Delta\sigma$ values for Yoke#B case. The results are obtained using constant σ of 55 MPa and R_{load} of 160 Ω under sinusoidal excitations of 100 Hz [Publication II].

properties of the core material were not known also introduces inaccuracies in the model. Furthermore, small discrepancies were caused by the measurement uncertainties and repeatability issues discussed in Section 4.2. Therefore, the comparison should be done keeping in view the limitations of the model and repeatability of the measurements.

In the next stage, the influence of $\Delta\sigma$ over the average output power was studied by increasing the $\Delta\sigma$ from 4 MPa to 40 MPa. Figure 4.15 shows the comparison between measured and simulated average output powers obtained under constant σ of 55 MPa and R_{load} of 160 Ω for the case of Yoke#B. The results show that the output power increases with an increase in the amplitude of $\Delta\sigma$. While there are some deviations between measured and simulated output powers, the model was able to follow the trend of the measurement results. The results from Figure 4.14 and Figure 4.15 validates the existence of the optimal preload σ and dynamic load $\Delta\sigma$ values, which needs to be tuned each time the magnetic bias changes. This was also shown experimentally in [42], where maximum output power for each σ case (20–80 MPa) occurs at different magnetic field bias values.

4.4 3D FE analysis with an equivalent stress model

In Publication III, the equivalent stress model presented in Section 3.2.2 was utilized for the first time to analyze a magnetostrictive energy harvester. The model implementation in COMSOL for 3D FE analysis of the prototype energy harvester is presented in Section 3.3.3. The stress-dependent measured *B*–*H*

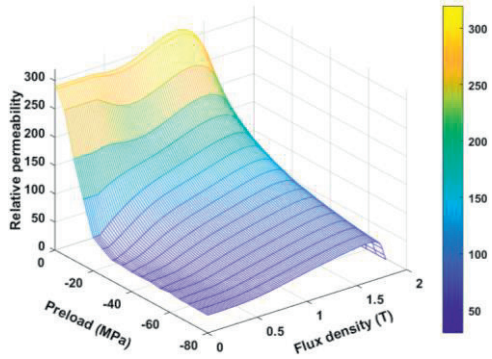

Figure 4.16 Relative permeability vs magnetic flux density interpolated utilizing different σ values from 0 to 80 MPa. ([Publication III], © 2021)

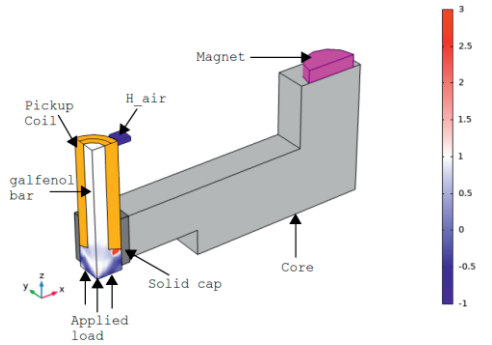

Figure 4.17 The 3D FE geometry of the rod-type galfenol-based prototype energy harvester fitted with a magnetic core. The color bar indicates the ratio of the stress distribution σ_{eq}/σ_{zz}. ([Publication III], © 2021).

curves shown in Figure 4.1 were utilized to obtain the relative permeability of the material. The results shown in Figure 4.16 present the relative permeability of the galfenol sample interpolated from the measured *B*–*H* curves. The model is validated against the measurement results obtained from the rod-type prototype energy harvester setup presented in Section 3.1.3. The 3D FE simulations were carried out keeping a constant $\Delta\sigma$ of 8 MPa and R_{load} of 160 Ω under sinusoidal mechanical vibrations of 100 Hz. The same experimental setup and operating conditions were utilized in Publication II to validate the thermodynamic magneto-mechanical model. This allows us to compare the results from two different modeling approaches. The geometry utilized for the FE simulations is shown in Figure 4.17.

To visualize the multiaxial nature of the stress, the stress distribution inside the galfenol rod is shown in Figure 4.17 as the ratio σ_{eq}/σ_{zz} between the equivalent stress and the zz-component of the stress. The results show that the zz-component

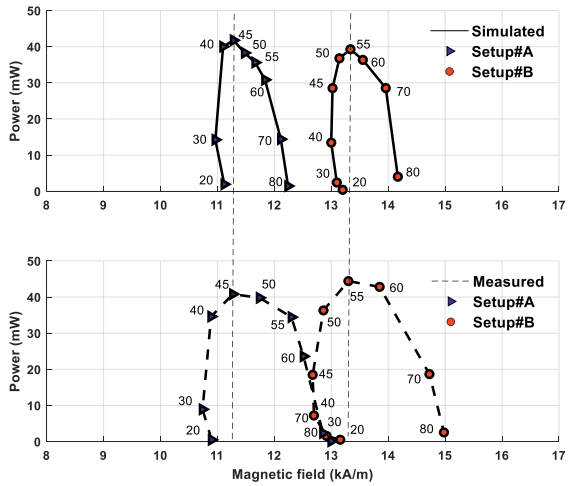

Figure 4.18 Measured and simulated average output power obtained under different σ values from 20 to 80 MPa for Yoke#A and Yoke#B cases. The results are obtained with a constant $\Delta\sigma$ of 8 MPa and R_{load} of 160 Ω under 100 Hz vibration frequency ([Publication III], © 2021).

of stress is dominant in the middle part of the galfenol rod, but the regions surrounded by the solid cap show signs of multiaxial stress. This is because the orientation of the magnetic flux density in the middle of the sample is parallel to the applied stress. However, the flux density orientation turns at the region closer to the core, causing the magneto-mechanical problem to become multiaxial. Using the equivalent stress model for correctly interpolating the permeability in the regions close to the core is thus justified.

For the energy harvesting setup, the FE simulations were carried under dynamic mechanical vibrations to analyze the influence of change in σ and magnetic bias over the harvested output power. The measured and simulated average output powers obtained by σ ranging from 20 to 80 MPa for the cases of Yoke#A and Yoke#B are shown in Figure 4.18. The results show that the model is able to successfully predict the preload values yielding maximum output power. However, the model struggles to accurately predict the magnetic bias at different σ values. This is because the model does not consider the small airgaps between galfenol rod, solid cap and core. In addition, the core was modeled utilizing built-in magnetization properties from the COMSOL library since the magnetization properties of the actual core material were not known. These limitations affect the total reluctance of the magnetic circuit. To provide a reasonable comparison between measured and simulated results shown in Figure 4.18, the B_r of the magnets was tuned once to match the magnetic field in the air measured at the region H_air in Figure 4.17. The tuning was performed for the σ values of 45 and

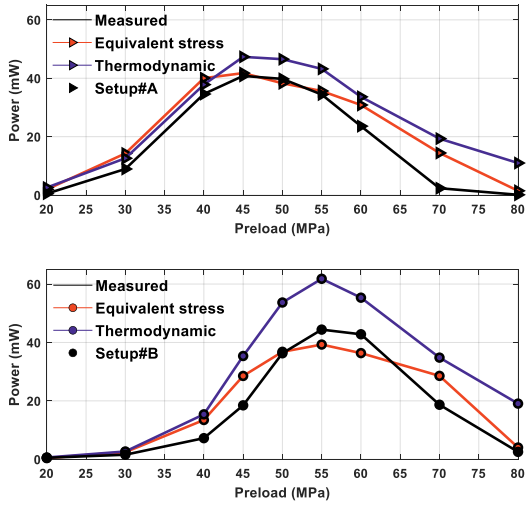

Figure 4.19 Measured and simulated average output powers obtained at σ values ranging from 20 to 80 MPa using the equivalent stress model and thermodynamic magneto-mechanical model ([Publication III] © 2021).

55 MPa indicated by the vertical dashed lines at which maximum output power is obtained. The B_r was kept constant for the remaining σ values during all simulations. The simulated results obtained from the equivalent stress model were also compared with those obtained from the directly coupled 3D FE model utilizing the thermodynamic approach discussed in Section 4.3.

The comparison between the measured and simulated output powers obtained from two different modeling approaches is shown in Figure 4.19. Both models are able to reproduce the measurement results with reasonable accuracy for both the Yoke#A and Yoke#B cases. However, there are some deviations between measured and simulated average output powers. The deviations can be explained by the limitations of the models and partly by the repeatability issues and measurement uncertainties discussed earlier in Section 3.3.2. The limitation of the thermodynamic model is that it is unable to fit to the measured B–H curves for the wider σ range, as can be seen from Figure 4.12. In addition, the choice of σ values utilized for fitting the model as well as the degree of polynomial coefficients for model parameters α_i, β_i, and γ_i changes the simulated output power. The limitation of the equivalent stress model is that the stress tensor only includes the stress due to mechanical loading and does not consider the stress caused by magnetostriction. Therefore, the total simulated stress is less than the actual stress, which affects the simulated magnetic field bias. This explains the difference in the simulated and measured magnetic field biases in Figure 4.18. It

was observed that small variations in the magnetic field bias significantly change the average output power obtained at a constant σ value. This is evident from the measured results in Figure 4.18 (a) since changing the magnetic field bias will change the optimal preload value and maximizing output power would again require tuning the preload.

4.5 3D FE model for cantilever-beam-type harvester

Publication IV presents the validation of the thermodynamic magneto-mechanical model to analyze a cantilever-beam-type galfenol-based prototype energy harvester device. The experimental setup and working principle of the cantilever-beam-type prototype energy harvester are presented in Section 3.1.4. The idea was to test the capability of the thermodynamic model to analyze different geometric configurations (rod-type and beam-type geometries) of the magnetostrictive energy harvesters. The 3D FE model presented in Section 3.3.4 was utilized to analyze the behavior of the beam-type magnetostrictive energy harvester under sinusoidal mechanical vibrations of varying amplitudes and frequencies. For the energy harvesting setup presented in Section 3.1.4, the results are categorized into the following two sections.

4.5.1 Beam resonant frequency

The literature reports that the performance of the beam-type energy harvester reaches its maximum when it operates at the resonant frequency [49], [86]. Furthermore, the resonant frequency of the cantilever beam changes as a function of vibration amplitude and magnetic bias. Therefore, the resonant frequency of the cantilever beam shown in Figure 3.14 was first calculated analytically as

$$f_0 = \frac{1}{2\pi}\sqrt{\frac{3EI}{\left(M + m_{\text{eff}}\right)l^3}} \tag{4.1}$$

where f_0 is the resonant frequency and, E is the effective Young's modulus of the combined aluminum-galfenol beam taken as 70 MPa. The term I represents the second moment of inertia; M is the tip mass of 9.71 grams which consists of a PETG cap and the magnet; l represents effective beam length of 38 mm measured

after the clamp; and m_{eff} is the effective beam mass of 2.2 grams computed for l = 38 mm. The resonant frequency computed analytically from (4.1) is 189 Hz.

In the next stage, the resonant frequency of the beam with magnets attached at both ends was obtained experimentally utilizing a free vibration test. During the free vibration test, the decaying amplitude of the tip displacement shown in Figure 4.20 was measured using a precision laser sensor. A resonant frequency of 200 Hz was computed by measuring a time of 40 ms over eight consecutive periods, as indicated by the arrow in Figure 4.20. As discussed in Section 3.3.4, the 3D FE model requires information related to the physical parameter of damping ratio ζ. The damping ratio was computed from the free vibrations in Figure 4.20 utilizing a logarithmic decrement method as

$$\zeta = \frac{\ln\left(\frac{X_k}{X_{k+n}}\right)}{2\pi n} \tag{4.2}$$

where X_k and X_{k+n} are the k^{th} and $(k+n)^{\text{th}}$ values of the peak displacement amplitude. A value of $\zeta = 0.0145$ was computed using (4.2) for the corresponding eight consecutive periods of the free vibrations shown in Figure 4.20.

To determine the effect of magnetostriction upon beam resonant frequency, the permanent magnets at both ends of the beam were replaced by solid iron cubes of similar size and weight. The frequency sweep method was utilized to determine the resonant frequency of the beam by measuring the tip displacement when the beam was excited under forced sinusoidal vibrations. Two sets of experiments

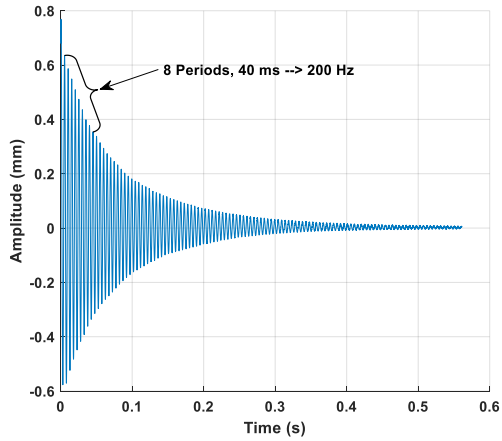

Figure 4.20 The measured resonant frequency of 200 Hz obtained from the decaying amplitude of tip displacement using free vibration test [Publication IV].

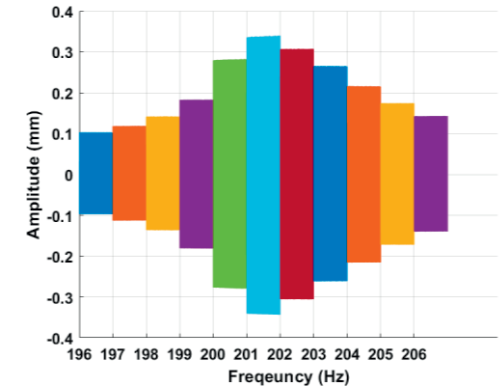

(a)

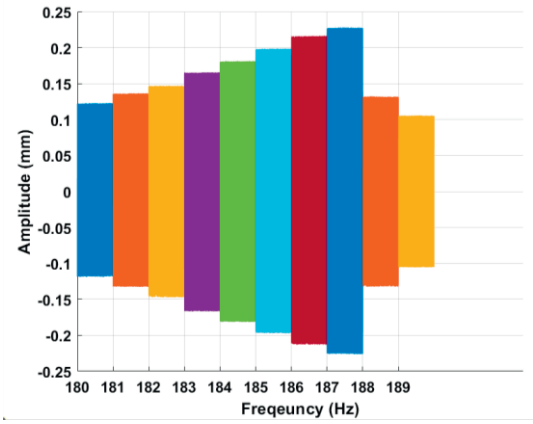

(b)

Figure 4.21 Measured tip displacement using 1*g* acceleration utilizing frequency sweep method for the cases of permanent magnets (a) and iron cubes (b). For each vibration frequency the displacement results were measured for 6 continuous seconds [Publication IV].

were carried out using a constant vibration amplitude of 1*g* acceleration. In the first set of experiments, the beam was magnetized by permanent magnets at both ends and the frequency sweep was performed around the resonant frequency of 200 Hz obtained from the free vibration test shown in Figure 4.20. In the second set of experiments, the permanent magnets were replaced by solid iron cubes and the frequency sweep was performed around the resonant frequency of 189 Hz computed analytically using (4.1). The measured results of the tip displacement obtained by sweeping the vibration frequencies for the case of permanent magnets and iron cubes are shown in Figure 4.21(a) and Figure 4.21 (b), respectively. The results depict that the magnetostriction increases the resonant frequency from 187 Hz in Figure 4.21 (a) to 201 Hz Figure 4.21 (b). The increase in the resonant

Table 4.4 Comparison between measured, simulated, analytically calculated and free vibration resonant frequencies. The measured and simulated results are obtained from frequency sweeps [Publication IV].

	Measured	**Simulated**	**Analytical**
With magnetostriction	201 Hz	200 Hz	-
Without magnetostriction	187 Hz	184 Hz	189 Hz

frequency can be explained by the so-called ΔE effect. As Löffler and Daniel explained in [97] and [98], the ΔE effect states that the magnetization of the magnetostrictive material increases E, and, according to (4.1), an increase in E consequently increases f_0.

3D FE simulations were performed for the frequency sweep with permanent magnets and iron cubes to determine the capability of the model to capture the influence of magnetostriction on the resonant frequency. In COMSOL, the mechanical damping was realized using Rayleigh damping given in (3.29). The damping parameters were computed using f_0 of 201 Hz, which was kept constant throughout the simulations. A resonant frequency of 200 Hz was obtained from the simulation with magnetostriction (permanent magnets) and 184 Hz without magnetostriction (iron cubes). Table 4.4 provides the comparison among measured, simulated, and analytically calculated resonant frequencies, showing that the thermodynamic magneto-mechanical model was successfully able to predict the increase in the resonant frequency caused by magnetostriction.

4.5.2 Energy harvester setup

For energy harvesting, the cantilever beam was subjected to sinusoidal mechanical vibrations of different acceleration amplitudes ranging from 0.5g to 2g. For each acceleration amplitude, the frequency sweep was performed from 196 to 206 Hz to determine the influence of vibration amplitude upon the resonant frequency of the energy harvester. The experiments were conducted three times to determine the repeatability and to provide a reasonable comparison with the simulated results. The comparison between the measured and simulated open circuit voltages (rms) and tip displacements is shown in Figure 4.22 and Figure 4.23. The measured results depict that the resonant frequency decreases from 202 Hz to 198 Hz with an increase in the vibration amplitude from 0.5g to 2g. The model was able to accurately predict the resonant frequencies under different vibration amplitudes with a percentage error of less than 2 percent. The deviations among the measured results in Figure 4.22 (a) and Figure 4.23 (a) are shown by

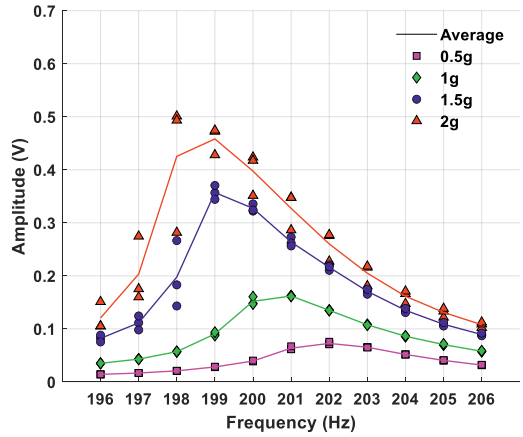

(a)

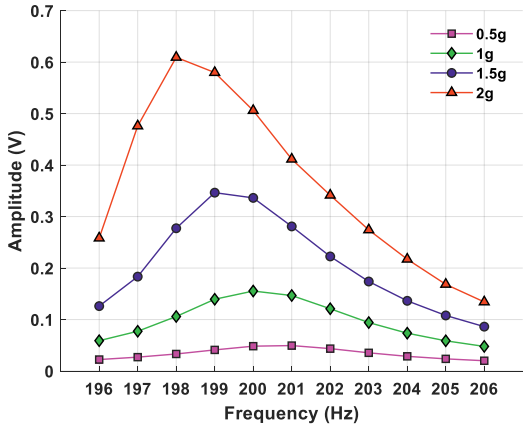

(b)

Figure 4.22 Measured (a) and simulated (b) open circuit voltages (rms) under varying vibration amplitudes from 0.5*g* to 2*g* [Publication IV].

markers, whereas the solid lines represent their average values. Slightly larger deviations can be seen near the resonant frequency for 1.5*g* and 2*g* cases. It was found that the tip displacement for the high acceleration values was quite large considering the size of the cantilever beam, making it difficult to stabilize near resonant frequency. Moreover, the resonant frequency was found to be sensitive to the slight displacement of the permanent magnets affecting the tip displacement and simulated voltage. In addition, the strength with which the cantilever beam is clamped affects the tip displacement.

The difference between the measured and simulated tip displacement was partly caused by the damping ratio, which was chosen to be frequency independent throughout the FE simulations. The damping ratio defines the beam

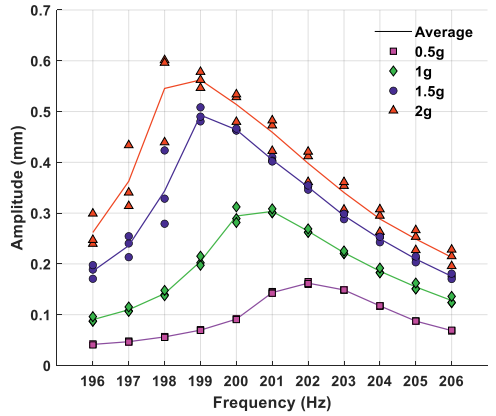

(a)

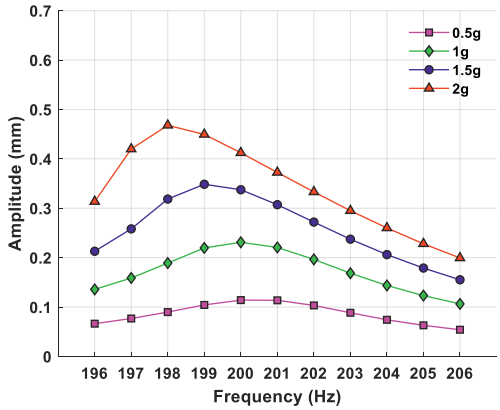

(b)

Figure 4.23 Measured (a) and simulated (b) tip displacements under varying vibration amplitudes from 0.5*g* to 2*g* [Publication IV].

stiffness and affects the tip displacement, which consequently affects the simulated voltage. The simulated voltage is also affected by the B_r of the permanent magnets, which was estimated from the measured magnetic field using a Hall probe. Furthermore, some inaccuracies in the model can be caused by neglecting the small airgaps between the caps and magnets, as well as the thickness of the glue between the aluminum and galfenol beams. Therefore, comparison between measured and simulated results must be done with the above-mentioned limitations in mind.

5 CONCLUSIONS

This thesis presents energy-based constitutive modeling and finite element analysis of magnetostrictive energy harvesters. This chapter concludes the thesis, provides a discussion and summary of the methods along with the obtained findings and presents the significance of the thesis and future work.

5.1 Summary of the methods and results

5.1.1 Experimental setup

This thesis emphasizes that repeatability of the measurements is crucial to provide a reliable comparison between measured and simulated results. For model validation, it is important to determine what proportion of the discrepancies occur due to measurement uncertainties and repeatability issues. The thesis advocates that the deviations in the experimental setup must be minimized to ensure the repeatability of the measurements. For the rod-type energy harvester, the output power was found to be quite sensitive to the vertical loading system and misalignments among the galfenol rod, iron core and magnets. Slight misalignment in the vertical loading system would change the applied stress in the middle of the galfenol rod. Furthermore, it was found that the loading device and all measuring devices should be warmed-up before carrying out experiments. A warm-up time of 40 minutes was provided to minimize the measurement discrepancies and improve repeatability. In addition, the measured results of the output voltage and current were taken as the average value of 10 consecutive readings. Friction was found to be another reason for introducing possible inaccuracies into the measured results. Lubrication was applied at the inner wall of the solid caps to minimize the friction between the contact points of the galfenol rod and solid caps. The output voltage and resonant frequency of the cantilever-beam-type energy harvester was found to be sensitive to the slight displacement of the permanent magnets and placement of the pick-up coil over

the beam. In addition, it was found that the clamping strength of the cantilever beam also affects the resonant frequency and causes slight deflection of the beam. To ensure repeatability, the magnets were glued and screwed firmly using PETG caps. Moreover, the experiments were carried out once the warm-up time of the shaker and laser displacement sensor had elapsed. All experiments for the rod-type energy harvester and cantilever-beam-type energy harvester were conducted three times to determine the repeatability, which has been discussed in Chapter 4.

5.1.2 Thermodynamic model

This thesis has shown that a directly-coupled thermodynamic magneto-mechanical model can analyze the magneto-mechanical behavior of the magnetostrictive energy harvesters. In Publication I, the energy-based constitutive model was implemented in a 2D axisymmetric FE model using in-house code in MATLAB to analyze a rod-type galfenol-based energy harvester. The thermodynamic model was able to determine the effect of mechanical preload, dynamic load, and load resistance upon harvester output power validating the suitability of the modeling approach. In Publication II, the effect of change in the preload and magnetic field bias upon the harvested output power was exploited while keeping the dynamic load and load resistance constant. The constitutive equations of the thermodynamic model were implemented in COMSOL Multiphysics for 3D FE analysis of the energy harvester. The modeling approach was validated by comparing the simulated and measured results obtained from a slightly modified rod-type harvester geometry.

In Publication IV, the thermodynamic model was tested on a cantilever-beam-type harvester geometry to determine the capability of the model to analyze different geometries of the energy harvester. The influence of the amplitude of vibrational acceleration and magnetostriction upon resonant frequency, and consequently the output voltage was analyzed. The model was validated against the measured results obtained from the prototype cantilever-beam-type energy harvester. The comparison among measured and simulated results from Publications I, II and IV evidenced that the thermodynamic model was able to reasonably predict the optimal operating conditions and could closely follow the measurement results. However, small discrepancies were observed between the measured and simulated results caused by model limitations and partly by measurement repeatability issues. It was observed that the thermodynamic model

was unable to properly fit to the measured magnetization curves for a wider range of mechanical preload. Furthermore, changing the degree of the polynomial energy expression influenced the fitting results. It was challenging to find a suitable degree of the polynomial energy expression and a suitable preload range that would result in the best fit. In addition, the remanence flux density of the permanent magnets utilized in the prototype harvester setups was measured using a Hall probe placed at the surface of the permanent magnet. Small discrepancies could potentially arise because the actual value of the remanence flux density was not known from the material properties and had to be tuned for the models. In addition, the magnetization properties of the core material were not known, so built-in material properties were utilized for the core material from the COMSOL library. Furthermore, the small airgaps between the contact surfaces of the rod-type and cantilever-beam-type prototype energy harvesters were not modeled. It was difficult to properly measure the airgaps between the core, solid caps, galfenol sample and magnets. Moreover, the airgaps might change due to continuous vibrations, which would mean that it was not possible to tune the airgaps to match the measured results due to practical design considerations, so it was not attempted.

5.1.3 Equivalent stress model

This thesis has shown that the equivalent stress modeling approach can be utilized for analyzing the magnetostrictive energy harvester. The model was implemented in COMSOL for 3D FE analysis of the energy harvester. The model was able to correctly predict the permeability of the galfenol material from the stress dependent measured magnetization curves. A direct comparison between two different modeling approaches was also presented. Unlike the thermodynamic modeling approach, the equivalent stress model was simple to implement since there were no free parameters that would require fitting to the measured magnetization curves. However, the limitation was that the model does not take into account the stress caused by magnetostriction, and therefore the total computed stress is less than the actual stress. In addition, the output power was found to be quite sensitive to the applied magnetic field bias. A slight change in the magnetic field bias would change the optimal preload value yielding maximum output power. Therefore, magnetic field bias had to be tuned once to provide a reasonable comparison between simulated and measured results.

5.2 Significance of the thesis and conclusions

In summary, this thesis validates the suitability of two existing magneto-mechanical constitutive models to analyze magnetostrictive energy harvesting devices. The magneto-mechanical models were able to analyze the influence of operating conditions (static mechanical preload, dynamic load, excitation frequency and magnetic field bias) and design characteristic (device geometry, load resistance, and coil parameters) on the performance of the energy harvester. The thermodynamic magneto-mechanical model has been utilized for the first time to analyze magnetostrictive energy harvesters. Compared to some earlier modeling approaches, the thermodynamic model has been tested on both rod-type and cantilever-beam-type harvester geometries to validate the suitability of the modeling approach to analyze different geometric configurations. The model was able to successfully predict the output power under varying preload, dynamic load, and load resistance values. The comparison among measured and simulated results showed that there does indeed exists optimal values of preload, dynamic load, and load resistance yielding maximum output power. Furthermore, the model was able to reasonably follow the measured results determining the influence of change in the magnetic field bias over mechanical preload. The influence of magnetostriction on resonant frequency of the cantilever beam has been shown. The thermodynamic model was able to accurately predict the change in the resonant frequency, both with and without magnetostriction.

The equivalent stress model has been utilized for the first time to analyze the magnetostrictive energy harvester. The model was able to reasonably determine the influence of magnetic bias over mechanical preload. The thesis also demonstrated successful implementation of the custom constitutive models in COMSOL by overriding the built-in electromagnetic and mechanical constitutive model. In Publications II and III, the remanence flux density was tuned for a single preload value to provide the correct magnetic field bias to the model. However, no further tuning was carried out for the individual preload values. From the engineering design point of view, this should not be a major problem. If the magnetic field bias of the manufactured energy harvester differs from the design value estimated by the model, the mechanical preload can be adjusted slightly such that the operating point shifts yielding maximum output power. Furthermore, the thesis has discussed the issues related to repeatability of the measurements and limitations of the model causing discrepancies between measured and simulated results. It was concluded that the comparison must be

done with the limitations of the model and repeatability of the measurements in mind. The results obtained from Publications I–IV showed that the thermodynamic magneto-mechanical model and equivalent stress model are suitable to be utilized as a tool to analyze magnetostrictive energy harvesters. The knowledge provided by the models could be utilized to tune the operating conditions and design characteristics for the development of the magnetostrictive energy harvesters.

5.3 Suggestions for future work

In this thesis, the output power was measured across a load resistance and the energy management circuit has not been tested. In a real scenario, however, the output from the energy harvester cannot be directly fed to the load (sensors or RF tags, etc.). An energy management circuit is needed to first capture the energy from the harvester, perform signal conditioning and store that into an energy accumulator. Future work should involve testing the energy management circuits and determine the efficiency of the energy conversion from harvester to the actual load. Furthermore, purely sinusoidal mechanical vibrations were utilized for testing the energy harvesters and validating the models. In reality, ambient vibrations are stochastic in nature, having random amplitudes and frequencies. Future work could involve gathering the actual vibrations data obtained from sources such as rail tracks, airplane wings or rotating machines. Furthermore, other giant magnetostrictive materials could be tested to determine the validity of the models to analyze energy harvesters utilizing different magnetostrictive materials.

REFERENCES

[1] Joule, J.P., 1847. XVII. On the effects of magnetism upon the dimensions of iron and steel bars. *The London, Edinburgh, and Dublin Philosophical Magazine and Journal of Science*, *30*(199), pp. 76–87.

[2] Dapino, M.J., 2004. On magnetostrictive materials and their use in adaptive structures. *Structural Engineering and Mechanics*, *17*(3–4), pp. 303–330.

[3] Clark, A.E., 1980. Magnetostrictive rare earth-Fe2 compounds. *Handbook of ferromagnetic materials*, *1*, pp. 531–589.

[4] Hathaway, K.B. and Clark, A.E., 1993. Magnetostrictive materials. *MRS Bulletin*, 18(4), pp. 34–41.

[5] Clark, A.E., Wun-Fogle, M., Restorff, J.B. and Lograsso, T.A., 2002. Magnetostrictive properties of Galfenol alloys under compressive stress. *Materials Transactions*, *43*(5), pp. 881–886.

[6] V. Berbyuk, Vibration energy harvesting using Galfenol-based transducer, Active and Passive Smart Structures and Integrated Systems 2013, International Society for Optics and Photonics, 2013, p. 86881F.

[7] Atulasimha, J. and Flatau, A.B., 2011. A review of magnetostrictive iron–gallium alloys. *Smart Materials and Structures*, *20*(4), p.043001.

[8] Wang, N.J., Liu, Y., Zhang, H.W., Chen, X. and Li, Y.X., 2016. Fabrication, magnetostriction properties and applications of Tb-Dy-Fe alloys: a review. *China Foundry*, *13*(2), pp. 75–84.

[9] Kellogg, R. and Flatau, A., 2008. Experimental investigation of Terfenol-D's elastic modulus. *Journal of Intelligent Material Systems and Structures*, *19*(5), pp. 583–595.

[10] Bowen, C.R., Kim, H.A., Weaver, P.M. and Dunn, S., 2014. Piezoelectric and ferroelectric materials and structures for energy harvesting applications. *Energy & Environmental Science*, *7*(1), pp. 25–44.

[11] Sudevalayam, S. and Kulkarni, P., 2010. Energy harvesting sensor nodes: Survey and implications. *IEEE Communications Surveys & Tutorials*, *13*(3), pp. 443–461.

[12] Niyato, D., Hossain, E., Rashid, M.M. and Bhargava, V.K., 2007. Wireless sensor networks with energy harvesting technologies: A game-theoretic

approach to optimal energy management. *IEEE Wireless Communications*, *14*(4), pp. 90–96.

[13] Shaikh, F.K. and Zeadally, S., 2016. Energy harvesting in wireless sensor networks: A comprehensive review. *Renewable and Sustainable Energy Reviews*, *55*, pp. 1041–1054.

[14] Akbari, S., 2014, September. Energy harvesting for wireless sensor networks review. In *2014 Federated Conference on Computer Science and Information Systems* (pp. 987–992). IEEE.

[15] Mitcheson, P.D., Yeatman, E.M., Rao, G.K., Holmes, A.S. and Green, T.C., 2008. Energy harvesting from human and machine motion for wireless electronic devices. *Proceedings of the IEEE*, *96*(9), pp. 1457–1486.

[16] Vullers, R.J., Van Schaijk, R., Visser, H.J., Penders, J. and Van Hoof, C., 2010. Energy harvesting for autonomous wireless sensor networks. *IEEE Solid-State Circuits Magazine*, *2*(2), pp. 29–38.

[17] Gavrila, H. and Ionita, V., 2002. Crystalline and amorphous soft magnetic materials and their applications- status of art and challenges. *Journal of Optoelectronics and Advanced Materials(Romania)*, *4*(2), pp. 173–192.

[18] Siang, J., Lim, M.H. and Salman Leong, M., 2018. Review of vibration-based energy harvesting technology: Mechanism and architectural approach. *International Journal of Energy Research*, *42*(5), pp. 1866–1893.

[19] Wei, C. and Jing, X., 2017. A comprehensive review on vibration energy harvesting: Modeling and realization. *Renewable and Sustainable Energy Reviews*, *74*, pp. 1–18.

[20] Meninger, S., Mur-Miranda, J.O., Amirtharajah, R., Chandrakasan, A. and Lang, J., 1999, August. Vibration-to-electric energy conversion. In *Proceedings of the 1999 international symposium on Low power electronics and design* (pp. 48–53).

[21] Reyer, M., Hurlebaus, S., Mander, J. and Ozbulut, O.E., 2011, November. Design of a wireless sensor network for structural health monitoring of bridges. In *2011 Fifth International Conference on Sensing Technology* (pp. 515–520). IEEE.

[22] Dumas, D., Lani, F., Monnier, T., Smaili, R. and Loyer, J., 2011, July. Damage detection in composite structures using autonomous wireless systems: simulation & validation. In *Journal of Physics: Conference Series* (Vol. 305, No. 1, p. 012084). IOP Publishing.

[23] White, N.M. and Zaghari, B., 2022. Energy Harvesting: An Overview of Techniques for Use Within the Transport Industry. *IEEE Electrical Insulation Magazine*, *38*(3), pp. 24–32.

[24] Wischke, M., Masur, M., Kröner, M. and Woias, P., 2011. Vibration harvesting in traffic tunnels to power wireless sensor nodes. *Smart Materials and Structures*, *20*(8), p.085014.

[25] Cleamnte, V.G., Brennan, M.J., Gatti, G. and Thompson, D.J., 2016, September. Energy harvesting from the vibrations of a passing train: effect of speed variability. In *Journal of Physics: Conference Series* (Vol. 744, No. 1, p. 012080). IOP Publishing.

[26] Cai, Q. and Zhu, S., 2021. The nexus between vibration-based energy harvesting and structural vibration control: A comprehensive review. *Renewable and Sustainable Energy Reviews*, p.111920.

[27] Paradiso, J.A. and Starner, T., 2005. Energy scavenging for mobile and wireless electronics. *IEEE Pervasive Computing*, *4*(1), pp. 18–27.

[28] Ueno, T., 2019. Magnetostrictive vibrational power generator for battery-free IoT application. *AIP Advances*, *9*(3), p.035018.

[29] Kausar, A.Z., Reza, A.W., Saleh, M.U. and Ramiah, H., 2014. Energizing wireless sensor networks by energy harvesting systems: Scopes, challenges and approaches. *Renewable and Sustainable Energy Reviews*, *38*, pp. 973–989.

[30] Dagdeviren, C., Li, Z. and Wang, Z.L., 2017. Energy harvesting from the animal/human body for self-powered electronics. *Annu. Rev. Biomed. Eng*, *19*(1), pp. 85–108.

[31] Sezer, N. and Koç, M., 2021. A comprehensive review on the state-of-the-art of piezoelectric energy harvesting. *Nano Energy*, *80*, p.105567.

[32] Zhang, T., Jiang, C., Zhang, H. and Xu, H., 2004. Giant magnetostrictive actuators for active vibration control. *Smart Materials and Structures*, *13*(3), p.473.

[33] Avvari, P.V., Yang, Y. and Soh, C.K., 2017. Long-term fatigue behavior of a cantilever piezoelectric energy harvester. *Journal of Intelligent Material Systems and Structures*, *28*(9), pp. 1188–1210.

[34] Iqbal, M., Nauman, M.M., Khan, F.U., Abas, P.E., Cheok, Q., Iqbal, A. and Aissa, B., 2021. Vibration-based piezoelectric, electromagnetic, and hybrid energy harvesters for microsystems applications: A contributed review. *International Journal of Energy Research*, *45*(1), pp. 65–102.

[35] Uchino, K. ed., 2017. Advanced piezoelectric materials: Science and technology. Woodhead Publishing.

[36] Zhang, Q., Wang, Y. and Kim, E.S., 2015. Electromagnetic energy harvester with flexible coils and magnetic spring for 1–10 Hz resonance. *Journal of Microelectromechanical Systems*, *24*(4), pp. 1193–1206.

[37] Davino, D., Krejčí, P. and Visone, C., 2013. Fully coupled modeling of magneto-mechanical hysteresis through 'thermodynamic' compatibility. *Smart Materials and Structures*, *22*(9), p.095009.

[38] Clemente, C.S., Mahgoub, A., Davino, D. and Visone, C., 2017. Multiphysics circuit of a magnetostrictive energy harvesting device. *Journal of Intelligent Material Systems and Structures*, *28*(17), pp. 2317–2330.

[39] Adly, A., Davino, D., Giustiniani, A. and Visone, C., 2010. Experimental tests of a magnetostrictive energy harvesting device toward its modeling. *Journal of Applied Physics*, *107*(9), p.09A935.

[40] Viola, A., Franzitta, V., Cipriani, G., Di Dio, V., Raimondi, F.M. and Trapanese, M., 2015. A magnetostrictive electric power generator for energy harvesting from traffic: Design and experimental verification. *IEEE Transactions on Magnetics*, *51*(11), pp. 1–4.

[41] Zucca, M., Hadadian, A. and Bottauscio, O., 2015. Quantities affecting the behavior of vibrational magnetostrictive transducers. *IEEE Transactions on Magnetics*, *51*(1), pp. 1–4.

[42] Palumbo, S., Rasilo, P. and Zucca, M., 2019. Experimental investigation on a Fe-Ga close yoke vibrational harvester by matching magnetic and mechanical biases. *Journal of Magnetism and Magnetic Materials*, *469*, pp. 354–363.

[43] Fang, Z.W., Zhang, Y.W., Li, X., Ding, H. and Chen, L.Q., 2017. Integration of a nonlinear energy sink and a giant magnetostrictive energy harvester. *Journal of Sound and Vibration*, *391*, pp. 35–49.

[44] Berbyuk, V., 2013, April. Vibration energy harvesting using Galfenol-based transducer. In *Active and Passive Smart Structures and Integrated Systems 2013* (Vol. 8688, pp. 429–440). SPIE.

[45] Kita, S., Ueno, T. and Yamada, S., 2015. Improvement of force factor of magnetostrictive vibration power generator for high efficiency. *Journal of Applied Physics*, *117*(17), p.17B508.

[46] Cao, S., Yang, S., Zheng, J., Zhang, L. and Wang, B., 2016. An equivalent circuit model and energy extraction technique of a magnetostrictive energy harvester. *IEEE Transactions on Applied Superconductivity*, *26*(4), pp. 1–6.

[47] Deng, Z. and Dapino, M.J., 2017. Influence of electrical impedance and mechanical bistability on Galfenol-based unimorph harvesters. *Journal of Intelligent Material Systems and Structures*, *28*(3), pp. 421–431.

[48] Yang, Z., Tan, Y. and Zu, J., 2017. A multi-impact frequency up-converted magnetostrictive transducer for harvesting energy from finger tapping. *International Journal of Mechanical Sciences*, *126*, pp. 235–241.

[49] Yoo, J.H. and Flatau, A.B., 2012. A bending-mode Galfenol electric power harvester. *Journal of Intelligent Material Systems and Structures*, *23*(6), pp. 647–654.

[50] Cao, S., Zheng, J., Guo, Y., Li, Q., Sang, J., Wang, B. and Yan, R., 2015. Dynamic characteristics of Galfenol cantilever energy harvester. *IEEE Transactions on Magnetics*, *51*(3), pp. 1–4.

[51] Mori, K., Horibe, T., Ishikawa, S., Shindo, Y. and Narita, F., 2015. Characteristics of vibration energy harvesting using giant magnetostrictive cantilevers with resonant tuning. *Smart Materials and Structures*, *24*(12), p.125032.

[52] Ueno, T. and Yamada, S., 2011. Performance of energy harvester using iron–gallium alloy in free vibration. *IEEE Transactions on Magnetics*, *47*(10), pp. 2407–2409.

[53] Wun-Fogle, M., Restorff, J.B. and Clark, A.E., 2006. Magnetomechanical coupling in stress-annealed Fe–Ga (Galfenol) alloys. *IEEE Transactions on Magnetics*, *42*(10), pp. 3120–3122.

[54] Brooks, M., Summers, E., Restorff, J.B. and Wun-Fogle, M., 2012. Behavior of magnetic field–annealed Galfenol steel. *Journal of Applied Physics*, *111*(7), p.07A907.

[55] Preisach, F., 1935. Über die magnetische Nachwirkung. *Zeitschrift für physik*, *94*(5), pp. 277–302.

[56] Jiles, D.C. and Atherton, D.L., 1986. Theory of ferromagnetic hysteresis. *Journal of Magnetism and Magnetic Materials*, *61*(1–2), pp. 48–60.

[57] Bergqvist, A. and Engdahl, G., 1991. A stress-dependent magnetic Preisach hysteresis model. *IEEE Transactions on Magnetics*, *27*(6), pp. 4796–4798.

[58] Sablik, M.J. and Jiles, D.C., 1993. Coupled magnetoelastic theory of magnetic and magnetostrictive hysteresis. *IEEE Transactions on Magnetics*, *29*(4), pp. 2113–2123.

[59] Adly, A.A. and Mayergoyz, I.D., 1996. Magnetostriction simulation using anisotropic vector Preisach-type models. *IEEE Transactions on Magnetics*, *32*(5), pp. 4773–4775.

[60] Bottauscio, O., Lovisolo, A., Roccato, P.E., Zucca, M., Sasso, C. and Bonin, R., 2008. Modeling and experimental analysis of magnetostrictive devices: From the material characterization to their dynamic behavior. *IEEE Transactions on Magnetics*, *44*(11), pp. 3009–3012.

[61] Li, J. and Xu, M., 2011. Modified Jiles-Atherton-Sablik model for asymmetry in magnetomechanical effect under tensile and compressive stress. *Journal of Applied Physics*, *110*(6), p.063918.

[62] Zhou, H.M. and Zhou, Y.H., 2007. Vibration suppression of laminated composite beams using actuators of giant magnetostrictive materials. *Smart Materials and Structures*, *16*(1), p.198.

[63] Chakrabarti, S. and Dapino, M.J., 2012. Coupled axisymmetric finite element model of a hydraulically amplified magnetostrictive actuator for active powertrain mounts. *Finite Elements in Analysis and Design*, *60*, pp. 25–34.

[64] Evans, P.G. and Dapino, M.J., 2010. Efficient magnetic hysteresis model for field and stress application in magnetostrictive Galfenol. *Journal of Applied Physics*, *107*(6), p.063906.

[65] Dapino, M.J. and Chakrabarti, S., 2013. Modeling of 3D Magnetostrictive Systems with Application to Galfenol and Terfenol-D Actuators. In *Advances in Science and Technology* (Vol. 77, pp. 11–28). Trans Tech Publications Ltd.

[66] Chakrabarti, S. and Dapino, M.J., 2012. Fully coupled discrete energy-averaged model for Terfenol-D. *Journal of Applied Physics*, *111*(5), p.054505.

[67] Tari, H., Scheidler, J.J. and Dapino, M.J., 2015. Robust solution procedure for the discrete energy-averaged model on the calculation of 3D hysteretic magnetization and magnetostriction of iron–gallium alloys. *Journal of Magnetism and Magnetic Materials*, *384*, pp. 266–275.

[68] Belahcen, A., Fonteyn, K., Hannukainen, A. and Kouhia, R., 2008, October. On numerical modeling of coupled magnetoelastic problem. In *Proc. 21st Nordic Seminar on Computational Mechanics* (pp. 203–206).

[69] Fonteyn, K., Belahcen, A., Kouhia, R., Rasilo, P. and Arkkio, A., 2010. FEM for directly coupled magneto-mechanical phenomena in electrical machines. *IEEE Transactions on Magnetics*, *46*(8), pp. 2923–2926.

[70] Aydin, U., Rasilo, P., Singh, D., Lehikoinen, A., Belahcen, A. and Arkkio, A., 2015. Coupled magneto-mechanical analysis of iron sheets under biaxial stress. *IEEE Transactions on Magnetics*, *52*(3), pp. 1–4.

[71] Rasilo, P., Singh, D., Aydin, U., Martin, F., Kouhia, R., Belahcen, A. and Arkkio, A., 2015. Modeling of hysteresis losses in ferromagnetic laminations under mechanical stress. *IEEE Transactions on Magnetics*, *52*(3), pp. 1–4.

[72] Rasilo, P., Singh, D., Jeronen, J., Aydin, U., Martin, F., Belahcen, A., Daniel, L. and Kouhia, R., 2019. Flexible identification procedure for thermodynamic constitutive models for magnetostrictive materials. *Proceedings of the Royal Society A*, *475*(2223), p. 20180280.

[73] Daniel, L. and Hubert, O., 2009. An equivalent stress for the influence of multiaxial stress on the magnetic behavior. *Journal of Applied Physics*, *105*(7), p. 07A313.

[74] Daniel, L. and Hubert, O., 2010. Equivalent stress criteria for the effect of stress on magnetic behavior. *IEEE Transactions on Magnetics*, *46*(8), pp. 3089–3092.

[75] Rekik, M., Daniel, L. and Hubert, O., 2014. Equivalent stress model for magnetic hysteresis losses under biaxial loading. *IEEE Transactions on Magnetics*, *50*(4), pp. 1–4.

[76] Daniel, L., Rekik, M. and Hubert, O., 2014. A multiscale model for magneto-elastic behaviour including hysteresis effects. *Archive of Applied Mechanics*, *84*(9), pp. 1307–1323.

[77] Daniel, L., Hubert, O. and Rekik, M., 2015. A simplified 3-D constitutive law for magneto-mechanical behavior. *IEEE Transactions on Magnetics*, *51*(3), pp. 1–4.

[78] Daniel, L., 2017. An equivalent strain approach for magneto-elastic couplings. *IEEE Transactions on Magnetics*, *53*(6), pp. 1–4.

[79] Mudivarthi, C., Datta, S., Atulasimha, J. and Flatau, A.B., 2008. A bidirectionally coupled magnetoelastic model and its validation using a Galfenol unimorph sensor. *Smart Materials and Structures*, *17*(3), p.035005.

[80] Graham, F.C., Mudivarthi, C., Datta, S. and Flatau, A.B., 2009. Modeling of a Galfenol transducer using the bidirectionally coupled magnetoelastic model. *Smart Materials and Structures*, *18*(10), p.104013.

[81] Shi, P., 2020. Magneto-mechanical model of ferromagnetic material under a constant weak magnetic field via analytical anhysteresis solution. *Journal of Applied Physics*, *128*(11), p.115102.

[82] Zhao, X. and Lord, D.G., 2006. Application of the Villari effect to electric power harvesting. *Journal of Applied Physics*, 99(8), p.08M703.

[83] Rezaeealam, B., 2012. Finite element analysis of magnetostrictive vibration energy harvester. COMPEL – *The International Journal for Computation and Mathematics in Electrical and Electronic Engineering*.

[84] Davino, D., Krejčí, P., Pimenov, A., Rachinskii, D. and Visone, C., 2016. Analysis of an operator-differential model for magnetostrictive energy harvesting. *Communications in Nonlinear Science and Numerical Simulation*, 39, pp. 504–519.

[85] Liu, H., Cong, C., Zhao, Q. and Ma, K., 2019. Comprehensive analysis of the energy harvesting performance of a fe-ga based cantilever harvester in free excitation and base excitation mode. *Sensors*, 19(15), p. 3412.

[86] Cao, S., Liu, L., Zheng, J., Pan, R. and Song, G., 2019. Modeling and analysis of Galfenol nonlinear cantilever energy harvester with elastic magnifier. IEEE Transactions on Magnetics, 55(6), pp. 1–5.

[87] Meng, A., Yan, C., Li, M., Pan, W., Yang, J. and Wu, S., 2020. Modeling and experiments on Galfenol energy harvester. *Acta Mechanica Sinica*, 36(3), pp. 635–643.

[88] Clemente, C.S. and Davino, D., 2019. Modeling and characterization of a kinetic energy harvesting device based on Galfenol. *Materials*, *12*(19), p. 3199.

[89] Clemente, C.S., Davino, D. and Loschiavo, V.P., 2021. Analysis of a Magnetostrictive Harvester With a Fully Coupled Nonlinear FEM Modeling. *IEEE Transactions on Magnetics*, *57*(6), pp. 1–4.

[90] Zucca, M., Mei, P., Ferrara, E. and Fiorillo, F., 2017. Sensing dynamic forces by fe–ga in compression. *IEEE Transactions on Magnetics*, *53*(11), pp. 1–4.

[91] Datasheet. TdVib LLC by EXTREMA Products. URL: http://www.tdvib.com/wp-content/uploads/2015/09/Terfenol-D-Magnetic-Flux-Density.png

[92] Datasheet. TdVib LLC by EXTREMA Products, Summers, E., 2015. Galfenol – A New Class of Magnetostrictive Materials. Galfenol Public Release, 7.

[93] Bala, H., Trepak, N.M., Szymura, S., Lukin, A.A., Gaudyn, V.A., Isaicheva, L.A., Pawłowska, G. and Ilina, L.A., 2001. Corrosion protection of Nd–Fe–B type permanent magnets by zinc phosphate surface conversion coatings. *Intermetallics*, 9(6), pp. 515–519.

[94] Zhou, Q. and Liu, S., 2021. Fabrication of Magnesium Phosphate Coating by Electrochemical Cathodic Method for Corrosion Protection of Sintered NdFeB Magnets. *Journal of Materials Engineering and Performance*, *30*(2), pp. 1200–1206.

[95] Ahmad, K.A., Drummond, J.L., Graber, T. and BeGole, E., 2006. Magnetic strength and corrosion of rare earth magnets. *American Journal of Orthodontics and Dentofacial Orthopedics*, *130*(3), pp. 275–e11.

[96] Deng, Z. and Dapino, M.J., 2015, April. Multiphysics modeling and design of Galfenol-based unimorph harvesters. In *Industrial and Commercial Applications of Smart Structures Technologies 2015* (Vol. 9433, pp. 74–83). SPIE.

[97] Löffler, M., Kremer, R., Sutor, A. and Lerch, R., 2015. Hysteresis of the resonance frequency of magnetostrictive bending cantilevers. *Journal of Applied Physics*, *117*(17), p.17A907

[98] Daniel, L. and Hubert, O., 2009. An analytical model for the ΔE effect in magnetic materials. *The European Physical Journal – Applied Physics*, *45*(3).

PUBLICATION ERRATA

Publication I

The polynomial coefficient $\alpha_2 = -1.208 \times 104$ J/m^3 presented in Table 1 of Section 4.2 is incorrect. The correct value of the polynomial coefficient is $\alpha_2 = -1.028 \times 10^4$ J/m^3.

The stress range of 40–80 MPa in Section 4.1 is incorrect. The stress range of 40–70 MPa was utilized to obtain the coefficient of model parameters presented in Table 1 of Section 4.2.

Publication IV

To compute the resonant frequency of 200 Hz, the measured time of 200 ms over $n = 8$ consecutive periods mentioned in Section 4.2, paragraph 2 is incorrect. Instead, it should be 40 ms over $n = 8$ consecutive periods. The correct value of the measured time is also mentioned in Fig. 5 of the Publication IV.

PUBLICATIONS

PUBLICATION I

Finite Element Analysis of Magnetostrictive Energy Harvesting Concept Device Utilizing Thermodynamic Magneto-Mechanical Model

U. Ahmed, J. Jeronen, M. Zucca, S. Palumbo and P. Rasilo

Journal of Magnetism and Magnetic Materials 486 (2019)
DOI: 10.1016/j.jmmm.2019.165275

Journal of Magnetism and Magnetic Materials 486 (2019) 165275

Contents lists available at ScienceDirect

Journal of Magnetism and Magnetic Materials

journal homepage: www.elsevier.com/locate/jmmm

Research articles

Finite element analysis of magnetostrictive energy harvesting concept device utilizing thermodynamic magneto-mechanical model

U. Ahmed[a,*], J. Jeronen[a], M. Zucca[b], S. Palumbo[b,c], P. Rasilo[a]

[a] Tampere University, Electrical Engineering, P.O. Box 692, FI-33720 Tampere, Finland
[b] Istituto Nazionale di Ricerca Metrologica, INRIM, Metrology for Quality of Life Dept, Strada delle Cacce 91, Torino, Italy
[c] Politecnico di Torino, Dipartimento di Elettronica e Telecomunicazioni, Corso Duca degli Abruzzi 24, Torino, Italy

ARTICLE INFO

Keywords:
Energy harvesting
Finite element analysis
Helmholtz free energy
Magneto-elasticity
Magnetostrictive devices

ABSTRACT

This paper utilizes a thermodynamic approach based on Helmholtz free energy density and a finite element (FE) model to analyze a galfenol-based magnetostrictive energy harvesting concept device. An analytical energy density function is first presented assuming an isotropic material for the identification of a magneto-mechanical constitutive law. The model utilizes the magnetic flux density and mechanical strain as state variables. Compared to some earlier approaches, this simplifies the implementation of FE models based on magnetic vector potential and mechanical displacement, since time-consuming inversion of the constitutive law is not required. The Maxwell and mechanical balance equations are then solved utilizing the constitutive law in an axisymmetric FE model. A prototype device is developed and tested under uniaxial cyclic compressive loading of 100 Hz at different preload and dynamic loading cases. Finally, the results from the simulations are compared with the experimental results for validation. The comparison shows that the analytical constitutive model fits well to the magnetization curves measured under static loading. Furthermore, the FE model closely predicts the measured power with some discrepancies under different preload values. The model is able to predict the behavior of the device with respect to preload, load resistance and magnetization of the sample, proving to be an effective tool in the design of such devices.

1. Introduction

Magneto-mechanical energy harvesting based on giant magnetostrictive materials (GMMs), e.g. galfenol, Terfenol-D and Metglas, has received increased attention during the past few years, allowing maintenance and battery-free applications. GMMs offer large magnetostrains, strong magneto-mechanical coupling and high operational frequency bandwidth as compared to iron and other ferromagnetic alloys such as nickel and cobalt [1]. The discovery of GMMs has offered their successful incorporation as an active material in various applications including active vibration control, torque sensors and transducers as well as energy harvesters for structural condition monitoring [1,2]. Mechanical kinetic energy harvesters utilize ambient vibration sources otherwise wasted, originating from, long span bridges, skyscrapers and machines with rotating parts among others, to power up small-scale wireless sensors and transducers.

The effect of magnetostriction is defined as a change in the length or shape of the magnetostrictive material upon magnetization. This phenomenon induces strain in the material which is due to the fact that randomly aligned magnetic domains tend to align themselves in the direction parallel to the applied magnetic field [3]. The energy harvesters utilize the inverse magnetostrictive effect, which implies change in the magnetic permeability of the material upon mechanical stress, also known as the Villari effect [4]. The application of mechanical vibrations causes bulk changes in the magnetization of the material due to the rotation of the magnetic domains and domain wall motion [5]. Among giant magnetostrictive materials, galfenol is considered more suitable for energy harvesting applications as compared to Terfenol-D. The characteristics of galfenol include strong magneto-elastic coupling, ductile nature, low hysteresis losses, moderate magnetostriction (~250–350 ppm) at low magnetic fields (~10 kA/m) and high tensile strength (~500 MPa). In addition, due to its steel-like structural properties, galfenol can be welded, rolled and machined easily. On the other hand, Terfenol-D shows large magnetostriction (~1200–1600 ppm) at a high saturation magnetization (~160 kA/m), but it is quite brittle in nature having low tensile stress and poor machinability [6].

Moreover, the magnetostrictive properties of galfenol have been

* Corresponding author.
E-mail address: umair.ahmed@tuni.fi (U. Ahmed).

https://doi.org/10.1016/j.jmmm.2019.165275
Received 28 January 2019; Received in revised form 21 March 2019; Accepted 3 May 2019
Available online 06 May 2019
0304-8853/

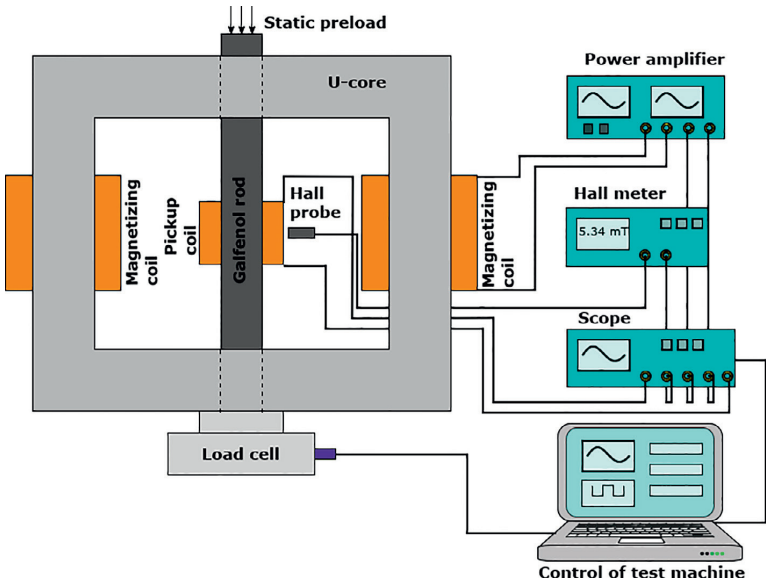

Fig. 1. Schematic diagram of the measurement system for the characterization of the magnetostrictive material.

analyzed in Refs. [7–10]. Galfenol offers a strong coupling coefficient as compared to Terfenol-D [7] and demonstrates large magnetostriction at a wide range of temperatures, showing weak temperature dependence [8]. Stress annealing changes the magnetostriction of galfenol and full magnetostriction can be achieved even at zero prestress [9]. The effect of change in Young's modulus ΔE is studied in Ref. [10] by applying a static compressive load from 0.5 to 63.3 MPa. In addition, the results from Ref. [11] show that under no applied bias, the Young's modulus varies between 72 and 78 GPa when the compressive stress ranges from 15 to 60 MPa.

Modeling tools are required to investigate the coupled magneto-mechanical effects for a magnetostrictive energy harvester. Furthermore, to optimize the design characteristics of the harvester, modeling tools determine the appropriate design characteristics and operating conditions in order to obtain maximum output power and higher efficiency. The design characteristic includes determining the geometry of the harvester, mechanical preload, amplitude and frequency of mechanical vibrations and magnetic bias. Moreover, the design parameters of the harvester are governed by the available mechanical excitation and are influenced by the physical dimensions, emphasing the need to develop a model enabling efficient design.

Various models have been developed analyzing coupled magneto-mechanical behavior under uniaxial and multiaxial loading cases [12–14]. An axisymmetric finite element model based on Maxwell's and Navier's equations coupled using nonlinear magnetomechanical constitutive laws is discussed in Ref. [13]. A Helmholtz free energy density based magneto-mechanical model utilizing thermodynamic approach has been proposed in [14]. The former utilizes the magnetic field and stress as the state variables, which requires numerically inverting the constitutive model when using it in finite element (FE) formulations based on the magnetic vector potential and mechanical displacement. On the other hand, the latter utilizes magnetic flux density and strain as state variables, and can be directly applied in FE tools. In addition, a magnetic hysteresis model due to applied bias and mechanical stress is presented in Ref. [15]. The model is based on analytical expressions for domain rotation, accurately describing the non-linear magnetization vs. field and strain vs. stress behavior in the dominant domain rotation regions. However, the models presented in Refs. [12,14,15] have not yet been applied for analyzing prototype magneto-mechanical transducers to be employed for harvesting energy.

Fully coupled nonlinear magneto-elastic models for magnetostrictive transducers are presented in Refs. [16–18]. Taking into account the nonlinear and dynamic behavior of magnetostrictive materials, the approach in [16] utilizes the Armstrong model representing an energy-based magneto-mechanical constitutive law, whereas [17] presents a class of phenomenological models for magneto-elastic interactions in materials with losses due to hysteresis. The model in Ref. [18] is based on constitutive equations resembling piezoelectricity. Models analyzing a magnetostrictive energy harvesting concept device are presented in Refs. [19–21]. A Preisach based phenomenological model for the analysis of optimization problems for harvesters is presented in Ref. [19]. A Gibbs free energy based fully coupled model for analyzing a magnetostrictive energy harvester concept device is discussed in Ref. [20]. The approach utilizes a three port equivalent circuit model related to mechanical, magnetic and electrical parts of a concept energy harvester, to be implemented in circuit simulation software.

In this paper, we apply a thermodynamic free energy density approach presented in Ref. [14] to analyze a galfenol-based magnetostrictive energy-harvesting concept device for the first time. The loss due to hysteresis for galfenol is small [21] and thus excluded from the analysis. We first present an analytical energy density function for expressing the coupled magneto-mechanical constitutive law. The model parameters are then determined by fitting the analytical energy density function against measured magnetization curves. The Maxwell and mechanical balance equations are solved utilizing the constitutive law in an axisymmetric FE model. Finally, measurements from a prototype energy harvesting concept device are compared with the simulated results to validate the model.

2. Experimental setup and working principle

2.1. Material characterization

First, the characterization of the galfenol rod ($Fe_{81.6}Ga_{18.4}$) used in the prototype concept device was carried out for identifying the constitutive law. The schematic diagram of the experimental setup for the

characterization of the material is presented in Fig. 1. The key components of the setup include the galfenol rod, magnetizing coils, a U-shaped magnetic core, a Hall probe and a prestress mechanism. The galfenol rod has a length of 60 mm with a diameter of 12 mm. The overall dimensions of the U-shaped magnetic core are 120 mm × 68 mm × 15 mm. The magnetizing coils are connected in series, consist of 600 turns, and are able to supply current up to 6 A through a power amplifier.

A static axial compressive prestress (preload) σ was first applied using a high performance test machine (Instron ElectroPuls E10000) in force control mode. The galfenol rod was then magnetized by supplying a 200 mHz AC voltage to the magnetizing coils using a signal generator and a power amplifier. The longitudinal strain ε was measured using an extensometer clamped in the middle of the sample. Finally, the magnetic field strength H was measured by a Hall probe placed in contact with the middle part of the sample and the average flux density B was obtained by integrating the induced voltage from the pickup coil wound around the active material. The measured magnetization and magnetostriction curves were obtained at different compressive preload values ranging from 0 to 80 MPa.

2.2. Energy harvester

The schematic diagram for the prototype harvester concept device is presented in Fig. 2 (right). The device consists of a galfenol rod utilized as an active material and two permanent magnets. The galfenol rod is machined as shown in the Fig. 2 (left) with a diameter of 6 mm in the middle and 12 mm from both ends to accommodate the pickup coil. The pickup coil consists of 2000 turns wound from 0.2 mm thick copper wire. The actual experimental setup is presented in Fig. 3 whereas, the geometry and FE mesh of the prototype harvester device used in the axisymmetric magneto-mechanical FE model are presented in Fig. 4. The markers in Fig. 4 denote the nodes where the axial force is applied. The regions marked as H_{air} and H_{bar} are used for computing the magnetic field in the air and inside the galfenol bar based on the FE solution. This is further discussed in Sections 3.2 and 4.2.

A constant magnetic bias is applied using two NdFeB magnets having a remanence flux density $B_r = 1.13$ T and coercive field $H_c = 955$ kA/m with physical dimensions of 6 mm in thickness and 12 mm in diameter. The magnets are attached at both ends of the galfenol rod and the axial load is applied through the magnets as shown in Fig. 2. The NdFeB magnets are coated with a phosphate coating. This is the treatment for the magnets used in actuators, which is particularly suitable to protect magnets from the effects of mechanical stress. After an intense stress, the properties of the magnets remain unaltered, provided that the stress is applied gradually, as it occurs in the compression machine. A dynamic compressive stress is applied on the bar in the axial direction using a force actuator, which is capable of providing a static offset force (preload) and a sinusoidal vibrational force up to 100 Hz frequency and 10 kN in amplitude.

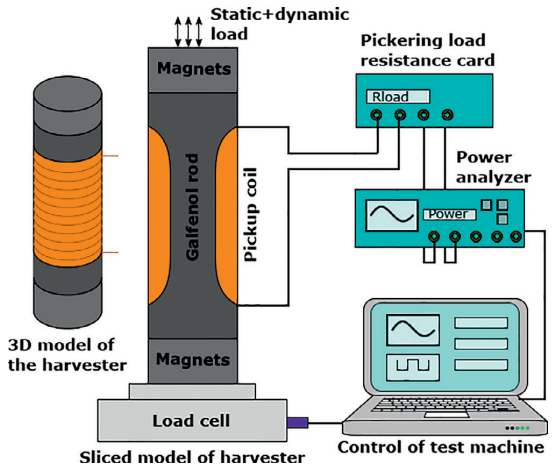

Fig. 2. Schematic diagram of the measurement system for the concept energy harvester and internal structure of the concept device (sliced model).

The vibrational force is measured by a load cell with an expanded uncertainty $\leq 0.5\%$. The harvester is first subjected to a static preload followed by a dynamic load at three different amplitudes (4, 6 and 8 MPa). The dynamic load is applied at a frequency of 100 Hz. The experimental procedure is then repeated for different preload values ranging from 40 to 80 MPa with an increment of 5 MPa. The voltage induced into the pickup coil as a result of the Villari effect and Faraday's law is measured using a precision power analyzer (Yokogawa WT3000). A Pickering programmable precision resistor (1%) card PXI 40-297-002, controlled by LabVIEW software, measures the output power. The programmable load resistance is varied to determine the maximum output power from the prototype concept device at different preload and dynamic load values. In this study, we analyze the effect of preload and dynamic load on the harvester, keeping the magnetic bias constant.

3. Models

3.1. Constitutive model

The energy harvester is modeled using a thermodynamic approach based on the Helmholtz free energy density function $\psi(\boldsymbol{B}, \boldsymbol{\varepsilon})$ presented in Ref. [14], where the state variables are the magnetic flux density vector $\boldsymbol{B}$ and the strain tensor $\boldsymbol{\varepsilon}$. The total strain $\boldsymbol{\varepsilon} = \boldsymbol{C}^{-1}\boldsymbol{\sigma} + \boldsymbol{\lambda}$ includes both the mechanical strain $\boldsymbol{C}^{-1}\boldsymbol{\sigma}$ and the strain caused by magnetostriction $\boldsymbol{\lambda}$, where $\boldsymbol{C}$ is the mechanical stiffness matrix and $\boldsymbol{\sigma}$ the stress. The state variables can be written in terms of six scalar invariants as

$$I_1 = \operatorname{tr}\boldsymbol{\varepsilon},\ I_2 = \operatorname{tr}\boldsymbol{\varepsilon}^2,\ I_3 = \operatorname{tr}\boldsymbol{\varepsilon}^3,$$
$$I_4 = \frac{\boldsymbol{B}\cdot\boldsymbol{B}}{B_{\text{ref}}^2},\ I_5 = \frac{\boldsymbol{B}\cdot\boldsymbol{\varepsilon}\boldsymbol{B}}{B_{\text{ref}}^2},\ I_6 = \frac{\boldsymbol{B}\cdot\boldsymbol{\varepsilon}^2\boldsymbol{B}}{B_{\text{ref}}^2}, \tag{1}$$

where tr denotes the trace of a tensor, $\boldsymbol{e}$ represents the deviatoric strain given by $\boldsymbol{e} = \boldsymbol{\varepsilon} - \frac{1}{3}(\operatorname{tr}\boldsymbol{\varepsilon})\boldsymbol{I}$, and $\boldsymbol{I}$ is the second-order identity tensor. $B_{\text{ref}} = 1$ T is only used for scaling purposes to make the invariants dimensionless. The Helmholtz free energy density, describing the magneto-mechanical interaction in the actuator material, is then written as

$$\psi = \frac{1}{2}\lambda I_1^2 + \mu I_2 + \sum_{i=1}^{n_\alpha}\alpha_i I_4^i + \sum_{i=1}^{n_\beta}\beta_i I_5^i + \sum_{i=1}^{n_\gamma}\gamma_i I_6^i, \tag{2}$$

where the polynomial coefficients α_i, β_i and γ_i are parameters fitted against the B-H curves obtained from the characterization measurements discussed in Section 2.1, and λ and μ are the Lamé parameters obtained from Young's modulus and Poisson's ratio for an isotropic material. The first two invariants I_1 and I_2 are related to pure mechanical behavior. The invariant I_3 is not utilized considering linear elastic behavior. I_4 is related to purely magnetic behavior, whereas I_5 and I_6 describe the magneto-elastic behavior.

The constitutive equations for the magnetic field strength $\boldsymbol{H}$ and the Cauchy stress tensor $\boldsymbol{\sigma}$, considering an isotropic ferromagnetic material, are obtained by computing the partial derivatives of ψ with respect to $\boldsymbol{B}$ and $\boldsymbol{\varepsilon}$ as

$$\boldsymbol{H}(\boldsymbol{B}, \boldsymbol{\varepsilon}) = \left(\frac{\partial\psi}{\partial\boldsymbol{B}}\right)^{\mathrm{T}} \text{and}\ \boldsymbol{\sigma}(\boldsymbol{B}, \boldsymbol{\varepsilon}) = \frac{\partial\psi}{\partial\boldsymbol{\varepsilon}}, \tag{3}$$

where T denotes the transpose.

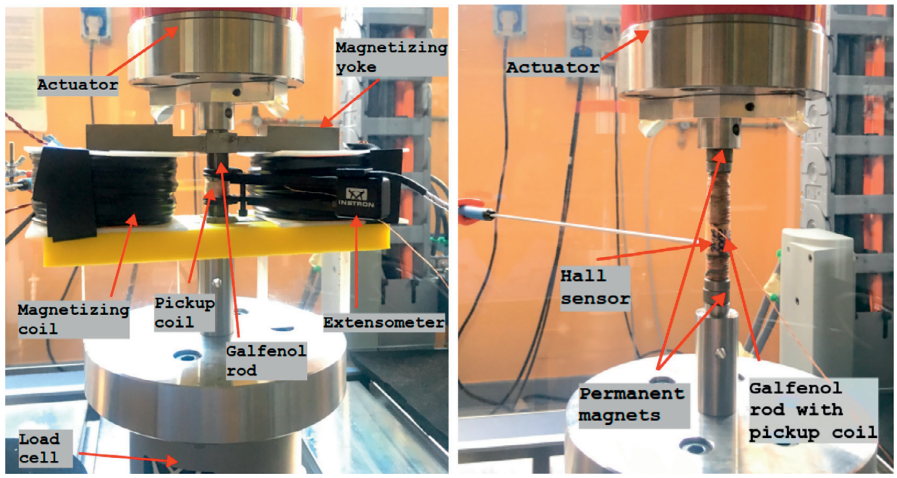

Fig. 3. Actual setup for the material characterization (left) and energy harvester concept device (right).

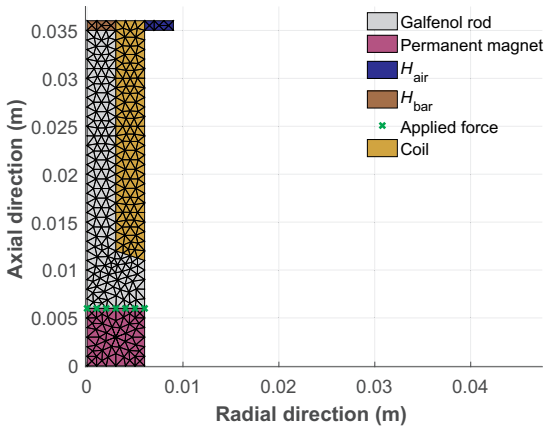

Fig. 4. Geometry and FE mesh of the prototype harvesters' concept device used in the axisymmetric magneto-mechanical FE model. The markers denote the nodes where the force is applied. Due to symmetry, only one half of the geometry is modeled.

3.2. Finite element model

In the actuator material, the axisymmetric magneto-mechanical FE model is based on solving the mechanical balance equations and the combination of Ampere's and Faraday's laws:

$$\nabla\cdot\sigma(B,\varepsilon)=0, \tag{4}$$

$$\nabla\times\boldsymbol{H}(\boldsymbol{B},\boldsymbol{\varepsilon})+\kappa\frac{\partial\boldsymbol{A}}{\partial t}=0, \tag{5}$$

where κ is the electrical conductivity. The circumferential magnetic vector potential $\boldsymbol{A}=A\boldsymbol{e}_\theta$, and the displacement vector $\boldsymbol{u}=u_r\boldsymbol{e}_r+u_z\boldsymbol{e}_z$ in the symmetry plane are used as the field variables, from which the flux density and strain are obtained as $\boldsymbol{B}=\nabla\times\boldsymbol{A}$ and $\boldsymbol{\varepsilon}=(\nabla\boldsymbol{u}+(\nabla\boldsymbol{u})^{\mathrm{T}})/2$. Eqs. (4) and (5) are coupled through the constitutive law (2) and (3). In other regions with constant magnetic reluctivity ν, only the electromagnetic problem

$$\nu\nabla\times\nabla\times\boldsymbol{A}+\kappa\frac{\partial\boldsymbol{A}}{\partial t}=\boldsymbol{J}_s+\nabla\times\boldsymbol{H}_c, \tag{6}$$

is solved. $\boldsymbol{J}_s=(Ni_{coil}/S_{coil})\boldsymbol{e}_\theta$ is the circumferential source current density, which is nonzero only in the pickup coil with N turns, cross-sectional area S_{coil} and current i_{coil}, while κ and $\boldsymbol{H}_c=H_c\,\boldsymbol{e}_z$ are the electrical conductivity and axially-oriented coercive field respectively, which are nonzero only in the permanent magnets.

The field problem and the variables A, u_r and u_z are discretized using a standard Galerkin FE discretization with nodal shape functions $\boldsymbol{N}=[N_1, N_2, \ldots]$. The current i_{coil} of the pickup coil is set as an additional variable to be solved from a voltage equation, assuming the coil to have an internal resistance R and to be connected to a load resistance R_{load}. The complete system of equations is

$$\begin{aligned}
&\int_\Omega r\left(-\left(\frac{\partial\boldsymbol{N}^{\mathrm{T}}}{\partial r}+\frac{\boldsymbol{N}^{\mathrm{T}}}{r}\right)H_z+\frac{\partial\boldsymbol{N}^{\mathrm{T}}}{\partial z}H_r\right)d\Omega+\left(\int_\Omega r\kappa\boldsymbol{N}^{\mathrm{T}}\boldsymbol{N}d\Omega\right)\frac{d\boldsymbol{a}}{dt}-\boldsymbol{D}i_{coil}=0,\\
&\int_\Omega r\left(\frac{\partial\boldsymbol{N}^{\mathrm{T}}}{\partial r}\sigma_{rr}+\frac{\partial\boldsymbol{N}^{\mathrm{T}}}{\partial z}\sigma_{zz}\right)d\Omega+\int_\Gamma r\boldsymbol{N}^{\mathrm{T}}[\sigma_{rr}\ \sigma_{zz}]\boldsymbol{n}d\Gamma=0,\\
&\int_\Omega r\left(\frac{\partial\boldsymbol{N}^{\mathrm{T}}}{\partial r}\sigma_{rr}+\frac{\boldsymbol{N}^{\mathrm{T}}}{r}\sigma_{\theta\theta}+\frac{\partial\boldsymbol{N}^{\mathrm{T}}}{\partial z}\sigma_{rz}\right)d\Omega+\int_\Gamma r\boldsymbol{N}^{\mathrm{T}}[\sigma_{rr}\ \sigma_{rz}]\boldsymbol{n}d\Gamma=0,\\
&\boldsymbol{C}\frac{d\boldsymbol{a}}{dt}+(R+R_{load})i_{coil}=0,
\end{aligned} \tag{7}$$

where r denotes the radial coordinate and the vector $\boldsymbol{a}$ contains the nodal values of the vector potential, $A=\boldsymbol{N}\boldsymbol{a}$. Furthermore, σ_{rr}, σ_{zz}, $\sigma_{\theta\theta}$, H_r and H_z are the radial (r), axial (z) and circumferential (θ) components of the stress and the magnetic field strength, respectively. In addition, Ω denotes the calculation domain in the axisymmetric plane, Γ the boundary lines inside Ω where the mechanical loading is applied, and $\boldsymbol{n}$ the outer normal vector of Γ. The winding matrices related to the flux linkage $\boldsymbol{C}$ and source current density $\boldsymbol{D}$ are given by,

$$\begin{aligned}
\boldsymbol{C}&=\frac{2\pi N}{S_{coil}}\int_{\Omega_{coil}}r\boldsymbol{N}d\Omega\ ,\\
\boldsymbol{D}&=\frac{N}{S_{coil}}\int_{\Omega_{coil}}r\boldsymbol{N}^{\mathrm{T}}d\Omega\ .
\end{aligned} \tag{8}$$

As boundary conditions, A is fixed to zero at the outer boundaries, and radial displacement u_r and axial displacement u_z are fixed to zero at the longitudinal middle axis and in the middle cross-section of the actuator, respectively. The time-derivatives are discretized using the Backward-Euler method,

$$\frac{d\boldsymbol{a}}{dt}=\frac{\boldsymbol{a}-\boldsymbol{a}_{prev}}{\Delta t}, \tag{9}$$

where Δt is the time step which is chosen to be 100 μs, and the discretized system (7) is solved with the Newton-Raphson method.

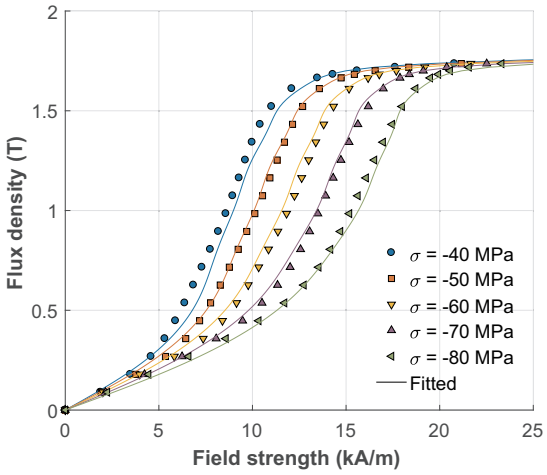

Fig. 5. Measured and fitted magnetization curves under different values of static compressive stress.

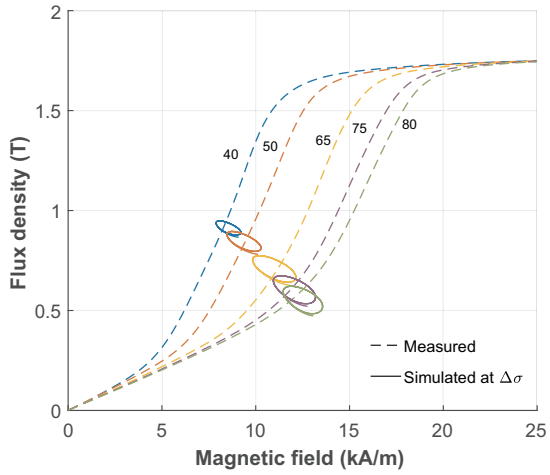

Fig. 6. Measured magnetization curves obtained during characterization at various compressive preload (σ) values and simulated dynamic hysteresis loops under cyclic loading ($\Delta\sigma$) of 8 MPa.

4. Results

4.1. Fitting of the constitutive model

The measured magnetization curves and their fitting to the analytical expression (2) under various static compressive loadings are presented in Fig. 5. The measured results are plotted as single valued *B-H* curves by taking the mean value of the hysteresis loop. It is worthwhile to note that galfenol shows negligible hysteresis and a small coercive field, which means lower energy conversion losses as compared to Terfenol-D [20,22]. Therefore, taking the mean value of the hysteresis loop does not significantly affect the accuracy of the solution. The result shows that the permeability of the material decreases due to applied compressive stress. In addition, the fitted curves accurately correspond to the measured curves. The percentage differences between measured and simulated field strengths are 17.94% for 40 MPa, 4.76% for 50 MPa, 8.83% for 60 MPa, 4.09% for 70 MPa and 7.45% for 80 MPa preload values. The values of the fitting parameters for α_i, β_i and γ_i when $n_\alpha = 11$, $n_\beta = 1$ and $n_\gamma = 2$ are given in Table 1. The values for Young's modulus and Poisson's ratio utilized during simulation are 75 GPa and 0.4 respectively.

4.2. Finite element simulations

The measured magnetization curves are utilized in FE simulations of the prototype harvester concept device to compute the change in the magnetic flux density (ΔB) inside the sample under cyclic mechanical loading. ΔB and the corresponding magnetic fields are averaged over the region H_{bar} shown in Fig. 4. The measurement results of the magnetization curves under static preload (40–80 MPa) and simulated results of ΔB upon static loading (40–80 MPa) followed by a dynamic cyclic loading ($\Delta\sigma$) of 8 MPa at 100 Hz frequency are presented in Fig. 6. The ΔB upon mechanical vibration is plotted as hysteresis loops representing the operating points of *B*. The simulated results of ΔB help to analyze and determine the optimal preload value. Both measurements and simulations were performed using preload values ranging from 0 to 80 MPa. However, not all of the *B-H* curves are plotted, in order to avoid overlapping and to clearly demonstrate the effect of preload upon magnetic flux density. The results in Fig. 6 depict change in the ΔB for different values of preload, which is shown by the area of the hysteresis loops. Such an area represents the average power at the corresponding preload case. A large area means a large ΔB value, which will generate higher power.

Table 1
Coefficients of the model parameters.

Parameter	Value (J/m^3)	Parameter	Value (J/m^3)
α_1	9.217×10^3	α_8	-1.071×10^4
α_2	-1.208×10^4	α_9	2.754×10^3
α_3	1.854×10^4	α_{10}	-399.5
α_4	-3.159×10^4	α_{11}	24.99
α_5	4.286×10^4	β_1	4.647×10^6
α_6	-4.082×10^4	γ_1	1.128×10^{10}
α_7	2.595×10^4	γ_2	-6.977×10^5

In order to validate the proposed axisymmetric FE model, the measurements for the average output power from the concept harvester setup are compared with the simulation results. The comparison between the measured and simulated average power is given in Fig. 7(a) and (b) respectively, under a constant dynamic load of 8 MPa and using seven different preload cases ranging from 40 to 80 MPa.

The time step length of $\Delta t = 100$ µs (100 steps per one fundamental period) of the 100 Hz mechanical loading, was considered suitable providing reasonable accuracy of the solution. A magnetostatic solution was used as the initial state, and three fundamental periods were simulated to ensure steady state. The simulations take approximately 130 ms per one time step, independently of the used time step (Δt). Various time step lengths were tested for the 56 simulations shown in Fig. 7(b), and the total computation time for all simulations and the percentage difference of the output power with respect to the $\Delta t = 100$ µs case were compared. The results for the comparison are presented in Table 2.

The results from the table show that reducing the time step down to $\Delta t = 12.5$ µs the output power increases by 2.5% compared to the $\Delta t = 100$ µs case at the additional computational cost of 152 min. On the other hand, increasing the time step to $\Delta t = 200$ µs the output power decreases by 2.7%, saving 14 min. Thus, the step size of 100 µs resulted to be a good compromise between the accuracy of the solution and the computation time.

The repeatability of the measurements is crucial to obtain accurate results. For this reason, three consecutive tests were conducted without perturbing the external conditions and the output power was recorded carefully each time. The measurement results in Fig. 7(a) are thus

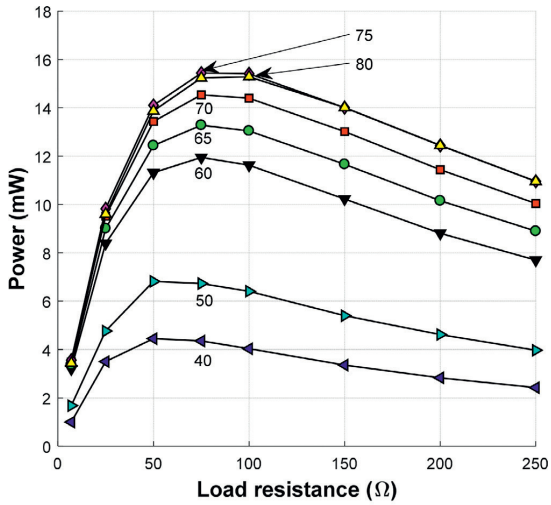

Fig. 7. Comparison among measured (a) and simulated (b) average power under constant dynamic load (8 MPa) and changing preload (σ).

Table 2
Simulation times and output power differences for different step sizes (for the 56 simulations in Fig. 7(b)).

Time step Δt (μs)	Total simulation time (min)	Power difference w.r.t. Δt = 100 (μs)
200	20	−2.7%
100	36	0%
50	72	1.5%
33	86	1.9%
25	133	2.2%
20	165	2.4%
12.5	188	2.5%

plotted as the average of three repeatedly done experiments. The measured results from Fig. 7(a) show that the output power increases with the increase in the preload, reaches its maximum at 75 MPa, and then starts decreasing gradually. The same phenomenon is also predicted by the simulated results in Fig. 7(b), but with slightly higher

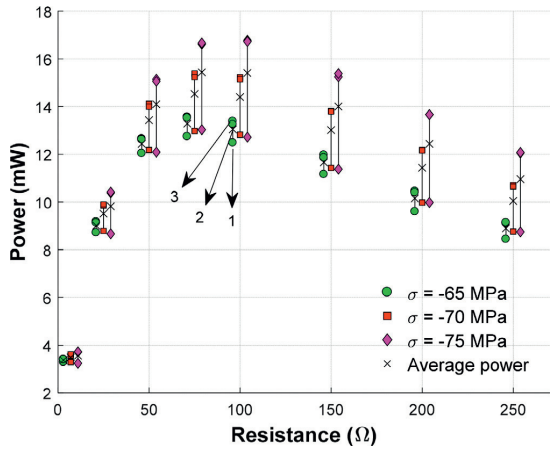

Fig. 8. Output powers obtained from the three separate measurement sessions (1, 2 and 3). The markers denote the measured output powers from each session. The crosses denote the average values, i.e., the results presented in Fig. 7(a). The −65 MPa and −75 MPa markers have been shifted horizontally for clarity, but the resistance values are the same for each preload.

amplitudes.

This increase in power is due to the change in the flux density variation ΔB with the increase of preload. The flux density variation reaches its maximum value around 75 MPa, which is also evident from the area of the hysteresis loops in Fig. 6. The ΔB at 75 and 80 MPa preload under dynamic load of 8 MPa is computed as 152.7 and 147.2 mT respectively. Furthermore, the output power is given as a function of the load resistance. The load resistance is varied in order to determine its optimal value at which maximum power can be obtained. In both the measurements and simulations, the optimal load resistance remains constant at 75 Ω.

In addition, some differences in the measured output power for the three repeatedly performed experiments were observed without perturbing the external conditions. The output powers for the separate sessions (1, 2 and 3) are presented in Fig. 8. The average power is presented as crosses, which corresponds to the measurement results shown in Fig. 7(a) for three different loading cases (−65, −70 and −75 MPa). It was observed that, in the first session, a lower output power is obtained compared to second and third sessions which are nearly coincident, which shows the sensitivity of the measurements to the external conditions. In addition, variability between single experiments increases with the preload. The maximum percentage difference between the variations of the measurements vs. the average output power at 65 MPa is lower than 10%, at 70 MPa is lower than 20% and at 75 MPa reaches 30% respectively. We are mostly interested in the higher stress range values, thus, the selection of (65–80 MPa) preload and dynamic load (8 MPa) is made considering the specific range of prestress values yielding maximum output power. Moreover, it was observed that even a minor misalignment of the sample also affects the repeatability of the measurements.

The comparison among measured and simulated field strength H in the air near the middle part of the sample (region H_{air} in Fig. 4) is presented in Fig. 9. Both the measurements and simulations show an increasing H under increasing compression. This can be explained by the illustration presented in Fig. 10, where a simplified sample with relative permeability μ_r is placed between two permanent magnets. As μ_r is decreased (from the left to the right in Fig. 10), a larger share of the total flux is forced into the air, which is seen in the bending flux lines near the middle part of the sample indicated by the dashed line. The same happens when the permeability of the sample decreases due to an

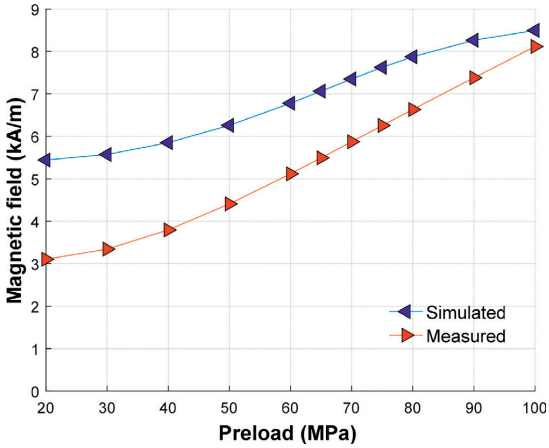

Fig. 9. Comparison among measured and simulated magnetic field intensity H (average values) near the middle part of the sample for different preload values under constant dynamic load (8 MPa).

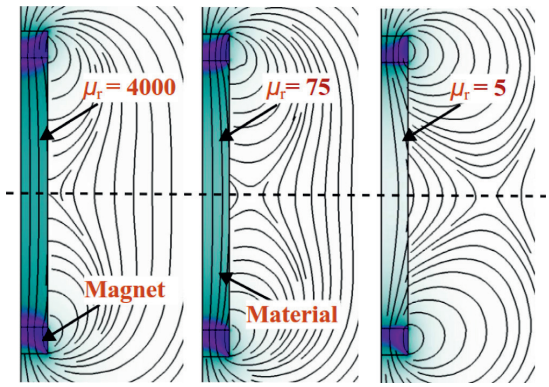

Fig. 10. Simulated field lines of magnetic flux density around a rectangular material sample magnetized by two permanent magnets at both ends at three different values of relative permeability (μ_r). The dashed line represents the area of interest where B is computed.

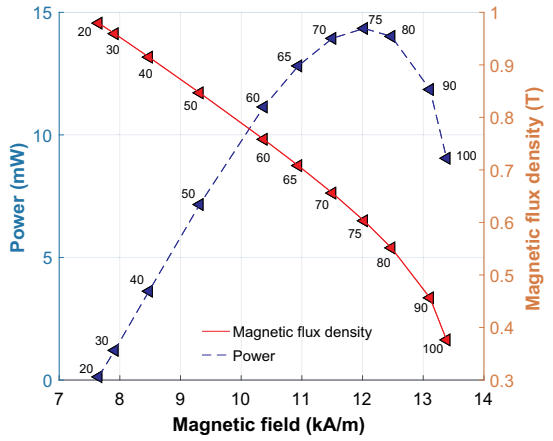

Fig. 11. Simulated results for the mean value of magnetic flux density inside the bar and average output power under various prestress values at dynamic load of 8 MPa, using 75 Ω as load resistance.

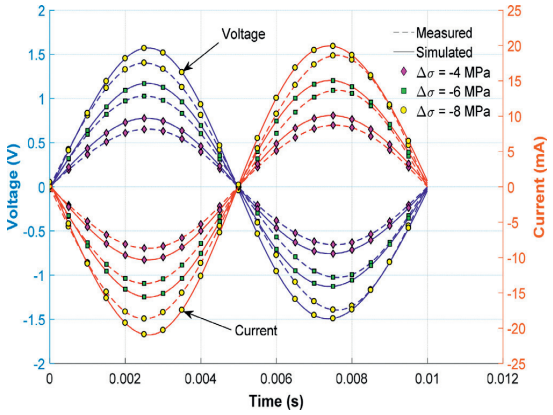

Fig. 12. Measured and simulated voltage and current waveforms under a constant preload (65 MPa) and a changing dynamic load using a constant load resistance of 75 Ω.

increase in compression. Fig. 9 also shows that the simulated magnetic field is overestimated as compared to measured one, and that the difference reduces when compression increases. This is due to the fact that the model slightly underestimates the permeability of the sample for lower values of stress, like seen in the −40 MPa curve in Fig. 5. Comparison among the measured and simulated average power, presented in Fig. 7, should be evaluated keeping in view the limitations of the model, the sensitivity of the measurements and their repeatability.

Now, in order to validate the optimal preload value of 75 MPa suggested by Fig. 7(a) and (b), simulations were conducted at a wider range of preload values (20–110 MPa) to clearly see the effect of the preload on the output power. The results of the mean value of B inside the bar computed at region H_{bar} from Fig. 4 and the average output power vs. H at preload ranging from 20 to 110 MPa are presented in Fig. 11. The simulation is done using a dynamic load of 8 MPa together with the optimal load resistance value of 75 Ω yielding the maximum power. The results from Fig. 11 also evidence an increase in the output power, reaching its maximum at 75 MPa, and then decreasing upon further increase in the preload.

The comparison of measured and simulated waveforms of the current and voltage at the optimal load resistance value of 75 Ω under a constant preload of 65 MPa and a changing dynamic load (6–8 MPa) is presented in Fig. 12. As expected, the measured and simulated results evidence an increase of the induced voltage and current under an increase in the amplitude of the dynamic cyclic load. This validates the fact that the output power is directly proportional to the increase in the amplitude of mechanical vibrations [22]. In addition, the simulated results of voltage and current are in quite a good agreement with the measured results, following the trend reasonably, which also validates the modeling approach.

5. Discussion and conclusion

An axisymmetric FE model utilizing a thermodynamic approach was presented in this paper to analyze the magneto-mechanical behavior of a magnetostrictive energy harvester concept device. A comparison between measured and simulated results was carried out to validate the proposed modeling approach. The comparison showed that the model can predict the simulated values of power, voltage and current with reasonable accuracy, and accurately follows the trend of the

measurement results.

The measurements under dynamic loading were found quite sensitive to changes in external parameters, including the warm-up time for the harvester device, the displacement of permanent magnets, and the alignment of the harvester with respect to the vertical loading system. These parameters should be kept constant to ensure reproducibility in the measured results. Therefore, the measured values were taken as the average of repeated readings for three consecutive experiments in order to compensate for some variability in the measurements. The difference in the measured and simulated results is in part due to limitations of the model and the lack of repeatability of the measurements, as indicated in Fig. 8. Furthermore, some of the difference between the measured and simulated values also occurs because the model overestimates the relative permeability of the material, as discussed in Section 4.2.

In this study, we are mainly interested in the prestress range that maximizes the output power. It was observed that the measured and simulated power for the preload values ranging from 65 to 80 MPa better match each other, following the trend reasonably, with slightly higher amplitudes for the simulated values. In addition, the maximum output power is a function of preload and load resistance. Therefore, load resistance is varied to obtain an optimal value that results in maximum power. The FE model enabled us to compute the magnetic flux density inside the sample, which is not possible to measure physically. The results presented in Fig. 11 provide insight into how the permeability of the material changes under applied compressive preload, as well as its influence on the output power. Given the general agreement between calculated and simulated results, the device behavior for preloads greater than 80 MPa has been extrapolated using the numerical model. The simulated results for the preload ranging from 20 to 110 MPa suggest that the maximum power can only be obtained at a certain preload value (75 MPa) and a certain magnetic field bias that serve as design characteristics. The proposed modeling approach can thus be applied to analyze a magneto-mechanical energy harvester and determine the optimal design characteristics and operating conditions.

Acknowledgement

This work was supported by the Academy of Finland (304112).

References

[1] M.J. Dapino, On magnetostrictive materials and their use in adaptive structures, Struct. Eng. Mech. 17 (3–4) (2004) 303–330.
[2] T. Zhang, C. Jiang, H. Zhang, H. Xu, Giant magnetostrictive actuators for active vibration control, Smart Mater. Struct. 13 (3) (2004) 473.
[3] F. Fiorillo, Measurements of magnetic materials, Metrologia 47 (2) (2010) S114.
[4] D. Davino, A. Giustiniani, C. Visone, Capacitive load effects on a magnetostrictive fully coupled energy harvesting device, IEEE Trans. Magn. 45 (10) (2009) 4108–4111.
[5] J. Atulasimha, A.B. Flatau, A review of magnetostrictive iron–gallium alloys, Smart Mater. Struct. 20 (4) (2011) 043001.
[6] V. Berbyuk, Vibration energy harvesting using galfenol-based transducer, Active and Passive Smart Structures and Integrated Systems 2013, International Society for Optics and Photonics, 2013, p. 86881F.
[7] R.A. Kellogg, A.B. Flatau, A.E. Clark, M. Wun-Fogle, T.A. Lograsso, Temperature and stress dependencies of the magnetic and magnetostrictive properties of Fe 0.81 Ga 0.19, J. Appl. Phys. 91 (10) (2002) 7821–7823.
[8] L. Weng, T. Walker, Z. Deng, M.J. Dapino, B. Wang, Major and minor stress-magnetization loops in textured polycrystalline Fe 81.6 Ga 18.4 Galfenol, J. Appl. Phys. 113 (2) (2013) 024508.
[9] J.H. Yoo, G. Pelligrini, S. Datta, A.B. Flatau, An examination of galfenol mechanical–magnetic coupling coefficients, Smart Mater. Struct. 20 (7) (2011) 075008.
[10] M. Wun-Fogle, J.B. Restorff, A.E. Clark, E. Dreyer, E. Summers, Stress annealing of Fe–Ga transduction alloys for operation under tension and compression, J. Appl. Phys. 97 (10) (2005) 10M301.
[11] R. Bellotti, P. Mei, G. Picotto, M. Santiano, M. Zucca, Strain measurements of cylinder magnetostrictive samples by interferometer readings, 17th International EUSPEN Conference & Exhibition, EUSPEN, 2017, pp. 379–380.
[12] L. Daniel, O. Hubert, M. Rekik, A simplified 3-D constitutive law for magneto-mechanical behavior, IEEE Trans. Magn. 51 (3) (2015) 1–4.
[13] S. Chakrabarti, M.J. Dapino, Coupled axisymmetric finite element model of a hydraulically amplified magnetostrictive actuator for active powertrain mounts, Finite Elem. Anal. Des. 60 (2012) 25–34.
[14] K. Fonteyn, A. Belahcen, R. Kouhia, P. Rasilo, A. Arkkio, FEM for directly coupled magneto-mechanical phenomena in electrical machines, IEEE Trans. Magn. 46 (8) (2010) 2923–2926.
[15] P.G. Evans, M.J. Dapino, Efficient magnetic hysteresis model for field and stress application in magnetostrictive Galfenol, J. Appl. Phys. 107 (6) (2010) 063906.
[16] F.C. Graham, C. Mudivarthi, S. Datta, A.B. Flatau, Modeling of a Galfenol transducer using the bidirectionally coupled magnetoelastic model, Smart Mater. Struct. 18 (10) (2009) 104013.
[17] D. Davino, P. Krejčí, C. Visone, Fully coupled modeling of magneto-mechanical hysteresis through thermodynamic compatibility, Smart Mater. Struct. 22 (9) (2013) 095009.
[18] J.L. Pérez-Aparicio, H. Sosa, A continuum three-dimensional, fully coupled, dynamic, non-linear finite element formulation for magnetostrictive materials, Smart Mater. Struct. 13 (3) (2004) 493.
[19] D. Davino, P. Krejčí, A. Pimenov, D. Rachinskii, C. Visone, Analysis of an operator-differential model for magnetostrictive energy harvesting, Commun. Nonlinear Sci. Numer. Simul. 39 (2016) 504–519.
[20] C.S. Clemente, A. Mahgoub, D. Davino, C. Visone, Multiphysics circuit of a magnetostrictive energy harvesting device, J. Intell. Mater. Syst. Struct. 28 (17) (2017) 2317–2330.
[21] B. Rezaeealam, Finite element analysis of magnetostrictive vibration energy harvester, COMPEL 31 (6) (2012) 1757–1773.
[22] S. Palumbo, P. Rasilo, M. Zucca, Experimental investigation on a Fe-Ga close yoke vibrational harvester by matching magnetic and mechanical biases, J. Magn. Magn. Mater. 469 (2019) 354–363.

PUBLICATION II

Modeling a Fe-Ga Energy Harvester Fitted with Magnetic Closure Using 3D Magneto-Mechanical Finite Element Model

U. Ahmed, U. Aydin, M. Zucca, S. Palumbo, R. Kouhia and P. Rasilo

Journal of Magnetism and Magnetic Materials 500 (2020)
DOI: 10.1016/j.jmmm.2020.166390

Journal of Magnetism and Magnetic Materials 500 (2020) 166390

Contents lists available at ScienceDirect

Journal of Magnetism and Magnetic Materials

journal homepage: www.elsevier.com/locate/jmmm

Research articles

Modeling a Fe-Ga energy harvester fitted with magnetic closure using 3D magneto-mechanical finite element model

U. Ahmed[a,*], U. Aydin[a,b], M. Zucca[c], S. Palumbo[c,d], R. Kouhia[e], P. Rasilo[a]

[a] Tampere University, Electrical Engineering, P.O. Box 692, FI-33720, Tampere (Hervanta Campus), Finland
[b] Aalto University, Department of Electrical Engineering and Automation, P.O. Box 15500, FI-00076, Espoo, Finland
[c] Istituto Nazionale di Ricerca Metrologica, INRIM, Strada delle Cacce 91, Torino, Italy
[d] Politecnico di Torino, Dipartimento di Elettronica e Telecomunicazioni, Corso Duca degli Abruzzi 24, Torino, Italy
[e] Tampere University, Civil Engineering, P.O. Box 600, 33014 Tampere University (Hervanta Campus), Finland

ARTICLE INFO

Keywords:
Energy harvesting
Finite element analysis
Magneto-elasticity
Helmholtz free energy
Magnetostrictive devices

ABSTRACT

This paper presents the implementation of magneto-mechanical constitutive law utilizing thermodynamic approach in a 3D finite element solver using COMSOL Multiphysics software. The analytical expression for the magnetic field strength and stress is derived from the constitutive model utilizing magnetic flux density and mechanical strain as state variables. The constitutive model is successfully implemented in commercially available software COMSOL. This implementation allows 3D analysis of an energy harvester device efficiently and accurately. A prototype concept device is developed to validate the model and its implementation. The device is tested under uniaxial compressive loading by varying the preload, dynamic load and magnetic bias. The model is validated by comparing the simulated and experimental results. The comparison shows that the model can reasonably predict the optimal value of the preload and magnetic bias yielding maximum power and is able to follow the measurement trends. This model can be used as a suitable tool to analyze the behavior of the concept energy harvesters and determine the optimal design parameters.

1. Introduction

Magneto-mechanical energy harvesters based on giant magnetostrictive materials (GMMs) allow conversion of ambient vibration energy from moving parts of machines, bridges and rail tracks etc. into electrical energy to power-up small-scale sensors and microelectronic systems. This enables an autonomous and battery free solution for wireless sensor nodes suitable in various applications including structural condition monitoring and biomedical applications. The GMMs can be utilized as transducers for active vibration control sensors. Among GMMs, galfenol exhibits strong magneto-mechanical coupling, low hysteresis losses, and high tensile strength (~500 MPa) as compared to Terfenol-D, making it a suitable candidate to be incorporated as an active material for the energy harvester. Terfenol-D is brittle in nature having low tensile strength (28–40 MPa) with poor machinability whereas galfenol can be welded and machined easily, thus providing more practical options to be utilized as an active material. A comparison among the characteristics of Terfenol-D and galfenol is presented in [1].

The design process of an energy harvester requires knowledge about the characteristics of the active material, the external operating conditions (magnetic bias, frequency and amplitude of mechanical vibrations) as well as the device design (geometry). Numerous studies have been carried out related to modeling and design of magnetostrictive energy harvesters [2] and [3]. During last decade, the focus has been shifted towards optimizing the device design and determining the optimal operating conditions to maximize the potential of the harvesters [3–6]. Modeling tools are required to analyze the coupled magneto-mechanical effects in ferromagnetic materials to determine efficient device design and optimal operating conditions for the energy harvester. Various models have been developed to study the effect of design parameters [5–8], but there is a lack of knowledge related to the influence of the several design parameters yielding maximum output power, which include the geometry of the device, applied magnetic bias, external loading and magnetic closure circuit. Moreover, there is no generic model to fully analyze the behavior of the energy harvester or to suggest suitable operating conditions and design parameters.

The proposed paper utilizes thermodynamic magneto-mechanical constitutive laws developed in [9] and [10] to be implemented in a 3D finite element (FE) model using COMSOL Multiphysics software. The model is validated by comparing the measurement results obtained

* Corresponding author.
E-mail address: umair.ahmed@tuni.fi (U. Ahmed).

https://doi.org/10.1016/j.jmmm.2020.166390
Received 5 September 2019; Received in revised form 28 December 2019; Accepted 2 January 2020
Available online 03 January 2020
0304-8853/

from the prototype energy harvester concept device developed in [5]. The aim of this paper is to extend the model presented in [9] from 2D axisymmetric to full 3D analysis of energy harvester devices. The model is applied to analyze a concept device including a galfenol rod, permanent magnets and a magnetic flux closure constructed with soft magnetic material. The results are analyzed to determine the influence of the design parameters on the device performance.

2. Experimental setup and working principle

2.1. Material characterization

The experimental setup is presented in two parts. In the first setup, the characterization of the material is performed for the identification of the constitutive laws describing the magneto-elastic behavior. A cylindrical rod of galfenol ($Fe_{81.6}Ga_{18.4}$) is used as the active material for the prototype energy harvesting concept device. The overall dimensions of the rod are 60 mm in length with the diameter of 12 mm [9]. The magnetization (B–H) and magnetostriction curves were obtained under various static axial compressive preload (σ) values ranging from 0 to 80 MPa. The sample is magnetized using an AC magnetization of 200 mHz. The preload is controlled by the loading machine to be constant during magnetization. The complete setup for the material characterization is presented in Fig. 1 where the galfenol rod is magnetized with the help of two coils and a U-shaped core. The Hall probe measures the magnetic field strength H near the middle part of the sample. The strain is measured using an extensometer clamped at the middle part of the sample. The magnetic flux density B is obtained by integrating the induced voltage from the pickup coil wound around the sample.

2.2. Energy harvester

The second setup is related to the energy harvester consisting of a galfenol rod as an active material which is magnetized with the help of permanent magnets and four L-shaped cores. The schematic diagram of the prototype harvester concept device is presented in Fig. 2. The galfenol rod is first machined to accommodate the pickup coil consisting of 2000 turns with the wire diameter of 0.2 mm as shown in Fig. 2. After machining the sample, the diameter of the sample is reduced to 6 mm for the length of 48 mm. Having a smaller cross-section allows us to study the behavior of the harvester at large range of mechanical biases, for the same stress exerted by the test machine. The test machine can exert a maximum sinusoidal force of about 7 kN rms (10 kN peak). The actual experimental setup is shown in Fig. 3. A constant magnetic bias is applied using NdFeB magnets having a remanence flux density of B_r = 1.1 T and coercive field strength of H_c = 955 kA/m with physical dimensions of 6 mm in thickness and 12 mm in diameter.

Two different cases were studied during experimentation indicated as Yoke#A and Yoke#B in Fig. 3. The case Yoke#A consists of one magnet on each column whereas Yoke#B has two magnets on both columns. The length of the columns from the L-shaped core is reduced to accommodate the magnets so that the overall length of the magnetic circuit remains the same.

For the energy harvester setup, the galfenol rod is first subjected to static compressive preload σ superposed with a sinusoidal dynamic compressive load with amplitude $\Delta\sigma$ and frequency of 100 Hz. The voltage is induced into the pickup coil due to applied dynamic load because of inverse magnetostrictive effect and Faraday's law. The output power is measured using 160 Ω load resistance for preload σ = 20–80 MPa keeping the dynamic load and vibration frequency constant. The maximum power is obtained as a function of magnetic bias and preload. In this study, we test the ability of the model in reproducing the effect of magnetic bias, preload and dynamic load on the harvester.

3. Models

3.1. Constitutive model

The derivation of coupled magneto-mechanical constitutive laws for the actuator material in an energy harvester using a thermodynamic approach is presented in [9]. The approach is based on deriving the Helmholtz free energy density $\psi(\boldsymbol{B}, \boldsymbol{\varepsilon})$ as a function of magnetic flux

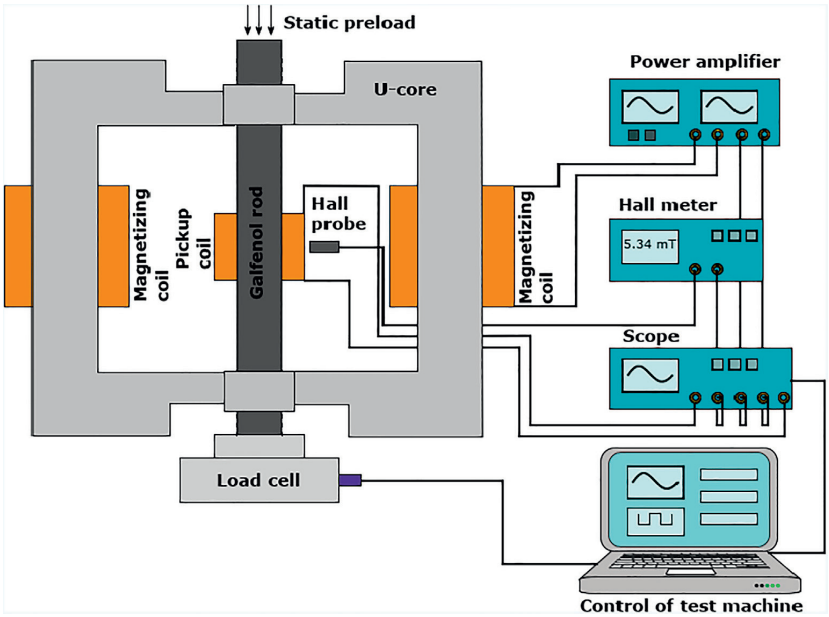

Fig. 1. Schematic diagram for the characterization of the material.

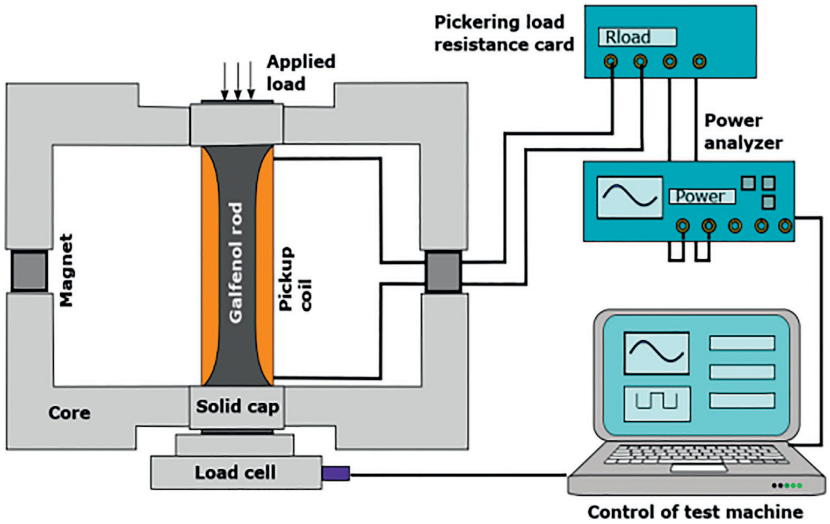

Fig. 2. Schematic diagram of the complete energy harvester setup and the internal structure of machined galfenol rod (sliced diagram).

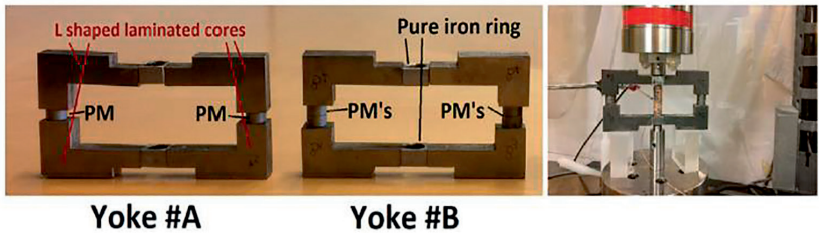

Fig. 3. The actual setup for the energy harvester (right), magnetic closure circuit with 2 magnets (Yoke #A) and 4 magnets (Yoke #B) on both sides.

density vector $\boldsymbol{B}$ and strain tensor $\boldsymbol{\varepsilon}$. Assuming the actuator material to be isotropic, the state variables $\boldsymbol{B}$ and $\boldsymbol{\varepsilon}$ are written in terms of six scalar invariants. The analytical expressions for the invariants can be found from [9]. The Helmholtz free energy density describing coupled magneto-mechanical behavior in the actuator material is written as

$$\psi = \frac{1}{2}\lambda I_1^2 + \mu I_2 + \sum_{i=1}^{n_\alpha} \alpha_i I_4^i + \sum_{i=1}^{n_\beta} \beta_i I_5^i + \sum_{i=1}^{n_\gamma} \gamma_i I_6^i \,, \tag{1}$$

where λ and μ are the Lamé parameters obtained from Young's modulus and Poisson's ratio, and the fitting parameters α_i, β_i and γ_i are polynomial coefficients fitted against the B–H curves obtained from the characterization of the material discussed in Section 2.1. The invariants I_1 and I_2 describe pure mechanical behavior, I_4 describes pure magnetic behavior and I_5 and I_6 describe magneto-elastic behavior. The invariant I_3 is not utilized since linear elastic behavior is considered in the absence of magnetic field. The constitutive equations for the magnetic field strength $\boldsymbol{H}$ and the Cauchy stress tensor $\boldsymbol{\sigma}$ are thus derived by computing the partial derivatives of ψ with respect to $\boldsymbol{B}$ and $\boldsymbol{\varepsilon}$

$$\boldsymbol{H}(\boldsymbol{B}, \boldsymbol{\varepsilon}) = \left(\frac{\partial \psi}{\partial \boldsymbol{B}}\right)^{\mathrm{T}} \text{ and } \boldsymbol{\sigma}(\boldsymbol{B}, \boldsymbol{\varepsilon}) = \frac{\partial \psi}{\partial \boldsymbol{\varepsilon}} \,, \tag{2}$$

where T denotes the transpose of a vector. The constitutive equations are symbolically derived in MATLAB, and their free parameters α_i, β_i and γ_i are fitted to the measurement data from the characterization of the material. The constitutive model allows analytical calculation of $\boldsymbol{H}$ and $\boldsymbol{\sigma}$ as a function of $\boldsymbol{B}$ and $\boldsymbol{\varepsilon}$.

3.2. Finite element model

The constitutive equations developed in section 3.1 are implemented in a 3D FE solver in COMSOL Multiphysics. The 3D magneto-mechanical FE simulation is carried out for 1/8th of the geometry presented in Fig. 4. The magnetic field strength H_{air} is computed near the middle part of the sample and mechanical stress is applied at the bottom of the sample indicated by arrows pointing in Fig. 4. The

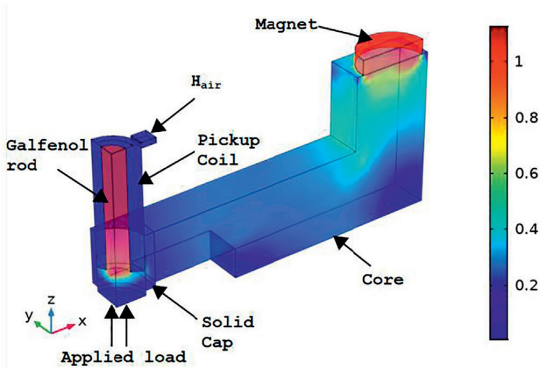

Fig. 4. The geometry of the model implemented in COMSOL for 3D FE simulation. Legend bar denotes magnetic flux density norm (T).

magnetic field interface is added which solves for the Maxwell's equations to compute the electromagnetic fields. The solid mechanics interface is added for the active material that solves the mechanical balance equations. The material model (2) based on ψ is implemented by overriding the electromagnetic and mechanical constitutive models. The magneto-mechanical FE model is then based on solving the mechanical balance equations together with the combination of Faraday's and Ampere's laws:

$$\nabla \cdot \boldsymbol{\sigma}(\boldsymbol{B}, \boldsymbol{\varepsilon}) = 0\,, \tag{3}$$

$$\nabla \times \boldsymbol{H}(\boldsymbol{B}, \boldsymbol{\varepsilon}) + \kappa \frac{\partial \boldsymbol{A}}{\partial t} = 0\,, \tag{4}$$

where κ is the electrical conductivity and $\boldsymbol{A}$ is the magnetic vector potential. The flux density and strain are obtained as $\boldsymbol{B} = \bigtriangledown \times \boldsymbol{A}$ and $\boldsymbol{\varepsilon} = (\bigtriangledown \boldsymbol{u} + (\bigtriangledown \boldsymbol{u})^{\mathrm{T}})/2$, where $\boldsymbol{u}$ is the displacement vector used as the field variable. The partial differential Eqs. (3) and (4) are coupled through the constitutive law (1) and (2). In other regions only the electromagnetic problem is solved as

$$\nabla \times \boldsymbol{\nu} \nabla \times \boldsymbol{A} + \kappa \frac{\partial \boldsymbol{A}}{\partial t} = \boldsymbol{J}_{\mathrm{s}} + \nabla \times \boldsymbol{H}_{\mathrm{c}}\,, \tag{5}$$

where $\boldsymbol{J}_{\mathrm{s}} = (N i_{\mathrm{coil}}/S_{\mathrm{coil}})\boldsymbol{e}_{\theta}$ is the circumferential source current in the pickup coil with N turns, cross-sectional area S_{coil} and current i_{coil} (nonzero only in the coil), κ is the electrical conductivity of the parts modeled as solid conductors (nonzero only in the permanent magnets and caps shown in Fig. 4). $\boldsymbol{H}_{\mathrm{c}}$ is the coercive field of the permanent magnets (nonzero only in the magnets). The electric circuit interface is added to compute the current and voltage across the load resistance R_{load}. The coil internal resistance ($R_{\mathrm{coil}} = 32.6\ \Omega$) is given as a parameter and the coil current i_{coil} is computed from the partial derivation of the vector potential $\boldsymbol{A}$ in the coil as

$$\begin{aligned} \phi &= N \oint_{\mathrm{c}} \boldsymbol{A} \cdot d\boldsymbol{l} \\ \frac{\partial \phi}{\partial t} &= -(R_{\mathrm{coil}} + R_{\mathrm{load}}) i_{\mathrm{coil}} \end{aligned}\,, \tag{6}$$

where c is the domain where line integral is computed and ϕ is the total flux linkage of the coil with N turns. The tangential components of the magnetic vector potential $\boldsymbol{A}$ are fixed to zero at the outer boundaries and the displacements perpendicular to the $x = 0$, $y = 0$ and $z = 0$ planes are fixed to zero as seen from Fig. 4. The Backward-Euler method is used for time integration of the Ampere's law, and the resulting discretized non-linear algebraic equation system is solved using the Newton-Raphson iteration.

4. Results

The magnetization curves (B–H) obtained during the characterization of the material in Section 2.1 are fitted to the analytical expression (1). The result of the fitting to the measured B–H curves at preload values ranging from 20 to 50 MPa is presented in Fig. 5. Owing to very low hysteresis losses discussed in [2] and [5], the fitting is done using a single valued B–H curve obtained by averaging the major hysteresis loop in the H-direction. The values of the fitting parameters α_i, β_i and γ_i for $\eta_\alpha = 11$, $\eta_\beta = 1$ and $\eta_\gamma = 2$ are presented in the Table. 1.

For the energy harvester setup discussed in Section 2.2, 3D FE simulations are carried out changing the operating conditions (magnetic bias and preload) to validate the model and its implementation in COMSOL. As discussed earlier, the output power of the energy harvester is governed by the choice of load resistance and available mechanical excitation. Quite often, we do not have control over the load or the amplitude or frequency of mechanical vibration (ambient vibrational sources). Therefore, for the sake of comparison with the measured results in [5], all simulations are done keeping constant load resistance ($R_{\mathrm{load}} = 160\ \Omega$), peak amplitude of vibrations ($\Delta\sigma = 8$ MPa) and the excitation frequency of 100 Hz.

The simulated results are computed by varying the preload (σ) ranging from 20 to 80 MPa for both the cases Yoke#A and Yoke#B. The applied preload changes the magnetic bias in the magnetic circuit for both cases. The influence of changing preload and magnetic bias on the average output power is presented in Fig. 6.

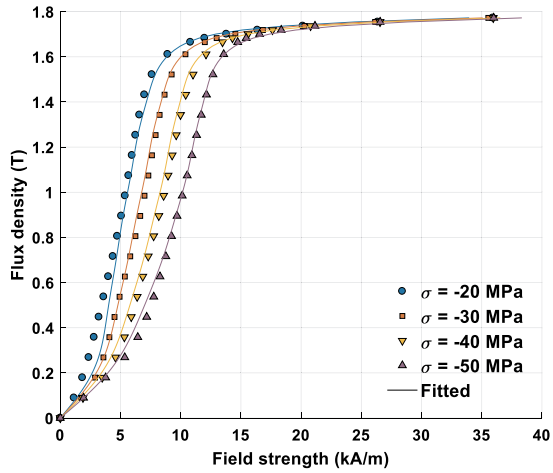

Fig. 5. Measured and fitted magnetization curves under different values of static compressive preload (σ).

Table 1
Coefficients of the fitting parameters.

Parameter	Value (J/m^3)	Parameter	Value (J/m^3)
α_1	6.89×10^3	α_8	-1.63×10^4
α_2	-1.72×10^4	α_9	3.80×10^3
α_3	4.51×10^4	α_{10}	-509.9
α_4	-8.08×10^4	α_{11}	29.89
α_5	9.79×10^4	β_1	-1.76×10^6
α_6	-8.03×10^4	γ_1	8.13×10^9
α_7	4.44×10^4	γ_2	-1.76×10^5

Since we are mainly interested in determining the optimal operating conditions yielding maximum power, the simulation is done for the specific preload range (20–80).

The maximum power in both simulated and measured results is obtained at 45 MPa for Yoke#A and 55 MPa for Yoke#B. The comparison among the mean values of the measured and simulated magnetic field H_{air} computed near the middle part of sample for Yoke#A and Yoke#B and average power for Yoke#A is presented in Fig. 7(a) and (b), respectively. The influence of preload over simulated magnetic flux density inside the bar (B_{bar}) and average power for Yoke#B is presented in Fig. 7(c). The results from Fig. 7(c) indicate that the permeability of the material decreases by increasing preload and the maximum power is obtained at 55 MPa. The results from Figs. 6 and 7 illustrate that there exists an optimal value of preload and magnetic bias for each specific case (Yoke#A and Yoke#B) resulting in maximum output power. In addition, the simulated results are in reasonable agreement with the measurements for the range of 20–50 MPa for which the fitting has been done. The difference among measured and simulated results increases for higher stress values which is evident from Figs. 6 and 7. This difference is because, the model overestimates the relative permeability of the material for the range of 60–80 MPa. This causes smaller simulated magnetic field in the air (H_{air}) as compared to measured one. The overestimation of the relative permeability of the material results in larger values of the simulated power. Moreover, the simulation does not account for the small air gaps due to manufacturing tolerances between the solid cap, core and bar, which

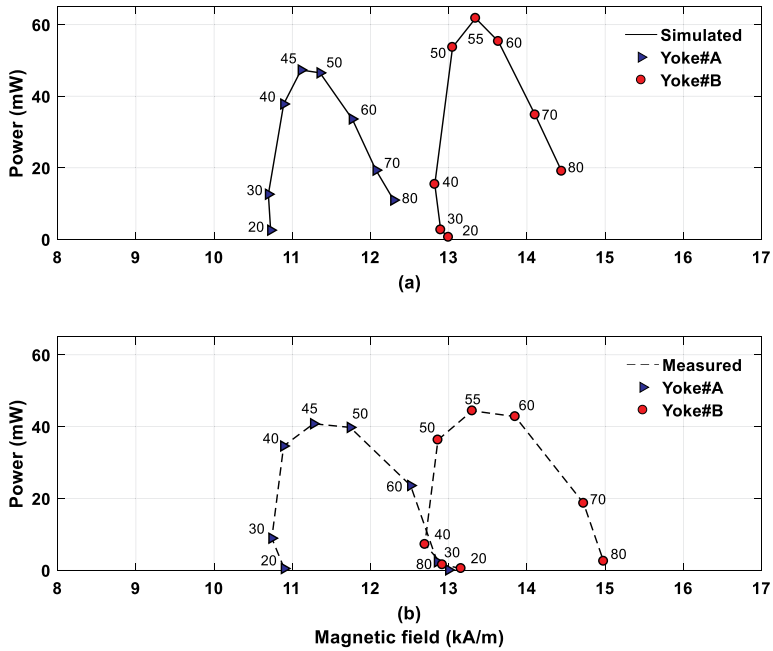

Fig. 6. Comparison among simulated (a) and measured (b) output power using R_{load} of 160 Ω, dynamic load of 8 MPa for different preload values in two different cases (Yoke#A and Yoke#B). The vibration freqeuncy is 100 Hz.

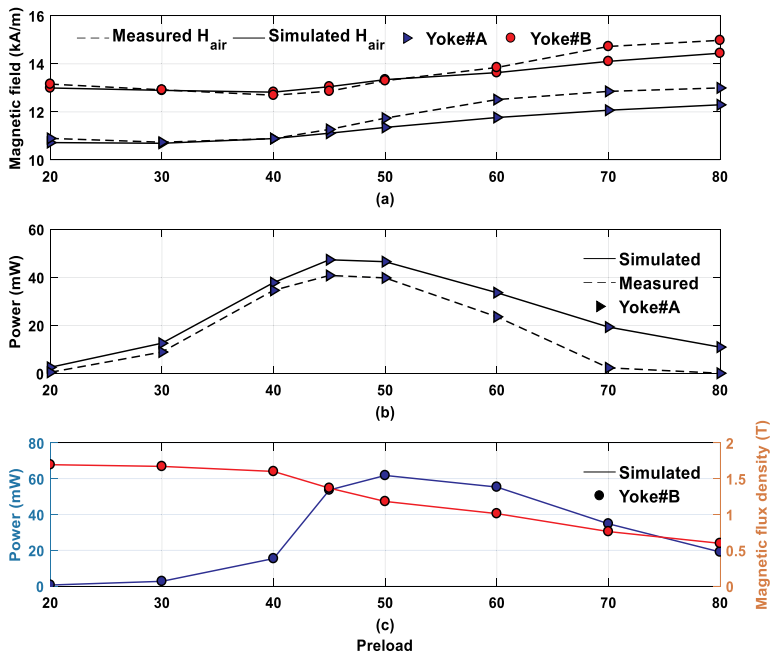

Fig. 7. Comparison among measured and simulated magnetic field H_{air} (a) and average powers with respect to changing preload (b). The simulated results of magnetic flux density B_{bar} and average power with respect to changing preload (c).

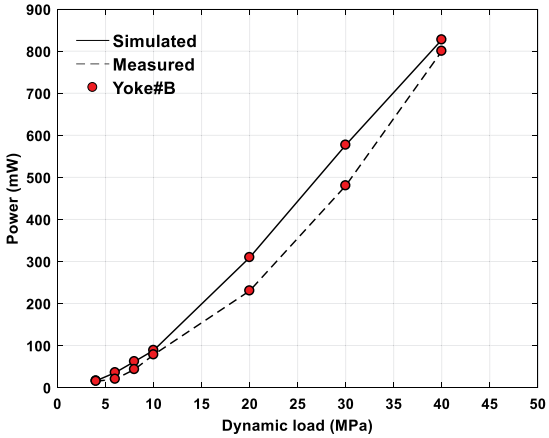

Fig. 8. Measured and simulated output power for various dynamic loading cases. The results are presented for the case of Yoke#B using constant preload of 55 MPa and vibrational frequency of 100 Hz.

decreases the reluctance of the magnetic circuit causing an increase in simulated power. Furthermore, the experimental results are affected by a measurement uncertainty, due to the accuracy of the field meter and due to the measurement repeatability [5] being anyway limited to few percent. Thus, the comparison among measured and simulated results should be made taking into account the uncertainty of the experimental results and model limitations.

The influence of increasing the dynamic load on the output power is studied by varying the $\Delta\sigma$ from 4 MPa to 40 MPa for the case of Yoke#B using a constant preload of 55 MPa. The comparison among measured and simulated results is presented in Fig. 8. It is evident from the figure that the output power increases with the increase in dynamic load. However, the simulated results show larger output power than measured results following the same trend.

5. Discussion and conclusion

This paper presents successful implementation of a magneto-mechanical constitutive law utilizing thermodynamic approach into a 3D FE model using commercially available COMSOL software. The model is validated by comparing the simulated and measured results for an energy harvester setup. The simulated results indicate that the model can reasonably predict the output power for the fitting range presented in Fig. 5. In addition, the model could also predict the optimal preload value and magnetic bias yielding maximum power.

The model contains several parameters which are not known accurately. The main parameters are the remanence flux density of the magnets, the permeability of the magnetizing core and the length of the small airgaps between the core, the caps and the galfenol rod. Changing these parameters will change the magnetic field $\boldsymbol{H}$ next to the bar. In order to compare the simulations and the measurements, we have tuned the remanence flux density of the magnets so that the simulated $\boldsymbol{H}$ value matches the measured $\boldsymbol{H}$ value in the case of preload yielding maximum output power. The airgaps between the core, the caps and the galfenol rod were not considered in the simulations. Tuning the parameters by directly matching the measured and simulated output powers would not be possible during practical design and was thus not attempted.

Although the model reasonably describes the behavior of the studied devices, differences between the modeled and measured results are observed under some cases, particularly where the preload stress is above 60 MPa. These differences are associated with the measurement uncertainties and limitations of the model. In particular, the measurements were found to be sensitive to the vertical loading system of machine. These effects cause small discrepancies in the measurements. Moreover, the model can reasonably follow the trend of the measured results but is unable to accurately predict the results outside the range of data used for the fitting.

The simulated results validate that, indeed there exists an optimal value of preload and magnetic bias resulting in maximum power. Tuning the external operating conditions (magnetic bias, preload, load resistance frequency and amplitude of vibrations) is important for the design and application prospective for the energy harvester. The proposed modeling approach can be applied to analyze a magneto-mechanical energy harvester and determine the optimal design characteristics and operating conditions.

References

[1] V. Berbyuk, 2013, Vibration energy harvesting using Galfenol-based transducer. In: Active and Passive Smart Structures and Integrated Systems 2013 (Vol. 8688, p. 86881F). International Society for Optics and Photonics.
[2] C.S. Clemente, A. Mahgoub, D. Davino, C. Visone, Multiphysics circuit of a magnetostrictive energy harvesting device, J. Intell. Mater. Syst. Struct. 28 (17) (2017) 2317–2330.
[3] D. Davino, P. Krejčí, C. Visone, Fully coupled modeling of magneto-mechanical hysteresis through thermodynamic compatibility, Smart Mater. Struct. 22 (9) (2013) 095009.
[4] B. Rezaeealam, Finite element analysis of magnetostrictive vibration energy harvester, COMPEL-Int. J. Comput. Math. Electr. Electr. Eng. 31 (6) (2012) 1757–1773.
[5] S. Palumbo, P. Rasilo, M. Zucca, Experimental investigation on a Fe-Ga close yoke vibrational harvester by matching magnetic and mechanical biases, J. Magn. Magn. Mater. 469 (2019) 354–363.
[6] J. Atulasimha, A.B. Flatau, A review of magnetostrictive iron–gallium alloys, Smart Mater. Struct. 20 (4) (2011) 043001.
[7] P.G. Evans, M.J. Dapino, Dynamic model for 3-D magnetostrictive transducers, IEEE Trans. Magn. 47 (1) (2010) 221–230.
[8] S. Chakrabarti, M.J. Dapino, Coupled axisymmetric finite element model of a hydraulically amplified magnetostrictive actuator for active powertrain mounts, Finite Elem. Anal. Des. 60 (2012) 25–34.
[9] U. Ahmed, J. Jeronen, M. Zucca, S. Palumbo, P. Rasilo, Finite element analysis of magnetostrictive energy harvesting concept device utilizing thermodynamic magneto-mechanical model, J. Magn. Magn. Mater. 486 (2019) 165275.
[10] K. Fonteyn, A. Belahcen, R. Kouhia, P. Rasilo, A. Arkkio, FEM for directly coupled magneto-mechanical phenomena in electrical machines, IEEE Trans. Magn. 46 (8) (2010) 2923–2926.

PUBLICATION III

3-D Magneto-Mechanical Finite Element Analysis of Galfenol-Based Energy Harvester Using an Equivalent Stress Model

U. Ahmed, U. Aydin, L. Daniel and P. Rasilo

IEEE Transactions on Magnetics 57.2 (2021)
DOI: 10.1109/TMAG.2020.3011875

3D Magneto-Mechanical Finite Element Analysis of Galfenol-Based Energy Harvester Using an Equivalent Stress Model

U. Ahmed[1], U. Aydin[2], L. Daniel[3,4], P. Rasilo[1]

[1]Unit of Electrical Engineering, Tampere University, FI-33720 Tampere, Finland
[2]ABB Oy, Marine and Ports, FI-00980, Helsinki, Finland
[3]Université Paris-Saclay, CentraleSupélec, CNRS, Laboratoire de Génie Electrique et Electronique de Paris, 91192, Gif-sur-Yvette, France.
[4]Sorbonne Université, CNRS, Laboratoire de Génie Electrique et Electronique de Paris, 75252, Paris, France

This paper presents the implementation of an equivalent stress model to analyze a Galfenol-based magneto-mechanical energy harvesting concept device. The equivalent stress approach can transform any arbitrary stress tensor into a uniaxial stress acting along the direction of the magnetic flux density. Unlike multiaxial magneto-mechanical phenomenological models, it offers simple implementation to predict the permeability change by interpolation from uniaxial measurements. For the first time, the proposed model is implemented in a 3D finite element solver using COMSOL Multiphysics software to analyze an energy harvesting setup, where the effect of mechanical preload and magnetic bias on the output power can be studied. The model is tested under different compressive loading cases ranging 20 – 80 MPa, and the simulated results are compared with the measurement results for validation. The results show that the approach can successfully be used as a tool to analyze the behavior of the harvester device and to determine the optimal design parameters.

***Index Terms*— Constitutive laws, energy harvesting, magnetoelasticity, magnetostriction, strain, stress.**

I. Introduction

ANALYSIS and design of magnetostrictive energy harvesters have been widely studied in the past decade. The energy harvesters allow conversion of mechanical vibration energy into electrical energy originating from ambient vibrational sources such as buildings, bridges, rail tracks or moving parts of machines. Such harvesters can be employed at remote locations to power up wireless sensor nodes or small-scale electronic devices [1]. After the discovery of giant magnetostrictive materials (Galfenol, Terfenol-D and Metglas etc.), the research on magnetostrictive energy harvesting has predominantly increased and various prototype devices have been introduced as proofs of concept [2], [3].

The amount of harvested power is influenced by the operating conditions (mechanical preload and magnetic bias) and design characteristics (amplitude and frequency of vibration, device geometry and magnetic closure circuit etc.). Modeling tools are required to analyze and design such devices and determine the influence of design parameters on device performance. In addition, due to 3D multiaxial nature of magnetic field and mechanical stress, the analysis of such devices becomes quite complex [4].

Various researches have been done to model the magneto-mechanical effects of the magnetostrictive harvesters using phenomenological models [2], [3] and [5]. Such models are based on deriving a more or less empirical analytical expression for the constitutive equations defining the magneto-elastic behavior of the material. Finding a practical analytical expression which sufficiently replicates the magneto-elastic behavior is difficult. Indeed, fully coupled non-linear models are promising but complicated to implement. In addition, the analytical expression might need to be changed when the state variables change.

This paper proposes to use an equivalent stress model presented in [6] for 3D magnetodynamic analysis of a magneto-mechanical energy harvester concept device. The equivalent stress model is tested for the first time in an energy harvesting application. It offers a simple and straightforward approach that only requires measurements from the uniaxial stress dependent magnetization curves (*B-H* curves). The model is implemented in COMSOL Multiphysics software for 3D finite element (FE) simulations. The paper also discusses and compares the results against the thermodynamic modeling approach developed and tested in [7]. The idea is to test how these models can be utilized for the analysis of the energy harvesting device. The simulated results from both models are compared with measurement results for validation.

II. Experimental Methods

In order to validate the modelling approach and to analyze the energy harvesting device, an experimental setup is developed and tested as discussed in [8]. The experimental setup is divided into two parts. The stress-dependent magnetization curves are obtained to characterize the active material (Galfenol) in the first part, whereas the second part is developed for testing the actual energy harvester setup. The measurement principles are summarized in this section, while a detailed description of both setups can be found in [7].

A. Material Characterization

The characterization of Galfenol is performed first to obtain the magnetization curves (*B-H* curves) under various static preload (σ) values. A cylindrical Galfenol rod of 60 mm in length and 12 mm in diameter is utilized as the active material for the harvester. In order to obtain the stress dependent *B-H* curves, the Galfenol rod is first magnetized with the help of two U-shaped cores and two coils supplied by 200 mHz AC

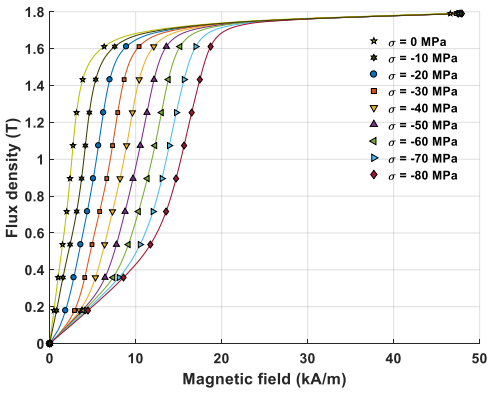

Fig. 1. Measured *B*-*H* curves produced from material charaterization at different mechanical preload (σ) values.

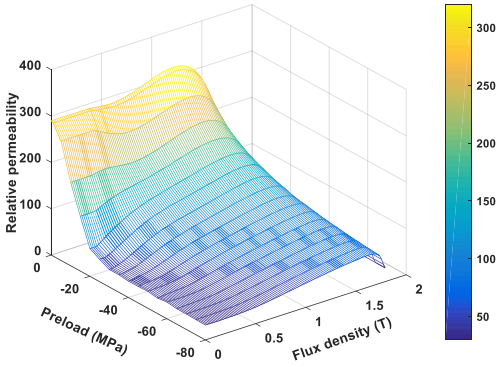

Fig. 2 Relative permeability vs. magnetic flux density at different mechanical preload (σ) values.

voltage. The rod is then subjected to various static uniaxial compressive preloads σ ranging 0 – 80 MPa with a step of 5 MPa. The magnetic field strength H is measured using a Hall probe placed at the middle part of the sample and the magnetic flux density B is obtained by integrating the voltage induced in the pickup coil wound around the sample. Since only anhysteretic material models are considered, single-valued magnetization properties are extracted by averaging the ascending and descending branches of the measured hysteresis loops in the H-direction. The characterization produces a set of magnetization curves $B(H)$ as a function of the static uniaxial stress σ presented in Fig. 1, from which we can interpolate the permeability as $\mu(B, \sigma)$ as shown in Fig. 2.

B. Energy harvester setup

The schematic diagram of the prototype energy harvester setup is presented in Fig. 3 (a). In this setup, the Galfenol rod is magnetized with the help of cylindrical NdFeB permanent magnets and four L-shaped cores as shown in Fig. 3 (b). The magnets have physical dimensions of 12 mm in diameter and

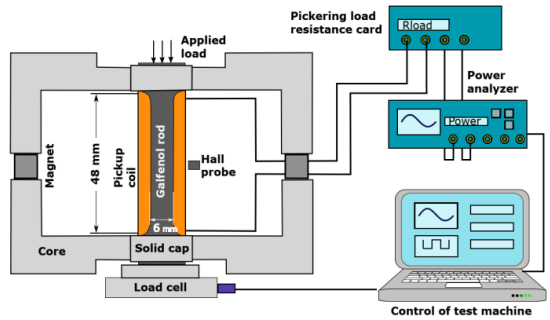

(a)

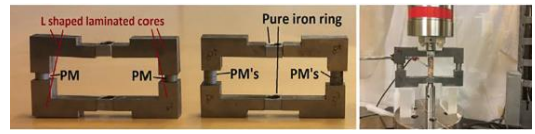

Setup#A Setup#B Actual setup

(b)

Fig. 3. Schematic diagram of the energy harvester setup (a) and the actual setup (b) with both configurations Setup#A (2 magnets) and Setup#B (4 magnets).

6 mm in thickness with a remanence flux density of B_r = 1.1 T and coercivity of H_c = 995 kA/m and produce a magnetic bias into the sample. The Galfenol rod is machined to reduce the diameter of the sample to 6 mm from the middle for the length of 48 mm as seen from Fig. 3 (a). A pickup coil consisting of 2000 turns of 0.2 mm wire is wound around the machined sample. Since the test machine could exert a maximum sinusoidal force of 7 kN rms (10 kN peak), machining the sample allowed us to operate at large range of stress values. A programmable precision load resistance card PXI 40-297-002 is connected to the pickup coil as variable load resistance to measure the output power.

To analyze the effect of magnetic bias, two different magnetizing configurations were studied (Fig. 3 (b)). Setup#A contains one permanent magnet (PM) at each column of the L-shaped core (2 magnets in total) whereas Setup#B has 2 magnets (PM's) on each column (4 magnets in total). For the energy harvester setup, the Galfenol rod is first subjected to a static compressive preload σ followed by sinusoidal dynamic load $\Delta\sigma$ of 8 MPa at 100 Hz vibration frequency. The application of the dynamic load causes an induced voltage in the pickup coil due to Villari effect and Faraday's law. Finally, the output power supplied to the load resistance of 160 Ω is measured.

The experiment is repeated for various mechanical preload σ values ranging from 20 – 80 MPa keeping the dynamic load $\Delta\sigma$ and vibration frequency constant. The same experiment is repeated for both configurations Setup#A and Setup#B to determine the effect of mechanical preload and magnetic bias over the output power. The aim of this paper is to test the equivalent stress model to predict the output power as a function of mechanical preload and magnetic bias and

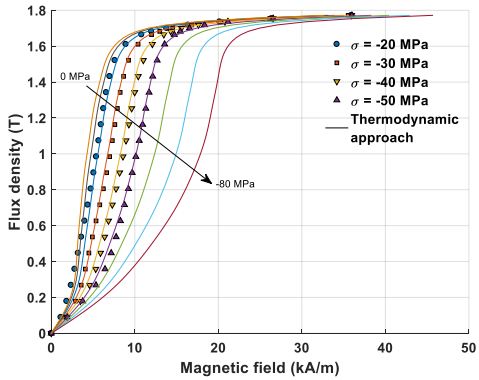

Fig. 4. Simulated magnetization curves under mechanical preload values of 0, -10, …, -80 MPa using the thermodynamic approach. The markers denote the measurements used for fitting the model.

compare the results with the measurements obtained from the harvester.

III. Models

A. Equivalent stress model

The idea of equivalent stress models is to utilize the permeability data $\mu(B, \sigma)$ obtained from the uniaxial measurements to interpolate the correct permeability for a combination of an arbitrary flux-density vector $\boldsymbol{B}$ and stress tensor $\boldsymbol{\sigma}$. This is done by converting the stress tensor into an equivalent uniaxial stress σ_{eq} along the direction of the magnetic flux density in such a way that similar macroscopic magneto-elastic behavior of the material is obtained. The complete derivation of the equivalent stress/strain model is presented in [6]. The magnetic flux density vector is written as $\boldsymbol{B} = B\boldsymbol{b}$, where B is the magnitude and $\boldsymbol{b}$ the direction vector. The equivalent stress in terms of magneto-elastic energy can be written as

$$\sigma_{\mathrm{eq}} = \frac{3}{2}\boldsymbol{b}^{\mathrm{T}}\boldsymbol{s}\boldsymbol{b}\,, \tag{1}$$

where $\boldsymbol{s} = \boldsymbol{\sigma} - \frac{1}{3}\mathrm{tr}(\boldsymbol{\sigma})\boldsymbol{I}$ is the deviatoric part of the stress tensor $\boldsymbol{\sigma}$, and $\boldsymbol{I}$ is the identity matrix.

B. Thermodynamic magneto-mechanical model

In addition to measurements, the equivalent stress approach is compared with a COMSOL implementation of a thermodynamic modeling approach discussed in [7]. In brief, a fully 3D directly-coupled multiaxial magneto-mechanical model is obtained by analytically expressing a Helmholtz free energy as a function of the magnetic flux-density vector $\boldsymbol{B}$ and strain tensor $\boldsymbol{\varepsilon}$ as

$$\psi\left(\boldsymbol{B},\boldsymbol{\varepsilon}\right) = \frac{1}{2}\lambda I_1^2 + \mu I_2 + \sum_{i=1}^{\eta_\alpha}\alpha_i I_4^i + \sum_{i=1}^{\eta_\beta}\beta_i I_5^i + \sum_{i=1}^{\eta_\gamma}\gamma_i I_6^i\,, \tag{2}$$

where $I_1 = \mathrm{tr}(\boldsymbol{\varepsilon})$, $I_2 = \mathrm{tr}(\boldsymbol{\varepsilon}^2)$, $I_4 = \boldsymbol{B}\cdot\boldsymbol{B}$, $I_5 = \boldsymbol{B}\cdot\boldsymbol{\varepsilon}\boldsymbol{B}$ and $I_6 = \boldsymbol{B}\cdot\boldsymbol{\varepsilon}^2\boldsymbol{B}$, λ and μ are Lamé parameters obtained from Young's modulus and Poisson's ratio, and α_i, β_i and γ_i are fitting parameters. The magnetic field strength vector $\boldsymbol{H}$ and stress tensor $\boldsymbol{\sigma}$ are obtained by partial differentiation of the free energy density as

$$\boldsymbol{H}\left(\boldsymbol{B},\boldsymbol{\varepsilon}\right) = \left(\frac{\partial\psi}{\partial\boldsymbol{B}}\right)^{\mathrm{T}} \text{ and } \boldsymbol{\sigma}\left(\boldsymbol{B},\boldsymbol{\varepsilon}\right) = \frac{\partial\psi}{\partial\boldsymbol{\varepsilon}}\,. \tag{3}$$

In order to obtain the material parameters α_i, β_i and γ_i, the magnetization curves obtained from (3) are fitted against the uniaxial measurement $H(B, \sigma)$ for the mechanical preload range 20 to 50 MPa for $\eta_\alpha = 11$, $\eta_\beta = 1$ and $\eta_\gamma = 2$. The *B*-*H* curves produced by the thermodynamic model in the range of 0 – 80 MPa are presented in Fig. 4. A relatively good fitting can be achieved in a narrow stress range, but outside of the fitting data range (below 20 MPa and above 50 MPa), the simulated results deviate from the measurements shown in Fig. 1.

IV. Finite Element Model

The analytical expression of the equivalent stress σ_{eq} is implemented in COMSOL Multiphysics software for 3D FE simulation of the prototype device discussed in Section II B. Due to symmetry reasons, modeling 1/8th of the geometry is sufficient. At first step, a purely mechanical simulation with linear elasticity is performed to calculate the stress distribution in the Galfenol rod by solving $\nabla\cdot\boldsymbol{\sigma} = 0$ with the applied load imposed as a Neumann boundary condition on the top of the rod. The stress tensor only includes the stress from the mechanical loading written as $\boldsymbol{\sigma} = \mathbf{C}{:}\varepsilon$ where $\mathbf{C}$ is the 4th order mechanical stiffness tensor and $\boldsymbol{\varepsilon}$ is the pure elastic strain tensor.

At second step, an electromagnetic simulation is performed which uses the equivalent stress model for the permeability as the constitutive law as $\boldsymbol{H}(\boldsymbol{B}, \boldsymbol{\sigma}) = \boldsymbol{B} / \mu(\|\boldsymbol{B}\|, \sigma_{\mathrm{eq}})$, where $\boldsymbol{B} = \nabla\times\boldsymbol{A}$. The COMSOL utilizes the local permeability $\mu(\|\boldsymbol{B}\|, \sigma_{\mathrm{eq}})$ interpolated from the uniaxial permeability measurements shown in Fig. 2. In the actuator material, the combination of Ampere's and Faraday's laws is solved in terms of the magnetic vector potential $\boldsymbol{A}$ as

$$\nabla\times\boldsymbol{H}(\boldsymbol{B},\boldsymbol{\sigma}) + \kappa\frac{\partial\boldsymbol{A}}{\partial t} = 0\,, \tag{4}$$

where κ denotes the electrical conductivity. In the other regions, a purely electromagnetic problem is solved as

$$\nu\nabla\times\nabla\times\boldsymbol{A} + \kappa\frac{\partial\boldsymbol{A}}{\partial t} = \boldsymbol{J}_{\mathrm{s}} + \nabla\times\boldsymbol{H}_{\mathrm{c}}\,, \tag{5}$$

where ν is the constant reluctivity. The circumferential source current density in the pickup coil of N turns is $\boldsymbol{J}_{\mathrm{s}} = (Ni_{\mathrm{coil}}/S_{\mathrm{coil}})\boldsymbol{e}_\theta$, where i_{coil} and S_{coil} are the coil current and coil cross-section area. The electrical conductivity κ is nonzero only in the permanent magnets and the solid caps connecting the rod and core (Fig. (3a)), while $\boldsymbol{H}_{\mathrm{c}}$ is the coercive field of

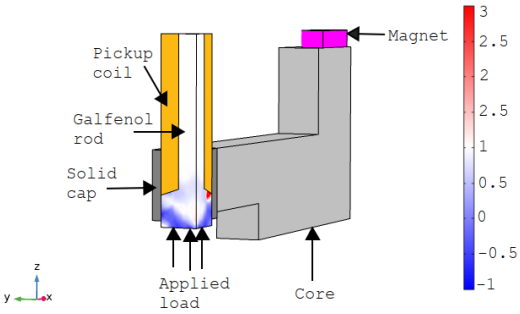

Fig. 5. Distribution of the stress ratio σ_{eq} / σ_{zz} in the Galfenol rod.

the magnets.

The power flow from the pickup coil to the load resistance is modeled using the electric circuit interface in COMSOL, calculating the pickup coil current from

$$\frac{N}{S_{\text{coil}}}\int_{V_{\text{coil}}}\frac{\partial A_\theta}{\partial t}dV+\left(R_{\text{coil}}+R_{\text{load}}\right)i_{\text{coil}}=0\,, \tag{6}$$

where R_{coil} = 32.6 Ω is the coil resistance, and the first term represents the back-emf computed by averaging the time derivative of the circumferential component of the vector potential over all possible paths in the coil volume V_{coil}. The time integration is done using Backward-Euler method, and the resulting nonlinear system is solved using the Newton-Raphson iteration. The implementation of the thermodynamic model in COMSOL Multiphysics software for 3D FE simulation is discussed in [7].

V. Results and Discussions

Due to the axial loading, the stress in the whole Galfenol rod is mainly uniaxial, so that the zz-component dominates. In the middle part of the rod, the flux density is oriented parallel to the stress. However, near the end of the rod, the flux density turns towards the core, causing the magneto-mechanical problem to become multiaxial. This is seen in Fig. 5, where the distribution of the ratio σ_{eq} / σ_{zz} between the equivalent stress and the zz-component of the stress tensor is visualized. Using the equivalent stress model for correctly interpolating the permeability in the regions close to the core is thus justified.

The energy-harvesting simulations are carried out using a load resistance of 160 Ω at a constant dynamic load $\Delta\sigma$ = 8 MPa and mechanical vibration frequency of 100 Hz. The influence of operating conditions (mechanical preload and magnetic bias) over the output power is simulated by varying the operating conditions. The simulated results are compared with the measured ones for validation. The results are simulated for the preload range of 20 – 80 MPa since we are mainly interested in the range where we obtain the maximum output power.

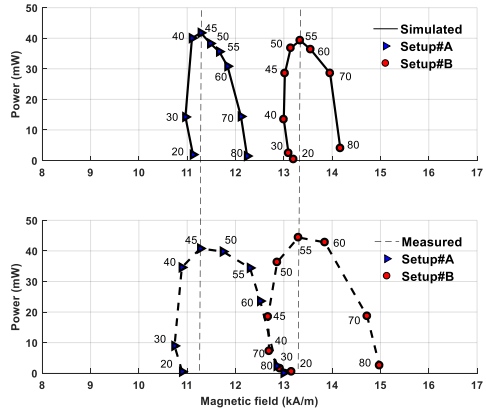

Fig. 6. Measured and simulated output power for different mechanical preload values and the effect of preload over magnetic bias.

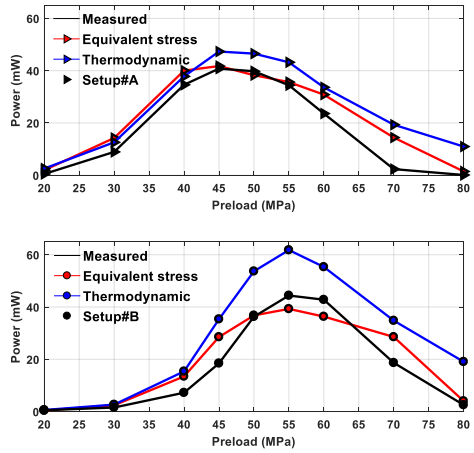

Fig. 7. Measured and simulated average output power at varying operating conditions using both equivalent stress and thermodynamic modeling approach.

It was observed that the output power is very sensitive to variations in the magnetic bias and changes significantly if the magnetic field bias changes slightly under a constant mechanical preload. It is difficult to predict the magnetic bias accurately with the FE model due to the existence of small clearances between the cores and the sample and the inaccuracies in modeling the magnetization properties of the core, which affect the total reluctance of the flux path. In order to allow a reasonable comparison of the output powers under different mechanical preloads, the remanence flux density of the permanent magnets is tuned so that the magnetic field near the middle part of the sample matches the field measured with the Hall-probe under the mechanical preload value at which the maximum output power is obtained. The remanence is then kept constant when other mechanical preload values are

simulated. The influence of the mechanical preload on the magnetic bias as well as the sensitivity of the output power to the magnetic bias can be seen from Fig. 6. The tuning is done for the preload value of 45 MPa for Setup#A and 55 MPa for Setup#B indicated by vertical dashed lines. The magnetic bias changes due to the applied preload which is evident from both measured and simulated results in Fig. 6.

For both the models, the comparison among measured and simulated average output powers for both configurations of the harvester setups (Setup#A and Setup#B) is presented in Fig. 7. The results indicate that the equivalent stress model can predict the output power with reasonable accuracy. The simulated results are consistent with the measured results with peak power occurring at 45 MPa for Setup#A and 55 MPa for Setup#B.

For comparison, the results obtained from the directly-coupled COMSOL Multiphysics implementation of the thermodynamic constitutive model described in [7] are presented in Fig. 7. The model predicts slightly larger values as compared to measured ones but can correctly estimate the mechanical bias at which maximum power is obtained. Moreover, the simulated results follow similar trends of the measurement results where the maximum power occurs at 45 MPa for Setup#A case and 55 MPa for Setup#B.

The limitation of the thermodynamic modeling technique is that it is unable to properly fit to the measured magnetization curves for wide range of static mechanical preload cases. The discrepancies can be seen by comparing the measured and simulated *B-H* curves in Fig. 1 and 4, respectively. The simulated results vary by the choice of the σ values used when fitting the model, as well as the degree of polynomial coefficients for parameters α, β and γ. The limitation of the equivalent stress model is that it does not consider the stress due to magnetostriction and thus the total simulated stress is less than the actual stress which affects the simulated magnetic field bias as seen from Fig. 6.

The difference between measured and simulated results can be explained by the limitations of the models and partly due to the uncertainty and repeatability of the measurements. The measurements were found sensitive to the warm-up time and alignment of the harvester to the vertical loading system. These parameters affect the repeatability of the measurements and must be kept constant.

VI. Conclusion

In this paper, the equivalent stress model is successfully implemented and tested for an energy harvester setup. The 3D FE simulations are carried out using commercially available software COMSOL Multiphysics, and the simulated results are compared with measurement results for validation. The results show that the model can successfully predict the maximum output power and mechanical preload and thus can be employed to analyze the harvester device.

The simulated results from the equivalent stress model are also compared with those from a directly-coupled FE model implemented using a thermodynamic approach. The main advantage of the equivalent stress model is that, unlike in the thermodynamic approach, there are no free parameters that would require fitting against measured *B-H* curves and the model is quite simple to implement.

Since the energy harvesters are excited by ambient vibration sources, the excitation amplitude and frequency cannot be controlled. The equivalent stress model can provide the knowledge of the optimal operating conditions (mechanical preload and magnetic bias), which can be tuned to design the harvester geometry tailored to the specific application (powering wireless sensor node or RF tag etc.). We are mainly interested in the preload range (45 – 60 MPa) where the studied material provides the maximum output power density. In this stress region, the accuracy of the equivalent stress model is sufficient.

The uncertainties related to material properties and manufacturing tolerances makes it difficult to accurately predict the magnetic bias using the FE models. This is not necessarily a major problem for engineering design, thanks to the dependency of optimal mechanical preload on the magnetic bias [8]. If the magnetic bias in a manufactured energy harvester differs from the design value, the mechanical preload can be adjusted to change the operation point so that the maximum output power is obtained.

References

[1] L. Wang and F. G. Yuan, "Vibration energy harvesting by magnetostrictive material," *Smart Materials and Structures*, Vol. 17, No. 4, p.045009, 2008.

[2] Clemente, C. Stefano, and D. Davino, "Modeling and Characterization of a Kinetic Energy Harvesting Device Based on Galfenol," *Materials*, Vol. 12, No 19, p.3199, 2019.

[3] Clemente, C. Stefano, A. Mahgoub, D. Davino and C. Visone, "Multiphysics circuit of a magnetostrictive energy harvesting device," *Journal of Intelligent Material Systems and Structures*, Vol 28, No. 17, pp.2317-2330, 2017.

[4] C. Mudivarthi, S. Datta, J. Atulasimha, and A. Flatau, "A bidirection-ally coupled magnetoelastic model and its validation using a Galfenol unimorph sensor," *Smart Materials and Structures*, Vol. 17, No. 3, 2008.

[5] B. Rezaeealam, "Finite element analysis of magnetostrictive vibration energy harvester," COMPEL- The international journal for computationand mathematics in electrical and electronic engineering, Vol. 31, No. 6 pp. 1757–1773, 2012

[6] O. Hubert and L. Daniel, "Energetical and multiscale approaches for the definition of an equivalent stress for magneto-elastic couplings," *Journal of Magnetism and Magnetic Materials*, Vol. 323, No. 13, p.1766-1781. 2011.

[7] U. Ahmed, U. Aydin, M. Zucca, S. Palumbo, R. Kouhia and P. Rasilo, "Modeling a Fe-Ga Energy Harvester Fitted with Magnetic Closure Using 3D Magneto-Mechanical Finite Element Model," *Journal of Magnetism and Magnetic Materials*, Vol. 500, No. 15, p.166390, 2020.

[8] S. Palumbo, P. Rasilo and M. Zucca, "Experimental investigation on a Fe-Ga close yoke vibrational harvester by matching magnetic and mechanical biases," *Journal of Magnetism and Magnetic Materials*, Vol. 469, pp.354-363, 2019.

PUBLICATION IV

Validation of Thermodynamic Magneto-Mechanical Finite-Element Model on Cantilever-Beam Type Magnetostrictive Energy Harvester

U. Ahmed, D. Blažević, Y. Mizukawa, U. Aydin and P. Rasilo

Journal of Magnetism and Magnetic Materials 564 (2022)
DOI: 10.1016/j.jmmm.2022.170098

Journal of Magnetism and Magnetic Materials 564 (2022) 170098

Contents lists available at ScienceDirect

Journal of Magnetism and Magnetic Materials

journal homepage: www.elsevier.com/locate/jmmm

Validation of thermodynamic magneto-mechanical finite-element model on cantilever-beam type magnetostrictive energy harvester

U. Ahmed [a,*], D. Blažević [a], Y. Mizukawa [a], U. Aydin [b], P. Rasilo [a]

[a] Tampere University, Electrical Engineering Unit, P.O. Box 692, FI-33720 Tampere, Finland
[b] ABB Oy, Motion Services, P.O. Box 210, FI-00381 Helsinki, Finland

ARTICLE INFO

Keywords:
Energy harvesting
Finite element analysis
Galfenol
Magneto-elasticity
Magnetostrictive devices
Villari effect

ABSTRACT

This paper presents the validation of a thermodynamic magneto-mechanical model to analyze a galfenol based cantilever beam type energy harvesting device. As compared to some earlier modeling approaches that were tested only on specific harvester geometries, the thermodynamic model has already been validated on rod-type harvesters and is now shown to be suitable for analyzing also beam-type devices. Moreover, the paper discusses the influence of magnetostriction upon resonant frequency. The thermodynamic model is implemented in a 3D finite element solver using COMSOL Multiphysics software. This allows optimizing the device design by tuning the geometric parameters and magnetic bias under available operating conditions (amplitude and frequency of vibrations) easily and efficiently. A unimorph cantilever beam type prototype harvester device consisting of a galfenol beam bonded to an aluminum substrate is constructed for validating the model. Simulated and measured results are compared at base excitation amplitudes of 0.5 to 2 g under varying vibration frequencies. The results show that the maximum induced voltage is obtained at the resonant frequency which decreases slightly with an increase in the vibration amplitude. Furthermore, it is shown that the resonant frequency decreases from 201 Hz to 187 Hz at 1 g base acceleration when the magnetic bias is removed. The comparison of measured and simulated results show that the model can accurately predict the resonant frequency with a relative error of less than 2 %, validating the modeling approach. The model can also reasonably determine the open circuit voltage with some discrepancies at large vibration amplitudes.

1. Introduction

The concept of energy harvesting has seen significant rise in attention during the past decade as the demand for supplying maintenance and battery-free energy increased for wireless sensor nodes and small-scale power electronic devices. Rapid development of ultra-low power microelectronic sensors and integrated circuit manufacturing technology have brought the power requirement levels to tens of microwatts [1], making it possible to power electronic devices with small scale energy harvesting devices. The popular techniques of energy harvesting include piezoelectric, electromagnetic, electrostatic and magnetostrictive energy harvesting [2]. The limitations of piezoelectric harvesters are low mechanical coupling, high level of induced voltage, low output current and shorter lifespan due to mechanical breakdown at higher stress levels [3]. Frequently explored electromagnetic energy harvesters have mesoscale volumes which limits their application in small-scale power electronic devices and makes them more suitable for low frequency operation. Downscaling of this type of harvesters is also more difficult with the usual micromanufacturing techniques [4]. Electrostatic energy harvesters have mechanical limitations and need an external voltage source [4,5]. After the discovery of giant magnetostrictive materials (GMMs) such as galfenol, Terfenol-D and Metglas, the research on magnetostrictive energy harvesting has predominantly increased due to their ability to supply reliable and maintenance free energy. GMMs are rare earth alloys that show large magnetostriction and high energy density. Among GMMs, galfenol offers high tensile strength (~350 MPa), relatively large magnetostriction (200–250 ppm), low hysteresis losses and strong magneto-mechanical coupling [6]. Stefano in [7] has experimentally shown that hysteresis in galfenol-based energy harvesters is negligible. A difference of 1 % was noticed while comparing the two output power curves obtained by subsequently increasing and decreasing the applied magnetic field from 5 kA/m to 40 kA/m under constant mechanical vibrations. More importantly, galfenol is an iron gallium alloy that can be welded and machined easily, making

* Corresponding author.
E-mail address: umair.ahmed@tuni.fi (U. Ahmed).

https://doi.org/10.1016/j.jmmm.2022.170098
Received 18 August 2022; Received in revised form 6 October 2022; Accepted 19 October 2022
Available online 25 October 2022

it a more practical option in structural health condition monitoring applications. Magneto-mechanical energy harvesters utilize ambient vibrations from rotating machinery parts, rail tracks, aircraft wings, steel cable bridges etc. and converts it into electrical energy through the inverse magnetostrictive effect. Magnetostrictive harvesters can also be used as transducers for active vibration control [8] and [9].

The analysis and design of an energy harvesting device require knowledge related to the material characteristics and the operating conditions. Since such harvesters utilize vibrations from ambient sources, the information related to the nature, amplitude and frequency of the vibration is needed in the design process to determine the optimal design parameters and device geometry. The design parameters include choosing the magnetic field bias and coil parameters and constructing the device geometry based on the energy requirement for a specific application. Therefore, modeling tools are needed to analyze the harvester device under typical operating conditions in order to successfully customize the device design to the specific application [5–8].

Various models have been developed to analyze galfenol based energy harvesting devices. Models based on a linearized approach using piezomagnetic constitutive equations are presented in [9] and [10]. These models are simple to implement but incapable of analyzing the material at non-linear regions. A non-linear dynamic model based on Armstrong electro-mechanical constitutive equations is proposed in [11]. The open circuit voltage predicted by the model is higher than the measured one for large excitations (3–4 g, g = 9.81 m/s^2 being the gravitational acceleration) because the model excludes hysteresis losses. Fully coupled dynamic models implemented in finite element (FE) formulations are presented in [12] and [13]. The coupled magneto-mechanical constitutive equations describing the effect of change in magnetic flux density upon stress based on the Jiles-Atherton model are discussed in [12]. The model is validated on a cantilever beam harvester using a single base excitation value for the first four resonant frequencies to analyze the harvester output power. A two degree of freedom lumped parameter non-linear coupled magneto-mechanical model is presented in [14] where an elastic magnifier is introduced with a traditional cantilever beam harvester. This allows two resonant frequencies with magnified tip displacement to work at a lower resonant frequency. A fully coupled non-linear Gibbs free energy-based magneto-mechanical model is presented in [7]. The model is validated on a cylindrical rod type harvester device. The authors show that the model reasonably predicts the output power of 3 mW with some discrepancies.

Despite the need for a generic modeling approach that can be applied to analyze different types of magnetostrictive energy harvesters, most models presented earlier in the literature have been validated only on one specific harvester. It is thus unclear if the models are capable of accounting for the influence of the harvester geometry (e.g. rod or beam type) and different operating conditions (e.g. mechanical loading and frequency, magnetic closure circuit and magnetic field bias). In our earlier work, we have developed a thermodynamic magneto-mechanical modeling approach, implemented it in a 3D FE model using COMSOL Multiphysics, and validated it against experiments on a rod-type galfenol-based energy harvesting concept device [15,16]. This paper extends the work by validating the model with a cantilever beam type harvester. The results show that the model can also be used to reasonably predict the open circuit output voltage and resonant frequency of the cantilever beam harvester.

2. Experimental methods

2.1. Material characterization

The magneto-mechanical energy harvester utilizes galfenol produced by Extrema products as the active material which has the stoichiometry of $Fe_{81.6}Ga_{18.4}$, a polycrystalline material grown as ⟨0 0 1⟩ axis aligned along the length of the material. The characterization of the material is needed to identify the magneto-mechanical constitutive laws describing the magneto-elastic behavior. The detailed discussion on the experimental setup for the characterization of the material is given in [15]. In brief, a cylindrical galfenol rod of length 60 mm and diameter 12 mm is first magnetized using a 200 mHz AC voltage with the help of two sets of coils and a U-shaped iron yoke. The rod is then subjected to a static uniaxial compressive mechanical preload σ ranging from 0 to 80 MPa with a step of 5 MPa to obtain a set of magnetization (B–H) curves under stress. The magnetic field strength H is measured by a Hall probe placed in the middle of the rod whereas the magnetic flux density B is obtained by integrating the voltage induced in a pickup coil wound around the sample.

2.2. Cantilever beam energy harvester

The experimental setup of the prototype cantilever beam type energy harvesting concept device is presented in Fig. 1. A similar harvester device design is also presented in [9] and [14]. The energy harvester consists of a cantilever beam, two sets of permanent magnets and a pickup coil wound around the beam. The cantilever beam consists of a galfenol strip with a length of 60 mm, width of 6 mm and thickness of 0.78 mm. The galfenol layer acts as an active material for the energy harvester which is supported by an aluminum strip which acts as a passive substrate layer. The aluminum strip has a length of 60 mm, width of 6 mm and thickness of 1.28 mm. The galfenol and aluminum beams are glued together with a uniform thin layer of glue to avoid misalignments that can affect the bending modes of the beam.

The working principle of the experimental setup is explained with the 2D schematic diagram presented in Fig. 2. The magnetic bias is provided by two sets of $10 \times 10 \times 10$ mm^3 neodymium magnets having remanence flux density of approximately 1.18 T. The remanence flux density is deduced by tuning the simulated magnetic field near the surface of the magnet in COMSOL to match the magnetic field measured using a Hall probe. The magnets are attached at both ends of the beam with super glue and enforced by caps made of 3D printed PETG material screwed to keep the magnets in place. The weights of the magnet and the cap are measured to be 7.57 g and 2.14 g, respectively, and together they act as the tip mass on the free end of beam. A pickup coil of 1000 turns made from 0.1 mm thick enameled copper wire is attached at the free end of the beam as shown in Fig. 1 and Fig. 2. The harvester beam is clamped to the aluminum base structure such that the active length of the cantilever beam is 38 mm from the fixed end as seen from the Fig. 2. The mechanical vibrations are provided by a Brüel & Kjær shaker device

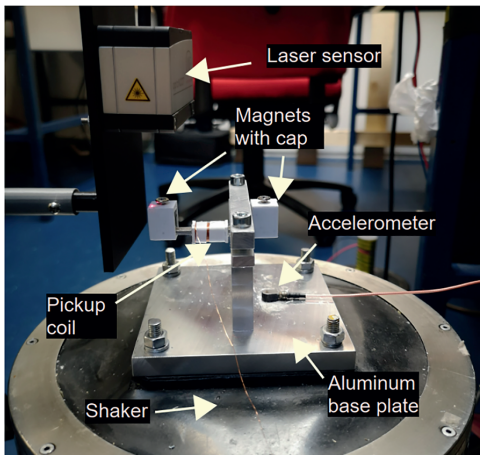

Fig. 1. The experimental setup and prototype design of the magnetostrictive energy harvester for model validation.

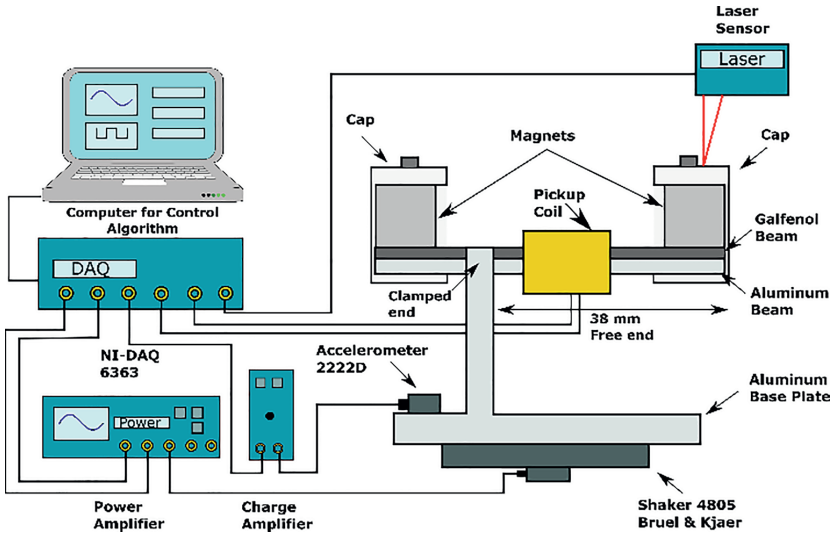

Fig. 2. Schematic diagram of the complete energy harvester setup.

that uses a permanent magnet motor (base model type 4805 with tabletop type 4813). The input signal from the shaker is supplied by a linear amplifier from Venable instruments. The shaker is able to provide peak-to-peak displacement of 13 mm at maximum 3 kHz excitation frequency. The custom-built aluminum base plate is screwed to the shaker base plate to provide a suitable rigid support for the cantilever, provide an air gap from the permanent magnet inside the shaker and securely transfer the forced sinusoidal mechanical vibrations. An optical laser displacement sensor (optoNTDC ILD1900-25) from Micro-Epsilon measures the tip displacement of the free end as shown in the Fig. 2. The laser sensor has linearity range of $< \pm 5$ μm, sampling rate of 10 kHz and its measuring range is 25 mm from the object. The vibration amplitude of the shaker plate is measured by mounting a piezoelectric accelerometer (model 2222D) which is connected to a charge amplifier from Brüel & Kjær (model type 2635) for signal conditioning.

The control algorithm is implemented in MATLAB using a National Instruments data acquisition card NI-6363. The experimental tests are performed by varying the vibration amplitudes from 0.5 g to 2 g with a step of 0.5 g. The mechanical vibration causes varying stress/strain in the beam which causes change in the magnetization of the material. A voltage is induced in the pickup coil attached to the beam as a result of the inverse magnetostrictive effect and Faraday's law. For each value of the vibration amplitude, the frequency sweep operation is performed to determine the resonant frequency of the beam by measuring the tip displacement. The amplitude of the input signal voltage supplied to the shaker is controlled by measuring the acceleration with the accelerometer attached to the aluminum base plate. The input signal is varied iteratively to obtain the desired acceleration which is then kept constant throughout the frequency sweep operation. The experiments are repeated three times to check the repeatability. The open circuit voltage, tip displacement and resonant frequency are measured to study the effect of operating frequency on the harvester performance. In this study we test the ability of the model to reproduce the effect of amplitude of mechanical vibration, magnetic bias and excitation frequency on the harvester output voltage.

3. Models

3.1. Constitutive model

The constitutive equations describing the directly-coupled multiaxial magneto-mechanical behavior in the galfenol material are derived using a thermodynamic approach, which has been presented in [17] and further discussed e.g. in [18] and [19]. The detailed discussion about implementing the approach in 3D in COMSOL Multiphysics software is presented in [15] and [16]. In brief, a Helmholtz free energy density function $\psi(\boldsymbol{B}, \boldsymbol{\varepsilon})$ is defined to describe the magneto-elastic interaction as a function of the magnetic flux density vector $\boldsymbol{B}$ and the strain tensor $\boldsymbol{\varepsilon}$. The exact form of the energy–density expression in [15–19] has varied while the model has evolved. Here it is written as

$$\psi(B,\varepsilon) = \frac{1}{2}\lambda I_1^2 + \mu I_2 + \sum_{i=1}^{\eta_\alpha} \alpha_i I_4^i + \sum_{i=1}^{\eta_\beta} \beta_i I_5^i + \sum_{i=1}^{\eta_\gamma} \gamma_i I_6^i \tag{1}$$

where α_i, β_i and γ_i are fitting parameters obtained from material characterization, and λ and μ are the Lamé parameters obtained from Young's modulus and Poisson's ratio. The total strain $\boldsymbol{\varepsilon}$ consists of the mechanical strain and the strain caused by magnetostriction. The state variables of ψ are written in terms of scalar invariants $I_1 = \mathrm{tr}(\boldsymbol{\varepsilon})$, $I_2 = \mathrm{tr}(\boldsymbol{\varepsilon}^2)$ describing linear elastic behavior, $I_4 = \boldsymbol{B}\cdot\boldsymbol{B}$ describing magnetic behavior and $I_5 = \boldsymbol{B}\cdot\boldsymbol{e}\boldsymbol{B}$ and $I_6 = \boldsymbol{B}\cdot\boldsymbol{e}^2\boldsymbol{B}$ describing magneto-mechanical behavior of the material, $\boldsymbol{e}$ being the deviatoric part of $\boldsymbol{\varepsilon}$. The constitutive equations for the magnetic field strength $\boldsymbol{H}$ and Cauchy stress tensor $\boldsymbol{\sigma}$ are then obtained by partial differentiation of the energy expression as

$$\boldsymbol{H}(\boldsymbol{B},\boldsymbol{\varepsilon}) = \left(\frac{\partial\psi}{\partial\boldsymbol{B}}\right)^{\mathrm{T}} \text{ and } \boldsymbol{\sigma}(\boldsymbol{B},\boldsymbol{\varepsilon}) = \frac{\partial\psi}{\partial\boldsymbol{\varepsilon}}. \tag{2}$$

The polynomial coefficients α_i, β_i and γ_i are determined by fitting the function $\boldsymbol{H}(\boldsymbol{B}, \boldsymbol{\varepsilon})$ obtained from (1) and (2) against the single-valued $H(B, \sigma)$ curves measured with the material characterization setup discussed in Section 2.1. During the fitting, the strain tensor $\boldsymbol{\varepsilon}$ is iterated with the Newton-Raphson method until the desired uniaxial stress is obtained. The fitting is done for the mechanical compressive preload range of 20 to 50 MPa for $\eta_\alpha = 11$, $\eta_\beta = 1$ and $\eta_\gamma = 2$ and the coefficient of the fitting parameters are given in [16].

3.2. Finite element model

The analytical expressions of the constitutive equations (1)-(2) are implemented in a 3D FE solver in COMSOL by overriding the electromagnetic and mechanical constitutive equations. The detailed discussion for the model implementation is presented in [16]. The 3D magneto-mechanical FE simulation for a cantilever beam type harvester is carried out for one half of the geometry, which is presented in Fig. 3. The model is constructed based on the actual prototype harvester device which consists of the galfenol beam attached to the aluminum beam, two permanent magnets at both ends and a pickup coil wound around the beam. In the COMSOL model, the solid mechanics interface solves for the equation of motion which includes the material damping written as

$$\rho\left(\frac{d^2\boldsymbol{u}}{dt^2}+\alpha_{\mathrm{dM}}\frac{d\boldsymbol{u}}{dt}\right)-\nabla\cdot\left(\boldsymbol{\sigma}(\boldsymbol{B},\boldsymbol{\varepsilon})+\beta_{\mathrm{dK}}\frac{\partial\boldsymbol{\sigma}(\boldsymbol{B},\boldsymbol{\varepsilon})}{\partial t}\right)=0 \tag{3}$$

where $\boldsymbol{u}$ is the displacement vector, ρ is the mass density, and α_{dM} and β_{dk} are the mass and stiffness damping parameters, respectively. The mechanical damping is simulated as Rayleigh damping expressed as

$$\zeta=\frac{1}{2}\left(\frac{\alpha_{\mathrm{dM}}}{2\pi f_0}+\beta_{\mathrm{dK}}2\pi f_0\right). \tag{4}$$

The damping ratio ζ and the resonant frequency f_0 are experimentally obtained from a free vibration test. The damping is assumed to consist mainly of the material-related damping β_{dk}, which is obtained from (4) by setting $\alpha_{\mathrm{dM}}=0$.

The normal component of displacement u_y is set to zero at the sliced boundary. The sinusoidal mechanical vibration amplitude ranging from 0.5 g to 2 g is imposed by prescribing the normal component of the displacement u_z on the aluminum clamp domain. The tip mass of 9.71 g is realized utilizing an added mass node to the magnet domain at the free end of the beam. The electromagnetic fields are computed by adding the magnetic field interface which solves the Maxwell's equations. The remanence flux density of the permanent magnets is the set as 1.18 T.

In the galfenol material, the combination of Ampere's and Faraday's laws is solved in terms of the magnetic vector potential $\boldsymbol{A}$ as

$$\nabla\times\boldsymbol{H}(\boldsymbol{B},\boldsymbol{\varepsilon})+\kappa\frac{\partial\boldsymbol{A}}{\partial t}=0 \tag{5}$$

where κ denotes the electrical conductivity. In the other regions, a purely electromagnetic problem is solved as

$$\nu\nabla\times\nabla\times\boldsymbol{A}+\kappa\frac{\partial\boldsymbol{A}}{\partial t}=\nabla\times\boldsymbol{H}_{\mathrm{c}} \tag{6}$$

where ν is the constant reluctivity and $\boldsymbol{H}_{\mathrm{c}}$ is the coercive field of the magnets. The voltage V_{ind} induced into the pickup coil is computed by averaging the time derivative of the circumferential component of the magnetic vector potential $\boldsymbol{A}$ over all possible paths in the cylindrical coil volume Ω_{coil} as

$$V_{\mathrm{ind}}=\frac{N}{S_{\mathrm{coil}}}\int_{\Omega_{\mathrm{coil}}}\frac{\partial\boldsymbol{A}_0}{\partial t}d\Omega \tag{7}$$

where N is the number of coil turns and S_{coil} is the cross-section area of the coil domain. The time integration is done using the Generalized Alpha method (a second order backward differential formulation with a parameter to control the damping of higher frequencies) instead of Backward Euler method since the latter causes numerical damping at higher frequencies [20]. The resulting non-linear system is solved using the Newton Raphson method.

4. Results and discussion

4.1. Material characterization

The energy density function ψ is fitted to the single-valued measured $H(B,\sigma)$ curves obtained from the material characterization setup discussed in Section 2.1. The comparison of the measured and fitted curves is presented in Fig. 4. The fitting is performed for the preload range of 20 to 50 MPa shown in Fig. 4. The preload range of 20 to 50 MPa is chosen as it provides a relatively good fitting against the measured B–H curves from 0 to 80 MPa explained in [16] which also contains the coefficients of the fitting parameters.

4.2. Beam resonant frequency

As discussed in Section 1, optimizing the energy harvester design requires knowledge related to operating conditions including the resonant frequency, magnetic bias etc. From literature [9] it is known that maximum power is generated when the cantilever beam operates at the resonant frequency. For the energy harvesting setup discussed in Section 2.2, the resonant frequency of the beam is first calculated analytically as

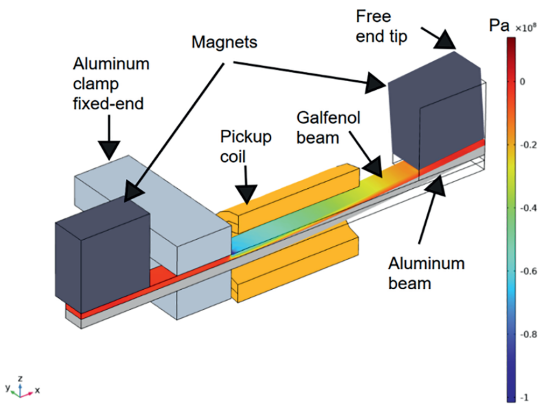

Fig. 3. The geometry of the model implemented in COMSOL for 3D FE simulation. Color bar denotes xx-component of stress in the galfenol beam (Pa).

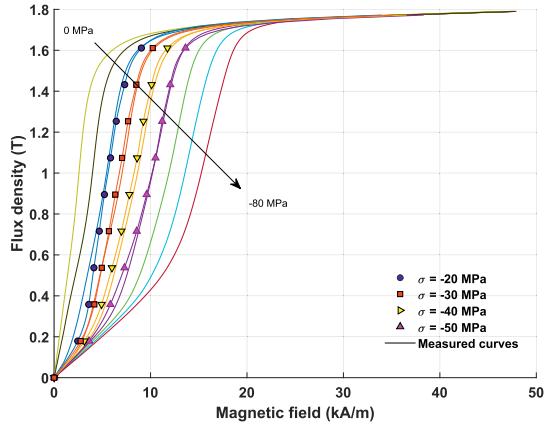

Fig. 4. Comparison among measured (solid lines) and fitted (lines with markers) magnetization curves B–H under different values of static compressive preload (σ).

$$f_0 = \frac{1}{2\pi}\sqrt{\frac{3EI}{(M + m_{\text{eff}})l^3}} \tag{8}$$

where E is the effective Young's modulus taken as 70 GPa for the combined galfenol-aluminum beam, M is the tip mass of 9.71 g including the PEGT caps whereas m_{eff} is the effecting beam mass of 2.2 g. The term l denotes the effective beam length of 38 mm and I is the second moment of inertia. The resonant frequency calculated from (8) is 189 Hz.

Experimentally, the resonant frequency with magnets attached at both ends is then obtained from free vibrations by measuring the decaying amplitude of the tip displacement presented in Fig. 5. The free vibrations are measured using a precision laser displacement sensor. The damping ratio ζ is computed from the free vibrations using a logarithmic decrement method as

$$\zeta = \frac{\ln\left(\frac{X_k}{X_{k+n}}\right)}{2\pi n} \tag{9}$$

where X_k and X_{k+n} are the k^{th} and $(k + n)^{\text{th}}$ values of the peak displacement amplitude. A resonant frequency of 200 Hz is obtained by measuring a time of 200 ms over $n = 8$ consecutive periods as indicated in the Fig. 5. A damping ratio of $\zeta = 0.0145$ is deduced for the corresponding peaks of the free vibrations.

Next, two sets of experiments are performed to determine the effect of magnetostriction on the resonant frequency. In case of forced vibrations, the resonant frequency is measured using a frequency sweep method by applying sinusoidal vibrations of 1 g acceleration. The first test is performed when the beam is magnetized by the permanent magnets, sweeping the frequency around the resonant frequency of 200 Hz obtained from the free vibration test. The second test is performed when the magnets are replaced by iron cubes with exactly the same weight as the magnets, sweeping the frequency around the analytically calculated resonant frequency of 189 Hz. A resonant frequency of 201 Hz is obtained with the magnets, and a resonant frequency of 187 Hz is obtained with the iron cubes at 1 g acceleration shown in Fig. 6 (a) and (b), which indicates that the magnetostriction increases the resonant frequency. The increase in resonant frequency can be explained by the so-called ΔE effect which states that the Young's modulus of the magnetostrictive material increases due to magnetization as discussed in [21] and [22]. According to (8), the increasing Young's modulus increases the resonant frequency.

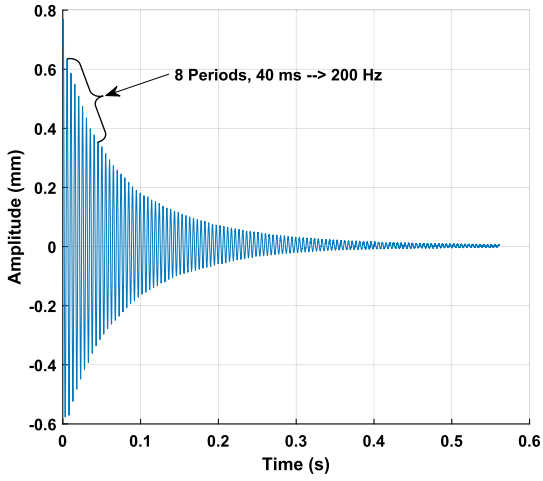

Fig. 5. Measured tip displacement at free vibration. The measured resonant frequency deduced from free vibration is 200 Hz.

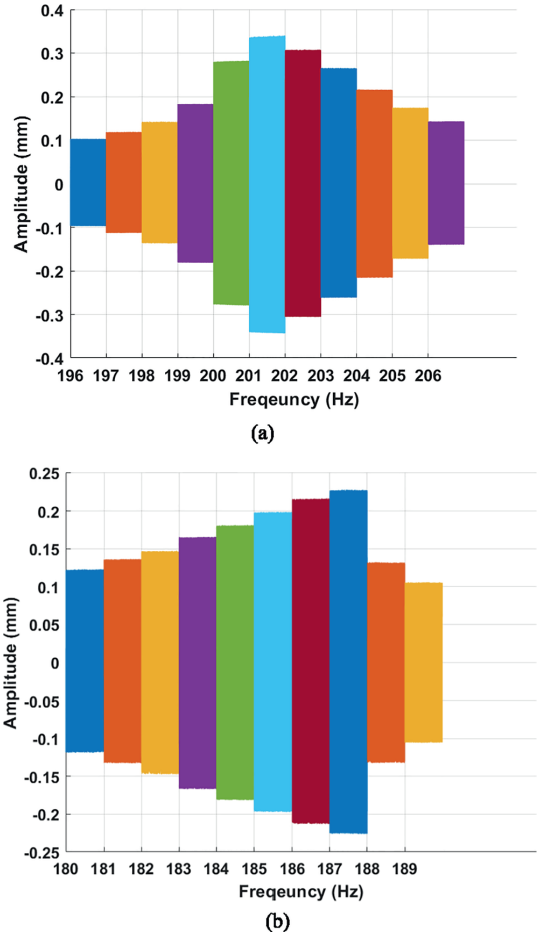

Fig. 6. Measured tip displacement under 1 g acceleration using the frequency sweep method. A resonant frequency of 201 Hz is obtained with magnets (a) and 187 Hz with iron cubes (b).

For the FE simulations in COMSOL, the mechanical damping is realized using Rayleigh damping presented in (4) where f_0 is kept constant at 201 Hz (obtained from the frequency sweep) throughout the simulations. The FE simulation is performed with and without magnetostriction to validate the thermodynamic model and to compare the results. A resonant frequency of 200 is computed with magnetostriction whereas a resonant frequency of 184 Hz is computed without magnetostriction using the magneto-mechanical model. This illustrates that the model can successfully predict the change in the resonant frequency due to magnetostriction. The comparison among measured, simulated and analytically calculated resonant frequencies showing the effect of magnetostriction is given in Table 1.

Table 1
Comparison of measured, simulated and analytically calculated resonant frequencies at 1 g.

	Measured	Simulated	Analytical
With magnetostriction	201 Hz	200 Hz	–
Without magnetostriction	187 Hz	184 Hz	189 Hz

4.3. Energy harvesting setup

The comparison of the measured and simulated open circuit voltage (rms) and tip displacement showing the influence of mechanical vibration amplitude and frequency is presented in Figs. 7 and 8. The results are obtained by applying forced mechanical vibrations from 0.5 g to 2 g for the frequency range of 196 Hz to 206 Hz. The results show that the output voltage is maximum at the resonant frequency which decreases slightly with the increase in the amplitude of the mechanical vibrations. The experiments are repeated three times keeping the same input conditions to check the repeatability. The deviations can be seen among the measured experimental results from Fig. 7 (a) and Fig. 8 (a) shown as markers, whereas the solid lines indicate the mean value. The deviation is large near the resonant frequency for the 1.5 g and 2 g excitations. This is caused by a large tip displacement due to high acceleration considering the size of the beam, which makes it difficult to stabilize near the resonant frequency.

As discussed earlier, the harvester utilizes ambient vibrations whose frequency and amplitude cannot be controlled. Therefore, the proposed model can be used to optimize the geometry and tip mass such that the harvester operates at the resonant frequency for peak performance. The comparison among measured and simulated results depicts that the thermodynamic model can accurately predict the resonant frequency with a percentage error of less than 2 %. Moreover, the results show that the resonant frequency decreases slightly with the increase in the vibration amplitude from 202 Hz to 198 Hz also predicted by the simulated results in Fig. 7 and Fig. 8.

The difference in the amplitudes of the measured and simulated displacement is caused by the damping ratio which is chosen to be frequency independent in FE simulations throughout the frequency sweep. Changing the damping ratio directly affects the tip displacement and hence the output voltage. The simulated output voltage is also affected by the magnetic bias which is estimated by measuring the magnetic field using a Hall sensor. Furthermore, the simulations do not account for the thickness of glue or the small airgaps between the caps holding the magnets at both ends. In addition, the output voltage is found sensitive to the placement of the pickup coil over beam, slight displacement of the permanent magnets and the cantilever's support clamping strength of the aluminum base also affects the resonant frequency and tip displacement. Therefore, the comparison of measurement and simulated results should be done keeping in mind the sensitivity in the

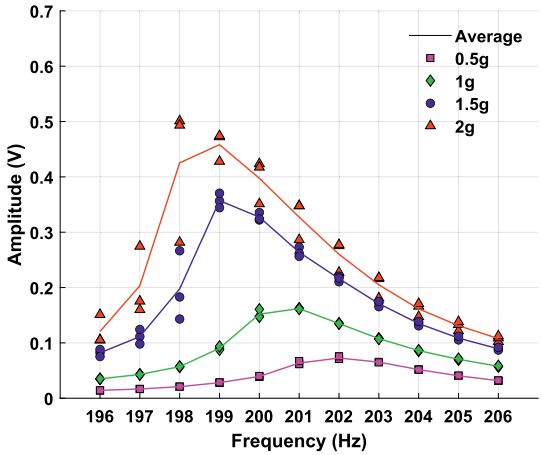

(a)

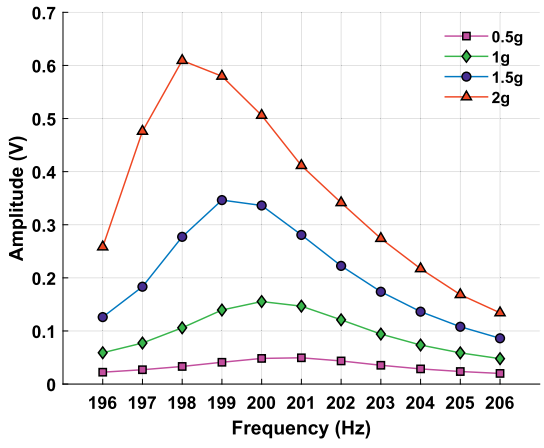

(b)

Fig. 7. Measured (a) and simulated (b) open circuit voltage (rms) curves under varying amplitude of mechanical vibrations.

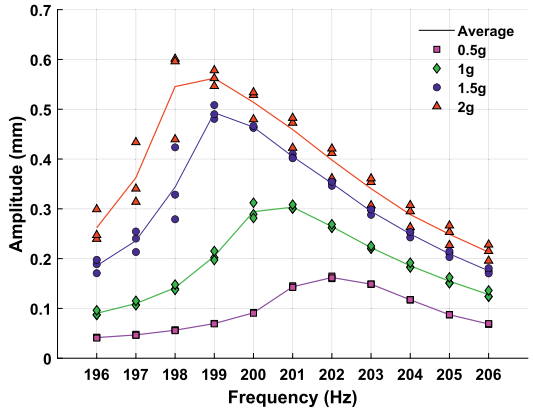

(a)

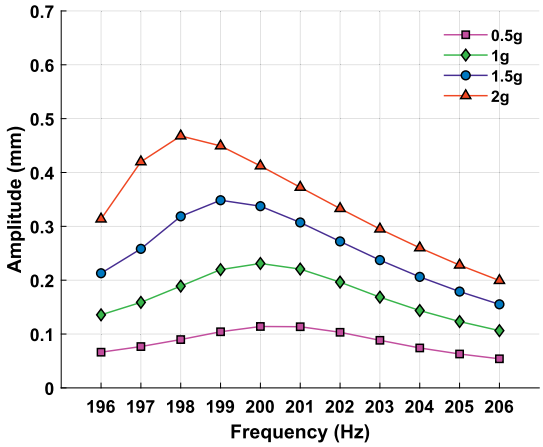

(b)

Fig. 8. Measured (a) and simulated (b) tip displacement measured from laser sensor.

measurements and limitations of the model.

5. Conclusion

In this paper, a thermodynamic magneto-mechanical modeling approach has been successfully validated against measurements from a cantilever beam type prototype energy harvester device. The model has previously been validated to analyze a cylindrical rod type harvester [15] which was modified later to include a magnetic closure circuit with varying magnetic field bias discussed in [16]. The thermodynamic model has been implemented in COMSOL Multiphysics software for 3D FE simulations. The advantage of implementing the model in COMSOL is the ability to conveniently modify the harvester geometry and perform parametric sweep operations to analyze the performance of the harvester for device optimization. Comparison of the simulated and measured results indicates that the model can accurately predict the resonant frequency of the harvester yielding maximum performance and determine the output voltage under varying vibration amplitudes and frequencies.

The FE simulations are performed considering no airgap between the magnets and the beam and a strong mechanical contact between the galfenol and aluminum beams which is an ideal condition that differs from the actual setup which uses adhesive and mechanical means of attachment. For comparison, the model needs to be tuned in order to consider the exact mechanical stresses in the beam and magnetic field bias which is not practical for each mechanical loading case. Furthermore, it is concluded that comparison of the measured and simulated results requires repeatable measurements which should be ensured by maintaining a constant clamping position of the cantilever beam, coil placement and magnet displacement. However, the measurement repeatability suffers near resonant frequency at high vibration amplitude caused by slight displacement of the tip magnet which changes the mechanical damping.

Modeling tools are required to determine the optimal design characteristic (harvester geometry, coil parameters, magnetic bias etc.) under available operating conditions (vibration amplitude, nature and frequency of mechanical vibrations) to analyze the energy harvester device and then optimize it to obtain peak performance. Combining the results of this paper to those of [15] and [16], the thermodynamic modeling approach has been validated to be suitable as a generic tool for analyzing different types of magnetostrictive energy harvesting devices. For a cantilever beam type harvester geometry, the model is able determine the resonant frequency and open circuit voltage yielding maximum harvester potential. For cylindrical rod type harvester, the model is able to successfully determine the optimal static mechanical preload σ, magnetic bias and optimal value of load resistance to obtain the maximum output power under forced sinusoidal mechanical excitations. The presented modeling approach can thus be used to support the design of energy harvesters for different applications.

CRediT authorship contribution statement

U. Ahmed: Conceptualization, Software, Methodology, Investigation, Writing – original draft. **D. Blažević:** Investigation, Writing – review & editing, Supervision. **Y. Mizukawa:** Investigation. **U. Aydin:** Formal analysis, Software. **P. Rasilo:** Formal analysis, Supervision, Writing – review & editing.

Declaration of Competing Interest

The authors declare that they have no known competing financial interests or personal relationships that could have appeared to influence the work reported in this paper.

Data availability

No data was used for the research described in the article.

Acknowledgements

The authors would like to thank the materials science and environmental engineering group of Tampere University for their assistance with this work. Also, we would like to thank the funding organizations including the European Union's Horizon 2020 research and innovation programme (Marie Skłodowska-Curie grant No 838375), Aimo Puromäki special funds (No. 20200522) awarded by the KAUTE foundation and the Finnish Government Scholarship Pool (No. KM-20-11380) awarded by the Finnish National Agency for Education for supporting this reseach work.

References

[1] X. Tang, X. Wang, R. Cattley, F. Gu, A.D. Ball, Energy harvesting technologies for achieving self-powered wireless sensor networks in machine condition monitoring: a review, Sensors 18 (12) (2018) 4113.
[2] H. Liu, C. Cong, Q. Zhao, K. Ma, Comprehensive analysis of the energy harvesting performance of a fe-ga based cantilever harvester in free excitation and base excitation mode, Sensors 19 (15) (2019) 3412.
[3] P.V. Avvari, Y. Yang, C.K. Soh, Long-term fatigue behavior of a cantilever piezoelectric energy harvester, J. Intell. Mater. Syst. Struct. 28 (9) (2017) 1188–1210.
[4] J. Siang, M.H. Lim, M. Salman Leong, Review of vibration-based energy harvesting technology: mechanism and architectural approach, Int. J. Energy Res. 42 (5) (2018) 1866–1893.
[5] M. Iqbal, M.M. Nauman, F.U. Khan, P.E. Abas, Q. Cheok, A. Iqbal, B. Aissa, Vibration-based piezoelectric, electromagnetic, and hybrid energy harvesters for microsystems applications: a contributed review, Int. J. Energy Res. 45 (1) (2021) 65–102.
[6] V. Berbyuk, Vibration energy harvesting using Galfenol-based transducer, in: Active and Passive Smart Structures and Integrated Systems vol. 8688, SPIE, 2013, pp. 429–440.
[7] S. Palumbo, P. Rasilo, M. Zucca, Experimental investigation on a Fe-Ga close yoke vibrational harvester by matching magnetic and mechanical biases, J. Magn. Magn. Mater. 469 (2019) 354–363.
[8] C.S. Clemente, A. Mahgoub, D. Davino, C. Visone, Multiphysics circuit of a magnetostrictive energy harvesting device, J. Intell. Mater. Syst. Struct. 28 (17) (2017) 2317–2330.
[9] J.H. Yoo, A.B. Flatau, A bending-mode galfenol electric power harvester, J. Intell. Mater. Syst. Struct. 23 (6) (2012) 647–654.
[10] X. Zhao, D.G. Lord, Application of the Villari effect to electric power harvesting, J. Appl. Phys. 99 (8) (2006) 08M703.
[11] S. Cao, J. Zheng, Y. Guo, Q. Li, J. Sang, B. Wang, R. Yan, Dynamic characteristics of Galfenol cantilever energy harvester, IEEE Trans. Magn. 51 (3) (2015) 1–4.
[12] P.G. Evans, M.J. Dapino, Dynamic model for 3-D magnetostrictive transducers, IEEE Trans. Magn. 47 (1) (2010) 221–230.
[13] S. Chakrabarti, M.J. Dapino, Coupled axisymmetric finite element model of a hydraulically amplified magnetostrictive actuator for active powertrain mounts, Finite Elem. Anal. Des. 60 (2012) 25–34.
[14] S. Cao, L. Liu, J. Zheng, R. Pan, G. Song, Modeling and analysis of Galfenol nonlinear cantilever energy harvester with elastic magnifier, IEEE Trans. Magn. 55 (6) (2019) 1–5.
[15] U. Ahmed, J. Jeronen, M. Zucca, S. Palumbo, P. Rasilo, Finite element analysis of magnetostrictive energy harvesting concept device utilizing thermodynamic magneto-mechanical model, J. Magn. Magn. Mater. 486 (2019) 165275.
[16] U. Ahmed, U. Aydin, M. Zucca, S. Palumbo, R. Kouhia, P. Rasilo, Modeling a Fe-Ga energy harvester fitted with magnetic closure using 3D magneto-mechanical finite element model, J. Magn. Magn. Mater. 500 (2020) 166390.
[17] K. Fonteyn, A. Belahcen, R. Kouhia, P. Rasilo, A. Arkkio, FEM for directly coupled magneto-mechanical phenomena in electrical machines, IEEE Trans. Magn. 46 (8) (2010) 2923–2926.
[18] P. Rasilo, D. Singh, U. Aydin, F. Martin, R. Kouhia, A. Belahcen, A. Arkkio, Modeling of hysteresis losses in ferromagnetic laminations under mechanical stress, IEEE Trans. Magn. 52 (3) (2015) 1–4.
[19] P. Rasilo, D. Singh, J. Jeronen, U. Aydin, F. Martin, A. Belahcen, L. Daniel, R. Kouhia, Flexible identification procedure for thermodynamic constitutive models for magnetostrictive materials, Proc. R. Soc. A 475 (2223) (2019) 20180280.
[20] Z. Deng, M.J. Dapino, Multiphysics modeling and design of Galfenol-based unimorph harvesters, in: Industrial and Commercial Applications of Smart Structures Technologies, vol. 9433, SPIE, 2015, pp. 74–83.
[21] M. Löffler, R. Kremer, A. Sutor, R. Lerch, Hysteresis of the resonance frequency of magnetostrictive bending cantilevers, J. Appl. Phys. 117 (17) (2015) 17A907.
[22] L. Daniel, O. Hubert, An analytical model for the ΔE effect in magnetic materials, Eur. Phys. J.-Appl. Phys. 45 (3) (2009) 31101.